ANALYSIS OF THE PLASMA RESPONSE IN A HALL THRUSTER

Eduardo Ahedo
Juan M. Gallardo
Félix I. Parra

E.T.S.I. AERONAUTICOS
UNIVERSIDAD POLITECNICA DE MADRID
SPAIN

Final Report, September 15, 2002.

Contract order number: F61775-01-WE070
Contracting Entity: EOARD-AFOSR
Supervisor: Dr. Ingrid Wysong

REPORT DOCUMENTATION PAGE	Form Approved OMB No. 0704-0188

Public reporting burden for this collection of information is estimated to average 1 hour per response, including the time for reviewing instructions, searching existing data sources, gathering and maintaining the data needed, and completing and reviewing the collection of information. Send comments regarding this burden estimate or any other aspect of this collection of information, including suggestions for reducing the burden, to Department of Defense, Washington Headquarters Services, Directorate for Information Operations and Reports (0704-0188), 1215 Jefferson Davis Highway, Suite 1204, Arlington, VA 22202-4302. Respondents should be aware that notwithstanding any other provision of law, no person shall be subject to any penalty for failing to comply with a collection of information if it does not display a currently valid OMB control number.
PLEASE DO NOT RETURN YOUR FORM TO THE ABOVE ADDRESS.

1. REPORT DATE ***(DD-MM-YYYY)*** 26-08-2002	**2. REPORT TYPE** Final Report	**3. DATES COVERED** *(From – To)* 13 August 2001 - 13-Aug-02

4. TITLE AND SUBTITLE ANALYSIS OF THE PLASMA RESPONSE IN A HALL THRUSTER	**5a. CONTRACT NUMBER** F61775-01-WE070
	5b. GRANT NUMBER
	5c. PROGRAM ELEMENT NUMBER
6. AUTHOR(S) Professor EDUARDO A Ahedo	**5d. PROJECT NUMBER**
	5d. TASK NUMBER
	5e. WORK UNIT NUMBER
7. PERFORMING ORGANIZATION NAME(S) AND ADDRESS(ES) UNIVERSIDAD POLITECNICA DE MADRID ETSI Aeronauticos Plaza Cardenal Cisneros Madrid 28040 Spain	**8. PERFORMING ORGANIZATION REPORT NUMBER** N/A
9. SPONSORING/MONITORING AGENCY NAME(S) AND ADDRESS(ES) EOARD PSC 802 BOX 14 FPO 09499-0014	**10. SPONSOR/MONITOR'S ACRONYM(S)**
	11. SPONSOR/MONITOR'S REPORT NUMBER(S) SPC 01-4070

12. DISTRIBUTION/AVAILABILITY STATEMENT

Approved for public release; distribution is unlimited.

13. SUPPLEMENTARY NOTES

14. ABSTRACT

This report investigates 1 dimensional and 2 dimensional hall effect thruster models to better understand the following physics related issues: radial structure of the plasma, lateral wall effects, physics of the subsonic region, no near-total ionization regimes, effects of secondary electron emission from the walls, and reduction of the growth rate of self oscillations.

15. SUBJECT TERMS

EOARD, Modelling & Simulation, Hall effect thrusters, electric propulsion, plasma

16. SECURITY CLASSIFICATION OF:			**17. LIMITATION OF ABSTRACT**	**18, NUMBER OF PAGES**	**19a. NAME OF RESPONSIBLE PERSON**
a. REPORT UNCLAS	**b. ABSTRACT** UNCLAS	**c. THIS PAGE** UNCLAS	UL	115	Ingrid Wysong
					19b. TELEPHONE NUMBER *(Include area code)* +44 (0)20 7514 4285

The Contractor, UNIVERSIDAD POLITECNICA DE MADRID, hereby declares that, to the best of its knowledge and belief, the technical data delivered herewith under Contract No F61775-01-WE070 is complete, accurate, and complies with all requirements of the contract.

September 20, 2002

Eduardo Ahedo Principal Investigator	Javier UCEDA Vice President for Research and Institutional Relations

We certify that there were no subject inventions to declare as defined in FAR 52.227-13, during the performance of this contract.

September 20, 2002

Eduardo Ahedo Principal Investigator	Javier UCEDA Vice President for Research and Institutional Relations

The material of Chapters 1, 2, and 4 has produced three papers published this year in Physics of Plasmas, Refs.[3, 2, 5]. The material of Chapters 3, 5, and 6 corresponds to work in progress and has been presented in three papers at the AIAA Joint Propulsion Conference, Indianapolis, July 7-10, 2002, Refs.[12, 4, 30].

In most of the report we have reproduced the texts of the respective papers. The coherence of each chapter is preserved in that way, but the whole report suffers from some repetitions and minor inconsistencies. The authors apologize for it.

The authors acnowledge fruitful discussions with Prof. Manuel Martínez-Sánchez.

Contents

1 RADIAL PRESHEATH MODEL FOR FLOWING PLASMAS 9

1.1 INTRODUCTION . . . 9
1.2 MODEL FORMULATION . . . 10
  1.2.1 The quasineutral presheath . . . 10
  1.2.2 The sheaths . . . 13
1.3 PLANAR AND ANNULAR SOLUTIONS . . . 14
  1.3.1 Planar geometry: cold ions . . . 14
  1.3.2 Planar geometry: general solution . . . 15
  1.3.3 Annular geometry . . . 15
1.4 SUMMARY . . . 16

2 RADIAL MODEL WITH SECONDARY EMISSION 23

2.1 INTRODUCTION . . . 23
2.2 MODEL FORMULATION . . . 24
2.3 SHEATH ANALYSIS . . . 25
  2.3.1 Sheath solution . . . 25
  2.3.2 The charge-saturated regime(CSR) . . . 28
2.4 COMPLETE SOLUTION . . . 28
  2.4.1 Presheath solution . . . 28
  2.4.2 Presheath/sheath matching . . . 29
  2.4.3 Results . . . 30
2.5 DISCUSSION . . . 31

3 PARTIAL TRAPPING OF SECONDARY ELECTRON EMISSION 39

3.1 INTRODUCTION . . . 39
3.2 MODEL FORMULATION . . . 40
3.3 SHEATH ANALYSIS . . . 41
  3.3.1 Dimensionless solution . . . 42
  3.3.2 Charge-saturation . . . 43
  3.3.3 Results . . . 43
3.4 PLANAR PRESHEATH ANALYSIS . . . 44
3.5 CONCLUSIONS . . . 46

4 AXIAL MODEL WITH HEAT CONDUCTION 53
4.1 INTRODUCTION 53
4.2 THE QUASINEUTRAL MODEL 54
4.2.1 Electron dynamics 55
4.2.2 Quasineutral equations 56
4.3 MODEL INTEGRATION 58
4.3.1 Singular/sonic points 58
4.3.2 Anode sheath 58
4.3.3 Boundary conditions 59
4.3.4 Integration procedure 59
4.4 ANALYSIS OF THE SPATIAL SOLUTION 60
4.4.1 Axial structure of the discharge 60
4.4.2 Inertial effects on electrons 62
4.4.3 Ion temperature 62
4.5 THRUST AND EFFICIENCY 63
4.5.1 Thrust 63
4.5.2 Thrust efficiency 64
4.6 THRUSTER PERFORMANCE 65
4.6.1 Domain of stationary solutions 65
4.6.2 Optimum performance 65
4.7 CONCLUSIONS 66

5 AXIAL MODEL WITH LATERAL WALL EFFECTS 73
5.1 INTRODUCTION 73
5.2 MODEL FORMULATION 74
5.2.1 Boundary conditions and structure of the discharge 75
5.3 STRUCTURE OF THE DISCHARGE 75
5.4 THRUST AND EFFICIENCY 77
5.5 PARAMETER INVESTIGATION 79
5.6 CONCLUSIONS 79

6 MODEL WITH AN INTERMEDIATE ELECTRODE 89
6.1 INTRODUCTION 89
6.2 MODEL FORMULATION 90
6.3 STRUCTURE OF THE DISCHARGE 92
6.4 PARAMETER INVESTIGATION 92
6.5 CONCLUSIONS 93

A DERIVATION OF THE RADIAL PRESHEATH MODEL 99

B ON THE PRESHEATH/SHEATH TRANSITION 101

C PARAMETER INVESTIGATION ON THE AXIAL MODEL 103

BIBLIOGRAPHY 111

Chapter 1

RADIAL PRESHEATH MODEL FOR FLOWING PLASMAS

1.1 INTRODUCTION

The transverse interaction of a collisionless plasma with two dielectric walls confining it was treated originally by Tonks and Langmuir[54], who solved the fundamental issues. The zero-current condition at the walls means that fluxes of ions and electrons to the walls must be equal, which implies a potential profile decreasing monotonically from around the center of the channel towards the two walls. Tonks and Langmuir showed that, in the zero Debye-length limit, the plasma structure consists of two thin non-neutral sheaths tied to the walls and a quasineutral region (the *presheath*) occupying the bulk of the channel. Each type of region is solved separately in their own distinguished scale. The condition for a correct presheath/sheath transition is *unique* and consists in the plasma flow being sonic there (the Bohm condition[20]). Apart from the three basic wall geometries, Tonks and Langmuir (interested in thin cylindrical probes immersed in cylindrical channels) discussed the case of an annular geometry, pointing out the lack of symmetry between the profiles of the inner and outer presheaths (these ones separated by the point of maximum electric potential).

A central contribution of Tonks and Langmuir is the *plasma balance equation*, which establishes the plasma production rate required to sustain a steady-state discharge. This production rate is proportional to the channel width, as it comes out from equating the volumetric production of plasma to the losses at the walls. In Tonks-Langmuir model, where plasma production is dominated by ionization, the plasma balance equation fixes the ionization rate and, as a consequence, the plasma temperature; indeed, a steady-state discharge is not possible when the plasma production rate is larger than the maximum ionization rate of the gas. Tonks and Langmuir considered different radial profiles for the ionization rate, but it was shown later that the mean value of the plasma production rate is independent of its radial profile [33, 23].

Bissell *et al.*[16] (reviewing several other papers) and Scheuer and Emmert[50] propose macroscopic formulations of the Tonks-Langmuir problem (for planar geometry only), with different closure hypotheses for the ion energy equation. They conclude that macroscopic models can approximate well the kinetic results, mainly in relation to particle and energy fluxes towards the walls.

As the Tonks-Langmuir model, these fluid models include ionization as the only source term in the plasma equations and, therefore, are restricted to no-flowing plasmas basically. When the plasma flows along the confining walls, the problem becomes two-dimensional(2D), with mutual interaction between the longitudinal and transverse (i.e. axial and radial) dynamics. However, at each axial cross-section (of a long channel) we may consider the one-dimensional(1D) problem that describes the radial dynamics of the plasma. The requires to take into account the influence of the axial flow on the radial motion. In the macroscopic formulation this can be modeled with adequate source terms in the radial equations.

The goal of this paper is to generalize the presheath/sheath model of Tonks-Langmuir to plasmas flowing axially, with emphasis on the coupled influence of ionization and axial flow on the radial solution. In a preliminary study (with planar geometry and cold ions) we showed already that losses to the wall are reduced by an effective radial friction due to axial variations of the radial conditions[9]. Here we develop the general model for warm ions and annular geometries. Thus, planar, cylindrical, and annular channels are covered; the differences between the inner and outer presheaths in the latter case are an extra aspect of interest. No secondary emission at the walls will be considered here, so that the sheath problem reduces to a well-known solution and the attention of the paper is focused on the presheath model.

An example of application of the present work is the plasma discharge in an annular Hall thruster. Since an accurate two-dimensional analysis of this problem is unavailable yet, partial analyses of the radial and axial problems are of great interest. In particular, the knowledge of the radial plasma structure would allow one to estimate the losses at the lateral walls at each cross-section, which could then be included as sink terms in 1D axial models of the discharge[26, 11]. The 2D Hall thruster discharge has been chosen here as the basis to formulate the 1D radial model for a flowing plasma. However, we believe this formulation to be general enough to apply to other flowing plasmas interacting with two walls. In order to emphasize this last point and to free the radial model from the Hall thruster case, the derivation of the 1D radial model from the 2D axisymmetric model of the discharge has been confined to Appendix A.

In a recent paper on a 2D model of the Hall thruster, Keidar *et al.*use a presheath/sheath model for the lateral walls[37]. They claim that for a smooth presheath/sheath solution the radial ion velocity at the sheath transition must be *smaller* than the (sonic) Bohm velocity, in contradiction to the well established sheath theory between a wall and a plasma[54, 48]. The main arguments supporting the sonic transition are recalled in Appendix B here. Comments on other aspects of Keidar's paper, like their results on the interaction between the axial and radial responses are out of the scope of this paper.

The rest of the paper is organized as follows. In Sec. II we formulate the radial model, the boundary and compatibility conditions, and the integration procedure. In Sec. III we discuss solutions for different cases and geometries. Conclusions are presented in Sec. IV.

1.2 MODEL FORMULATION

1.2.1 The quasineutral presheath

Figure 1.1 sketches the situation on an axial cross-section of an annular chamber. The plasma is supposed to flow axially between two long dielectric walls placed, in cylindrical coordinates (x, r, θ), at $r = r_{W'}$ and $r = r_W = r_{W'} + h$, with h the channel width. We consider the zero Debye-length limit, $\lambda_d/h \to 0$, allowing a two-scale, presheath/sheath analysis, where h and λ_d

are the distinguished scales of the presheath and sheath, respectively. From Appendix A, the pertinent 1D fluid equations in the presheath are

$$\frac{1}{r}\frac{\partial}{\partial r} r n_i v_{ri} = \nu_w n_i, \tag{1.1}$$

$$m_i n_i v_{ri}\frac{\partial v_{ri}}{\partial r} = -\frac{\partial}{\partial r}(n_i T_i) - e n_i \frac{\partial \phi}{\partial r} - \nu_r m_i n_i v_{ri}, \tag{1.2}$$

$$\frac{1}{r}\frac{\partial}{\partial r}(r\frac{3}{2}T_i n_i v_{ri}) + \frac{T_i n_i}{r}\frac{\partial}{\partial r}(r v_{ri}) = \nu_i \frac{1}{2} m_i n_i v_{ri}^2 + \nu_t n_i T_i, \tag{1.3}$$

$$n_e = \text{const} \times \exp(e\phi/T_e), \tag{1.4}$$

$$n_e = n_i. \tag{1.5}$$

Here: ν_i, ν_w, ν_r, ν_t are frequencies for ionization, ion net production, effective radial friction, and axial energy contribution, respectively, defined in Eq. (A.7). We assume these frequencies to be known functions of r in any axial position. Moreover, we restrict the discussion here to $\nu_j(r) = \text{const}, (j = i, w, r, t)$, because there are no fundamental novelties when treating more general profiles (see Ref. [23] and comments in Sec III.A).

Operating with the above equations, the radial problem in the presheath reduces to integrate the two coupled equations

$$\begin{aligned}(T_e + \frac{5}{3}T_i - m_i v_{ri}^2)\frac{\partial v_{ri}}{\partial r} &= (\nu_r + \frac{\nu_i}{3}) m_i v_{ri}^2 \\ &\quad - (T_e + \frac{5}{3}T_i)\frac{v_{ri}}{r} + \nu_w (T_e + \frac{5}{3}T_i) + (\frac{2}{3}\nu_t - \frac{5}{3}\nu_w) T_i,\end{aligned} \tag{1.6}$$

$$\frac{3}{2} v_{ri}\frac{\partial T_i}{\partial r} = \nu_i \frac{1}{2} m_i v_{ri}^2 - T_i\Big(\frac{\partial v_{ri}}{\partial r} + \frac{v_{ri}}{r}\Big) + \nu_w T_i + (\nu_t - \frac{5}{2}\nu_w) T_i, \tag{1.7}$$

plus one differential equation for the electric potential,

$$v_{ri}\frac{\partial}{\partial r}(\frac{e\phi}{T_e}) = \nu_w - \frac{1}{r}\frac{\partial}{\partial r}(r v_{ri}), \tag{1.8}$$

which corresponds to the so-called *plasma equation* in kinetic models[54].

Equation (1.6) shows that radial derivatives become singular at

$$|v_{ri}| = c_s(T_i) \equiv \sqrt{\frac{T_e + \frac{5}{3}T_i}{m_i}}, \tag{1.9}$$

with c_s the local sound velocity of the plasma. In particular, the electric field, $d\phi/dr$, becomes infinite there, indicating the failure of the quasineutral approximation and the transition from the large h-scale to the thin λ_d-scale of the sheath. Therefore,

$$v_{riQ} = c_{sQ}, \quad v_{riQ'} = -c_{sQ'}, \tag{1.10}$$

are the Bohm conditions defining the transition points (Q and Q′ Fig. 1.1) to the outer and inner non-neutral sheaths. In Appendix B we show that these transition conditions are the only valid ones.

The electric potential must present a maximum at some intermediate position of the channel (point M in Fig. 1.1), $\partial\phi/\partial r|_M = 0$. A local expansion of Eqs. (1.6)-(1.8) around point M yields

$$\begin{aligned} v_{ri}(r) &= \nu_w(r - r_M) + O[(r - r_M)^2], \\ T_i(r) &= T_{iM} + O[(r - r_M)^2], \end{aligned} \tag{1.11}$$

and the compatibility condition

$$\nu_t = 5\nu_w/2. \tag{1.12}$$

As Eq. (A.9) in Appendix A confirms, this condition corresponds to the correct balance between the radial and axial energy fluxes for ions.

Condition (1.12) makes identically zero the last term of each of the equations (1.6) and (1.7). Then, for the zero-ionization case ($\nu_i = 0$), Eqs. (1.1) and (1.3) yield the isentropic law

$$\frac{T_i}{n_i^{2/3}} = \text{const}, \tag{1.13}$$

which substitutes to Eq. (1.7).

Convenient dimensionless variables to integrate Eqs. (1.6)-(1.8) are

$$\tilde{r} = \frac{r}{h}, \quad \tilde{T}_i = \frac{T_i}{T_e}, \quad \tilde{\phi} = \frac{e(\phi - \phi_M)}{T_e}, \quad \tilde{v}_{ri} = \frac{v_{ri}}{\sqrt{T_e/m_i}}, \quad \tilde{\nu}_j = \frac{\nu_j}{\nu_0} \ (j = i, w, r, t), \tag{1.14}$$

with

$$\nu_0 = h^{-1}\sqrt{T_e/m_i} \tag{1.15}$$

the characteristic frequency for radial processes. The convenient integration procedure departs from point M towards points Q and Q′, using the expansions of Eq. (1.11) as initial conditions. The two independent integrations end where Bohm conditions (1.10) are satisfied, and determine $\tilde{r}_Q$ and $\tilde{r}_{Q'}$ in terms of five input parameters: $\tilde{T}_{iM}$, $\tilde{r}_M$, $\tilde{\nu}_i$, $\tilde{\nu}_r$, and $\tilde{\nu}_w$, while $\tilde{\nu}_t$ satisfies Eq. (1.12).

The sheaths thicknesses are of the order of the Debye length. Thus, in the zero Debye-length limit, the sheaths are seen as two surface discontinuities in the presheath scale:

$$r_W \simeq r_Q, \quad r_{W'} \simeq r_{Q'}. \tag{1.16}$$

Since the channel width is known, the presheath solution must satisfy the condition

$$\tilde{r}_Q - \tilde{r}_{Q'} = 1.$$

This implies an extra relation among the above five input parameters. After exchanging $\tilde{r}_M$ by the annular ratio

$$\beta = r_{W'}/r_W,$$

as known parameter, the extra relation leads to a relationship

$$\tilde{\nu}_w = \tilde{\nu}_w(\tilde{\nu}_i, \tilde{\nu}_r, \tilde{T}_{iM}, \beta). \tag{1.17}$$

This is the generalized form of the Tonks-Langmuir plasma balance equation for flowing plasmas and annular geometries; the limits $\beta \to 1$ and $\beta = 0$ correspond to the planar and cylindrical cases, respectively.

The comparison of the present model, Eqs. (1.1)-(1.5), with those of Refs. [16] and [50], shows that these ones cover only the cases i) $\beta = 1$ (i.e., a planar geometry) and ii) $\nu_r = \nu_i = \nu_w$ (i.e., a no flowing plasma). Therefore, the four free parameters of Eq. (1.17) are reduced in their case to just one: $\tilde{T}_{iM}$. Also, these no-flowing models use $\nu_i \frac{3}{2} T_n$ in Eq. (1.3) instead of $\nu_t T_i$, which agrees with Eq. (A.7) for the no-flowing case. This difference in the heating term has interesting consequences on the balance/compatibility condition for the internal energy. In our model, the term $\nu_t T_i$ leads to the compatibility condition (1.12), which states that the radial heating frequency, ν_t, depends on the radial production/loss frequency, ν_w, whereas the value of T_{iM} is *free* (which agrees with the idea of T_{iM} depending partially on the axial discharge conditions). On the contrary, in the no-flowing models of Refs. [16] and [50], which do not include the heating frequency ν_t (that is, they neglect any axial contribution to ion heating), the balance/compatibility condition *fixes* the value of T_{iM} (as proportional to T_n). [Differences in the definitions of the ion temperature in the different models have no relevant consequences and have then been ignored in the preceding discussion.]

1.2.2 The sheaths

The role of the two radial sheaths, $W'Q$ and QW in Fig. 1.1, is to provide the potential drop needed to maintain the zero-current condition at the wall. For the zero Debye-length limit, the sheaths are collisionless boundary layers perpendicular to the walls. The 2D Poisson equation, Eq. (A.11), reduces to the 1D radial form, Eq. (B.1), and plasma equations (1.1)-(1.5) become algebraic, conservation relations for the fluxes of different plasma magnitudes. In particular and taking the case of the outer sheath, the ion density flux to the outer wall, $g_{riW} = (n_i v_{ri})_W$, satisfies

$$g_{riW} = g_{riQ} = n_{iQ} c_{sQ}, \tag{1.18}$$

with $n_{iQ} = n_{iM} \exp(-e\phi_{QM}/T_e)$ and $\phi_{QM} = \phi_M - \phi_Q$ the potential drop at the presheath.

For no secondary emission at the walls and a semi-Maxwellian distribution of the electrons, the zero current condition follows

$$g_{riQ} = n_{eQ} \exp\big(-\frac{e\phi_{WQ}}{T_e}\big)\sqrt{\frac{T_e}{2\pi m_e}}, \tag{1.19}$$

with $\phi_{WQ} = \phi_Q - \phi_W$ the potential drop at the sheath. Solving for ϕ_{WQ}, one has

$$\frac{e\phi_{WQ}}{T_e} = \frac{1}{2}\big[\ln\frac{m_i}{2\pi m_e} - \ln\big(1 + \frac{5T_{iQ}}{3T_e}\big)\big]. \tag{1.20}$$

For all practical values of T_{iQ}/T_e, the last term on the right can be disregarded, so that the sheath potential drop is practically independent of the presheath solution.

The above expressions relate the main sheath parameters. The Poisson equation (B.1) needs to be solved only to determine the spatial structure of the sheath and to find, in a way equivalent to that used in Appendix B, that the (outer) sheath solution exists only for $v_{riQ} \geq c_{sQ}$.

1.3 PLANAR AND ANNULAR SOLUTIONS

1.3.1 Planar geometry: cold ions

We consider first the simple case

$$\beta \to 1, \quad \tilde{T}_{iM} = 0, \quad \tilde{\nu}_i \to 0. \tag{1.21}$$

The first condition implies that the channel is quasiplanar (satisfying $1/r \ll \partial/\partial r$), so that the presheath is composed by two symmetric regions, with $r_M = (r_Q + r_{Q'})/2$ the channel mid-point, and we just need to solve the region MQ. The second and third conditions yield $\tilde{T}_i(r) = \text{const} = 0$ as the solution of Eq. (1.7).

For the basic 'no-friction' case, $\tilde{\nu}_r = 0$, the velocity and potential profiles [Eqs. (1.6) and (1.8)] satisfy

$$\tilde{v}_{ri} - \tilde{v}_{ri}^3/3 = (\tilde{r} - \tilde{r}_M)\tilde{\nu}_w, \qquad \tilde{\phi} = -\tilde{v}_{ri}^2/2. \tag{1.22}$$

Setting $\tilde{v}_{riQ} = 1$ at $\tilde{r}_Q = \tilde{r}_M + 1/2$ [Eq. (1.10)] one has

$$\tilde{\nu}_w = 4/3, \tag{1.23}$$

which is the plasma balance condition for this basic case. It states that the total production frequency is fixed by the channel width and the plasma temperature. Notice that the plasma balance condition is the consequence of two facts: (a) wall electrical properties imply the presence of a thin non-neutral sheath; and (b) the transition to this sheath requires the ion flow to be sonic.

[Were not the frequency profile $\nu_w(r)$ constant, $(\tilde{r}-\tilde{r}_M)\tilde{\nu}_w$ in Eq. (1.22) should be substituted by $\int_{\tilde{r}_M}^{\tilde{r}} \tilde{\nu}_w(\tilde{r}')d\tilde{r}'$, and the balance condition would yield $\int_{\tilde{r}_{W'}}^{\tilde{r}_W} \tilde{\nu}_w(\tilde{r}')d\tilde{r}' = 4/3$. Since v_{ri} must be zero at point M and equal to $\pm c_s$ at the walls, the shape of $\nu_w(r)$ modifies only the local gradients of $v_{ri}(r)$: when ν_w tends to concentrate around point M, v_{ri} tends to present an intermediate inflexion point[23]. In any case, since the shape of $\nu_w(r)$ depends on both the axial flux and the ionization rate, very steep shapes are unlike.]

For the positive 'friction' case $\tilde{\nu}_r > 0$, Eqs. (1.6) and (1.8) yield

$$\frac{1+\alpha_r}{\sqrt{\alpha_r}} \arctan(\tilde{v}_{ri}\sqrt{\alpha_r}) - \tilde{v}_{ri} = \alpha_r \tilde{\nu}_w (\tilde{r} - \tilde{r}_M), \tag{1.24}$$

$$\tilde{\phi} = -\frac{1+\alpha_r}{2\alpha_r} \ln(1 + \alpha_r \tilde{v}_{ri}^2), \tag{1.25}$$

with $\alpha_r = \nu_r/\nu_w$ a convenient parameter[9]. Setting $\tilde{v}_{riQ} = 1$ at $\tilde{r} = \tilde{r}_M + 1/2$, one obtains the plasma balance condition relating now $\tilde{\nu}_w$ to $\tilde{\nu}_r$. Figures 1.2(a)-1.2(c) (case $\tilde{T}_{iM} = 0$ and $\tilde{\nu}_i = 0$) show the evolution, with the friction frequency, of the production frequency, the potential drop at the presheath, and the plasma current to the wall. For $\tilde{\nu}_r \to 0$, one recovers $\tilde{\nu}_w = 4/3$ and $\tilde{\phi}_{QM} = 1/2$; for $\tilde{\nu}_r \gg 1$, one has $\tilde{\nu}_w \simeq \pi^2/\tilde{\nu}_r$ and $\tilde{\phi}_{QM} \simeq \ln \tilde{\nu}_r$. These results indicate that larger ion frictions (i) mean larger potential and density drops across the channel in order to bring the ion flow to the sonic condition, $\tilde{v}_{riQ} = 1$, at the sheath tied to the wall, and (ii) yield lower production frequencies. Therefore, the axial motion turns out to be an efficient mechanism to inhibit the plasma losses to the wall.

However, the ion axial motion can lead to negative values of $\tilde{\nu}_r$ too, which increase the plasma current to the wall. For $\tilde{\nu}_r < 0$, $\tilde{v}_{ri}(\tilde{r}, \tilde{\nu}_r)$ and $\tilde{\nu}_w(\tilde{\nu}_r)$ satisfy

$$v_{ri} + \frac{1+\alpha_r}{2|\alpha_r|^{1/2}} \ln \frac{1 - v_{ri}|\alpha_r|^{1/2}}{1 + v_{ri}|\alpha_r|^{1/2}} = |\alpha_r| \tilde{\nu}_w (\tilde{r} - \tilde{r}_M), \tag{1.26}$$

and Eq. (1.10). These relations show that $\partial \nu_w / \partial(-\nu_r) > 0$, but solutions with negative friction exist only up to $\tilde{\nu}_r = -2$ (yielding $\tilde{\nu}_w = 2$). Were $-\tilde{\nu}_r > 2$, the plasma velocity would not reach the Bohm velocity, Eq. (1.10), and a steady radial solution would not form.

1.3.2 Planar geometry: general solution

To solve numerically Eqs. (1.6)-(1.8) for $\tilde{\nu}_i > 0$, $\tilde{T}_{iM} > 0$, and $\beta = 1$, we use the spatial variable $\xi = \tilde{\nu}_w(\tilde{r} - \tilde{r}_M)$ and the ratios $\alpha_j = \nu_j / \nu_w$ $(j = r, i)$. The integration from points M to Q yields the relation $\tilde{\nu}_w = 2\ \xi_Q(\alpha_r, \alpha_i, \tilde{T}_{iM})$, where from the plasma balance condition $\tilde{\nu}_w = \tilde{\nu}_w(\tilde{\nu}_r, \tilde{\nu}_i, \tilde{T}_{iM})$ is obtained.

The comparison of the solid and dash-dot lines in Figs. 1.2(a)-1.2(d) illustrates the effect of warm ions on zero-ionization situations. First, since the plasma sound speed increases with $\tilde{T}_{iM}$, one has that $\tilde{\nu}_w$ and wall losses increase too. Second, for $\tilde{\nu}_i = 0$, $T_i(r)$ decreases towards the walls following the isentropic law (1.13) and yielding

$$T_{iQ}/T_{iM} = \exp(-3\tilde{\phi}_{QM}/2) < 1.$$

Figure 1.3 and the dashed line of Figs. 1.2(a)-1.2(d) illustrate the influence of ν_i for different values of ν_i/ν_r. Although ν_i contributes to ν_r [Eq. (A.7)], for the present discussion it is convenient to take them as independent parameters. Then, Figs. 1.2(a) and 1.2(b) indicate that ν_r, and not ν_i, determine the net production frequency. The main effect of ν_i is to increase the dispersion of ion velocities, that is the ion temperature. Figure 1.4 shows the competition between the cooling effect of ion rarefaction, Eq. (1.13), the ion heating due to (and increasing with) ionization.

The no axial-flow case: $\tilde{\nu}_w = \tilde{\nu}_r = \tilde{\nu}_i$, treated by Tonks and Langmuir and Refs. [16] and [50], corresponds to a *single* solution point for each $\tilde{T}_{iM}$; these are the asterisks marked in Fig. 1.3. As Tonks and Langmuir explained (for $\tilde{T}_{iM} = 0$), the plasma balance condition in the no axial-flow case determines totally the ionization frequency, ν_i, and, therefore, the electron temperature. In cases where the axial flow is relevant (like the plasma discharge in a Hall thruster), T_e is determined by the axial energy balance mainly[10], and the difference between $\nu_i(T_e)$ and the total production frequency, $\nu_w(T_e, h)$ is provided by the axial variation of the ion axial flux [Eq. (A.8)]. Finally, notice that in the Tonks-Langmuir problem, a steady-state plasma discharge requires ν_w to be less than the absolute maximum of $\nu_i(T_e)$, whereas in a plasma flowing axially, the steady-state solution relies more on axial conditions.

1.3.3 Annular geometry

In this general case the convenient integration variable of Eqs. (1.6)-(1.8) is $\eta = \tilde{r}\tilde{\nu}_w$. The separate integrations of the presheath equations from point M towards points Q and Q′, which includes η_M as an input parameter, yields $\eta_{Q'}$ and η_Q as functions of η_M, α_r, α_i, and $\tilde{T}_{iM}$. Then, using the two equalities

$$\tilde{\nu}_w = \eta_Q - \eta_{Q'} = \eta_Q/\tilde{r}_Q, \tag{1.27}$$

the plasma balance condition in the form of Eq. (1.17) is obtained.

Figures 1.5(a)-1.5(c) depict spatial profiles of different magnitudes for zero-ionization cases ($\nu_i = 0$) and different annular ratios. Point M tends to drift towards the inner wall as β decreases, yielding two asymmetric presheaths, with steeper gradients in the inner one, as Tonks and Langmuir deduced. Plasma gradients tend to diverge as $\beta \to 0$, but the solution cannot be continued down to $\beta = 0$ (i.e., a cylindrical chamber), since then point M coincides with the channel axis and the inner presheath disappears.

For $\nu_i = 0$, the ion temperature follows the isentropic law (1.13). Consequences of this and the Bohm conditions (1.10), are $v_{riQ} = v_{riQ'}$ and $n_{iQ} = n_{iQ'}$, independently of β. Therefore, in spite of the presheath asymmetry, one has equal wall currents and potential drops in both presheaths,

$$\nu_i = 0: \qquad g_{riW} = g_{riW'}, \quad \phi_{Q'M} = \phi_{QM}.$$

Figures 1.6(a)-1.6(c) show, for different β, the evolution with ν_i of the main parameters of the inner and outer presheaths. In Fig. 1.6(a) we see that $\tilde{\nu}_w$ is affected weakly by the annular ratio, β; notice that, similar to Fig. 1.3, the no axial-motion case corresponds to just one point: $\tilde{\nu}_w = \tilde{\nu}_i$, for each β-line. Figures 1.6(b) and 1.6(c) show that for $\nu_i > 0$ and $\beta < 1$, wall currents and potential drops are different in the two presheaths. Differences increase as β decreases; departures from the planar solution become relevant for $\beta < 0.7$, roughly. Taking as a reference the planar case, potential drops tend to be smaller in the inner presheath and larger in the outer one [Fig. 1.6(b)] whereas plasma currents [Fig. 1.6(c)] follow the opposite behavior. The sheath solution (1.20) indicated that presheath asymmetries of an annular chamber do not produce further asymmetries in the inner and outer sheaths. In conclusion, in an annular chamber with non-zero ionization the particle and energy fluxes are larger at the inner wall than at the outer one.

Ion temperatures at points Q and Q′ for the cases of Fig. 1.6 are about $0.4 - 0.5T_e$ and their dependence on $\tilde{\nu}_r$ and β follow the trends of the respective potential drops. For $\tilde{\nu}_i = 0$, $\tilde{\nu}_r > 0$, and the rest of conditions the same as in Figs. 1.6, results are very similar to those of Figs. 1.6, except for the ion temperatures, which are smaller due to the isentropic behavior, Eq. (1.13).

1.4 SUMMARY

A model of the radial structure of a plasma flowing along two dielectric walls must take into account the contributions of the axial flow into the radial equations. In a macroscopic formulation, this can be done by including three terms, representing a particle source, an effective friction, and an internal energy source in the equations of continuity, momentum, and energy, respectively. The production/loss of ions may come from either ionization or the axial flow; the effective radial friction comes from both ionization and the axial variation of the radial velocity; and the internal energy of the axial flow contributes to the energy balance. Compared to the classical model of Tonks-Langmuir (and its macroscopic versions) the present model has three new parameters (or degrees of freedom): a net ion production/loss frequency, ν_w, (which is independent of the ionization frequency, ν_i), a frequency for ion radial friction, ν_r, and the ion temperature, T_{iM}, at the point separating inner and outer radial flows.

The plasma balance condition of Tonks-Langmuir stated that geometrical magnitudes determined ν_i and, as a result, the electron temperature. In the present model, the plasma balance condition yields ν_w as a function of the effective radial friction, the ionization rate, the temperature T_{iM}, and geometrical magnitudes, whereas T_e remains a free parameter (to be determined from the axial conditions of the discharge). The investigation of the plasma balance condition reveals two important conclusions. First, ν_w, beyond being proportional to the channel width, depends significantly on ν_r in a way such that a strong radial friction can reduce significantly the loss of plasma current into the lateral walls. And second, ν_i has practically no direct influence on ν_w; the indirect influence comes from the contribution of ν_i to ν_r.

The equation for the ion internal energy includes two source terms: one due to the velocity dispersion of the ion fluid because of ionization, and the second one coming from the mean temperature of the ion sources (ionization and axial flow). As a consequence, T_{iM} is partially independent of the temperature of the neutral gas, T_n. Regarding the thermodynamic response of the ions, it is shown that: (i) an isothermal behavior exists only for the zero-ionization and zero-temperature limit; (ii) an isentropic response takes place for zero-ionization, with radial rarefaction producing ion cooling; and (iii) for $\nu_i > 0$ and $T_{iM} > 0$, heating due to ionization competes with the rarefaction cooling in shaping the ion temperature profile.

The analysis of channels with different annular ratios, shows that asymmetries between the profiles of the inner and outer presheaths are relevant for $\beta < 0.7$, roughly. Point M of maximum potential moves towards the inner wall as β decreases, and plasma gradients are larger in the inner presheath. In spite of that presheath asymmetry, for $\nu_i = 0$ the potential drops and the currents into the walls are the same in the inner and outer presheath. For $\nu_i \geq O(1)$, smaller potential drops and larger wall currents are found in the inner presheath. Plasma currents remain constant inside the sheaths and the sheath potential drops are practically independent of the presheath solution.

To get an idea of the practical relevance of the different parameters controlling the presheath solution typical values for a SPT-100 type of Hall thruster are $\beta \sim 0.7$, $\tilde{T}_{iM} \ll 1$, $\nu_0 \sim 2-4 \times 10^5 \mathrm{s}^{-1}$, $\tilde{\nu}_i \sim 1$ in the ionization region and $\tilde{\nu}_i \ll 1$ outside it, and $\tilde{\nu}_r \sim 1$ in most of the channel[7].

Finally, research is pursued in two directions. First, ceramic materials may present a secondary emission yield of order unity[55, 36], which is not immediate to include in a presheath/sheath model between two walls[9]. Second, to determine completely the conditions of the plasma discharge requires the simultaneous solving of the coupled radial and axial models[7].

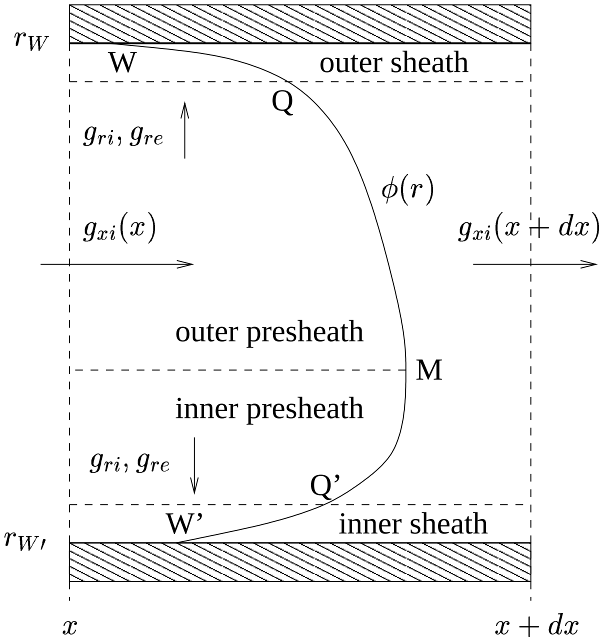
r_W
W
outer sheath
Q
g_{ri}, g_{re}
$\phi(r)$
$g_{xi}(x)$
$g_{xi}(x + dx)$
outer presheath
M
inner presheath
g_{ri}, g_{re}
Q'
W'
inner sheath
$r_{W'}$
x
$x + dx$

Figure 1.1: A generic radial section of a long annular channel between two dielectric walls. $g_{xi} = n_{xi}v_{xi}$ and $g_{ri} = n_{ri}v_{ri}$ represent axial and radial particle fluxes; $\phi(r)$ sketches the radial profile of the electric potential, which is maximum at point M. The transitions to the sheaths are at points Q and Q$'$. Since the presheath/sheath structure corresponds to the zero Debye-length limit one has $r_W = r_Q$ and $r'_W = r'_Q$.

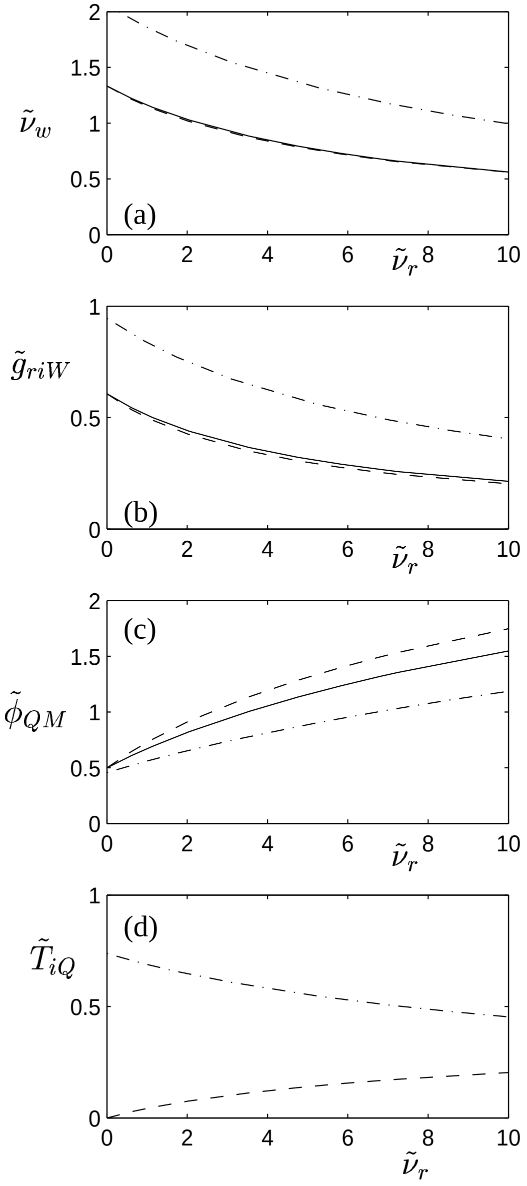

Figure 1.2: Planar geometry: Evolution of plasma parameters with $\tilde{\nu}_r$ for $(\tilde{T}_{iM}, \nu_i) = (0, 0)$[solid line], $(1, 0)$[dash-dot line], and $(0, \nu_r)$[dashed line]. The dimensionless particle flux is $\tilde{g}_{ri} = (n_{iM}\sqrt{T_e/m_i})^{-1} g_{ri}$.

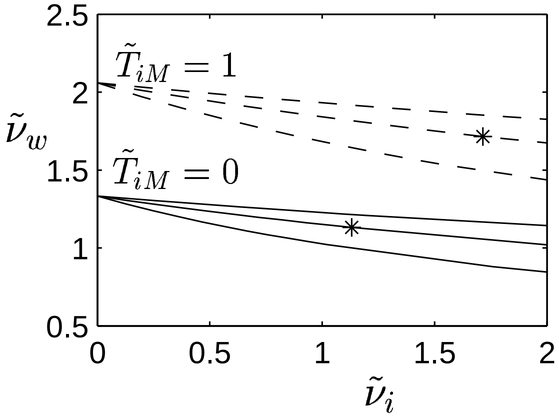

Figure 1.3: Planar geometry: Net production frequency versus ionization frequency for $\tilde{T}_{iM} = 0$(solid lines) and 1(dashed lines) and $\nu_i/\nu_r = 0.5, 1$ and 2 (from bottom to top for each $\tilde{T}_{iM}$). The asterisks correspond to the no-flowing case, $\nu_w = \nu_i = \nu_r$.

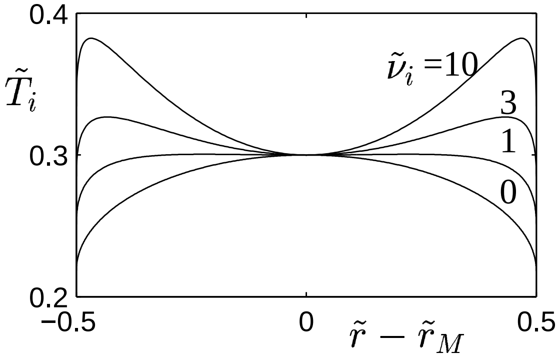

Figure 1.4: Planar geometry: Radial profile of ion temperature for $\tilde{T}_{iM} = 0.3$, $\tilde{\nu}_r = \tilde{\nu}_i$, and four ionization frequencies: $\tilde{\nu}_i = 0, 1, 3$ and 10.

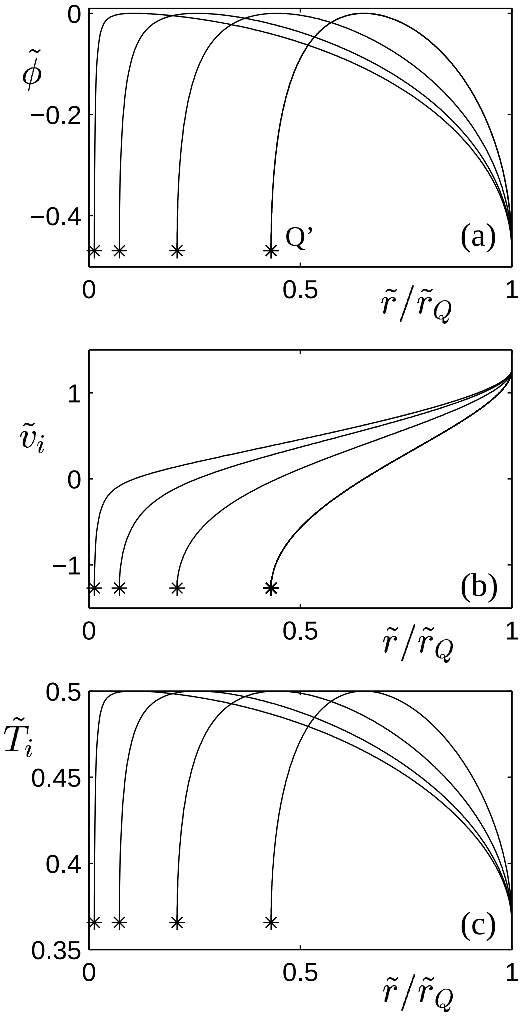

Figure 1.5: Annular geometry: Plasma profiles for different annular ratios ($r'_Q/r_Q \simeq 0.013$, 0.072, 0.21, 0.43), $\tilde{T}_{iM} = 0.5$, and $\tilde{\nu}_r = \tilde{\nu}_i = 0$. Points Q$'$ are at the asterisks; points M are at $d\phi/dr|_M = 0$ (and $v_{ri} = 0$) separating the inner and outer presheaths.

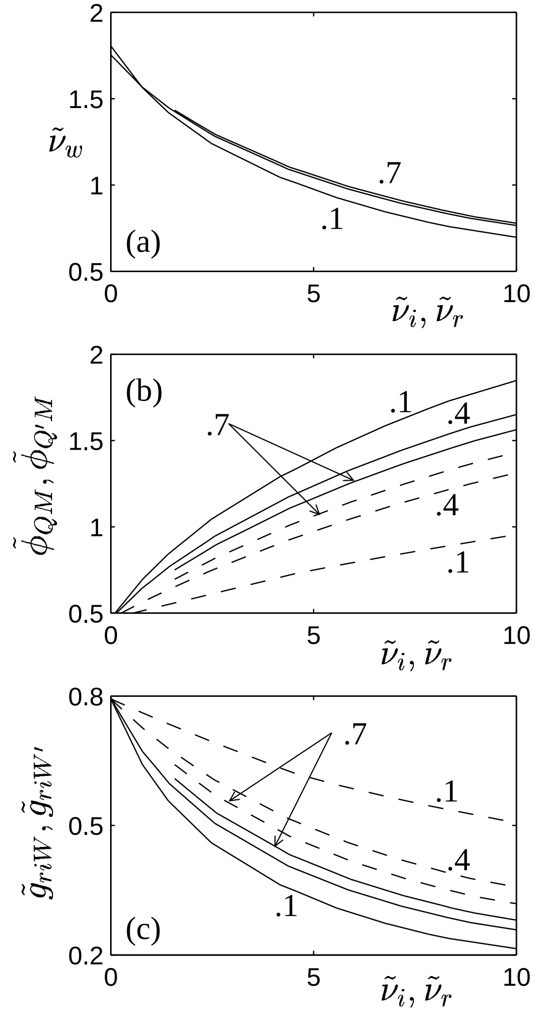

Figure 1.6: Annular geometry: Evolution of main plasma parameters with $\tilde{\nu}_i$ for $\tilde{T}_{iM} = 0.5$, $\nu_r = \nu_i$ and three annular ratios, $\beta = 0.1, 0.4$ and 0.7. In (b) and (c) solid lines correspond to the outer presheath, and dashed lines to the inner presheath.

Chapter 2

RADIAL MODEL WITH SECONDARY EMISSION

2.1 INTRODUCTION

The transverse (or radial) interaction of a collisionless plasma with two dielectric walls confining it was treated originally by Tonks and Langmuir[54]. They develop the sheath/presheath theory for the zero-Debye length asymptotic limit and solved the fundamental issues of the problem. In Tonks-Langmuir model and posterior papers complementing it, [33, 23, 16, 50] the ion and electron losses to the walls are balanced by volume ionization. In Ch. 1 we generalized that model to plasmas flowing longitudinally between planar or annular walls. The presheath problem depends then on two new parameters related to the axial flow, and it is shown that (i) in the absence (or excess) of ionization, the axial flow balances the radial losses of particles to the walls, and (ii) axial gradients introduce a friction effect on the radial acceleration of the ions, which leads to larger potential drops in the presheath and lower losses to the walls.

All the above models consider implicitly a passive (or non-emitting) wall. However, in many cases electron emission by the wall is important. For certain ceramic materials, electron impact produces secondary emission yields (the ratio between the secondary and primary fluxes at the wall) above 100% [43, 36]. Secondary electrons interact with the electrostatic field and the main plasma and modify sheath and presheath characteristics. The collisionless sheath with secondary emission was studied by Hobbs and Wesson[34], who demonstrated that the sheath becomes charge-saturated for a secondary emission yield close to 100%. However, they studied the sheath exclusively, and they did not match it to any model for the bulk of the plasma. To close the sheath equations, they impose the usual quasineutrality and sonic (i.e. Bohm) conditions at the sheath/plasma boundary.

Schwager formulated a planar, kinetic model with secondary emission of the region between one emitting wall and a source- or edge-plasma [51]. That region consisted of a (negative) wall sheath, followed by a quasineutral region, and a (positive) sheath close to the edge-plasma. Stephens and Ordoñez studied practically the same model [52], and Jolivet and Roussel apply the last one to the case of a Hall thruster [36]. In these three models, secondary electrons are assumed to accelerate freely across the whole plasma region between the emission wall and the edge-plasma. The secondary population is thermalized at the edge-plasma and re-emitted back as primary electrons to the central plasma region. This wall plus edge-plasma model does not reproduce satisfactorily the case of a plasma confined between two walls, with no intermediate edge-plasma. In particular, this edge-plasma does not act as a 'symmetry mirror' in a planar geometry: (i) the solution for the secondary population is not symmetric, since that population would be 'free' in half-channel and 'thermalized' in the other half; and (ii) the edge-plasma tends to create a sheath-like region close to it which is not expected in the usual two-wall case.

As the works just commented suggest, the main difficulty lies in the treatment of the secondary electrons in the bulk of the plasma. In a recent conference we proposed that a consistent presheath/sheath theory with secondary emission could be developed by treating differently the electron populations in each region [9]. The present chapter develops in detail that model. The two main pieces of it will be the Hobbs-Wesson model for the sheath (extended here to the case of warm ions) and our presheath model for flowing plasmas and two annular walls.

An application of the resulting model, which is of particular interest to us, is the plasma discharge in a Hall thruster chamber made of ceramic walls. The discharge is axisymmetric and particle and energy losses to the walls are known to affect greatly the thruster performance [46, 26, 38, 7]. Therefore, a good understanding of the radial plasma-wall interaction is crucial to predict correctly the axial response of the discharge.

The rest of the chapter is organized as follows. In Sec. II we formulate the main hypotheses of the model. In Sec. III we discuss the sheath solution. In Sec. IV we match the presheath model to the sheath solution and we compute results for the complete solution. In Sec. V we discuss the main results.

2.2 MODEL FORMULATION

Figure 2.1(a) sketches the radial model. The plasma flows between two annular walls placed, in cylindrical coordinates (x, r, θ), at $r = r_{W'}$ and $r = r_W = r_{W'} + h_c$, with h_c the channel width. Here, we are interested in the radial structure of the plasma discharge at a given axial position x. For dielectric walls, the zero current condition implies, in general, the potential profile $\phi(r)$ to present a maximum at a central point of the channel [point M in Fig. 2.1(a)] and to decrease monotonically towards the two walls [points W and W']. Except for very large voltages, secondary electron emission is due mainly to the impact of those electrons from the main population with enough energy to reach the walls. Depending on their posterior evolution inside the plasma, secondary electrons can be divided in two basic types: (i) a 'free' group constituted by those crossing the plasma from the emission wall and being collected back at the opposite wall, without interacting with other particles, and (ii) a 'trapped' group formed by those suffering occasional collisions with other particles and multiple electrostatic reflexions within the confining potential $\phi(r)$, until they thermalize with the bulk electron population.

The 'free' secondary population is simple to model; on the contrary, at each instant of time, there are 'trapped' secondary electrons with different temporal histories. The crucial issue of any stationary model is to figure out which is the temporally-averaged collective distribution of this trapped population. Our proposal is to take advantage of the presheath/sheath theory and of a macroscopic formulation for a dual treatment of the 'trapped' secondary electrons. The presheath/sheath theory applies to the zero Debye-length limit,

$$\lambda_d \ll h_c, \lambda_{col}, \tag{2.1}$$

with λ_d the Debye length, and λ_{col} the relevant mean free-path for collisional processes. The advantage of using this two-scale analysis is based on three features: (i) the sheaths are treated as surface discontinuities in the quasineutral scale, but as as collisionless and ionization-free regions in their inner scale; (ii) presheath and sheaths are solved separately in their own scales, and then matched at the presheath/sheath transition; and (iii) the matching or transition condition is unique and, for a plasma with zero radial flow somewhere in the presheath, consists of the sonic Bohm condition [40, 3].

The model we propose for the plasma is based in the following hypotheses:

(i) Within the thin, collisionless sheaths there are two independent electron populations: population p of primary, confined electrons coming from the bulk of the plasma and population s of secondary, wall-emitted electrons. Population s is accelerated freely by the sheath potential from the wall to the presheath boundary.

(ii) We consider that $\lambda_{col} \ll h_c$, so that all secondary electrons remain trapped in the bulk of the plasma. [This restricts the present model to the total-trapping case.]

(iii) Within the presheath, all (trapped) electrons, irrespective of their origin (ionization, axial flow, or wall-emission), are grouped in a single population e.

(iv) There is a unique population (i) of ions in sheath and presheath. Quasineutrality in the presheath means $n_i \simeq n_e$ at every point (and not just globally, as Ref. [52] states).

(v) To match consistently the solutions of presheath and sheaths three basic laws are imposed at each presheath/sheath transition: the conservation of the total electron density, the conservation of the net electron flux, and the continuity of the ion flux.

2.3 SHEATH ANALYSIS

2.3.1 Sheath solution

In general, we will refer the discussion only to the sheath tied to the outer wall; the inner sheath behaves in the same way. The outer sheath extends from the the wall (point W) to the presheath transition (point Q). If the sheath is not charge-saturated the electric potential is monotonic with $\phi_{WQ} = \phi_Q - \phi_W > 0$. In the zero Debye-length limit of Eq. (2.1), the sheath satisfies the conservation equations,

$$n_i v_{ri} = \text{const} = g_{ri}, \tag{2.2}$$

$$\frac{1}{2} m_i v_{ri}^2 + \frac{5}{2} T_i + e\phi = \text{const}, \tag{2.3}$$

$$T_i / n_i^{2/3} = \text{const}, \tag{2.4}$$

$$n_p = n_{pW} \exp \frac{e\phi - e\phi_W}{T_p}, \tag{2.5}$$

$$n_s v_{rs} = \text{const} = g_{rs}, \tag{2.6}$$

$$\frac{1}{2} m_e v_{rs}^2 - e\phi = \text{const}, \tag{2.7}$$

the flux conditions,

$$g_{ri} = g_{rp} + g_{rs}, \tag{2.8}$$

$$g_{rp} = n_{pW}\sqrt{T_p/2\pi m_e}, \tag{2.9}$$

$$g_{rs} = -\delta_w(T_p) g_{rp}, \tag{2.10}$$

and the (quasiplanar) Poisson equation,

$$\frac{\epsilon_0}{e}\frac{d^2\phi}{dr^2} = n_p + n_s - n_i. \tag{2.11}$$

The constants for the ion equations (2.2)-(2.4) are set at point Q and must match the values obtained at the presheath side. Since the wall temperature, T_w, is generally much smaller than the plasma temperature T_p, the mean energy of the secondary electrons when they leave the wall can be neglected (except in the very vicinity of point W) in Eq. (2.7). Equation (2.8) is the zero-current condition, and Eq. (2.9) corresponds to assume a quasi-Maxwellian distribution for population p.

In Eq. (2.10), the effective secondary emission yield of the wall, $\delta_w(T_p)$, depends on both T_p and the wall material. For the present purposes, a good-enough expression of the emission yield produced by a monoenergetic beam of energy E per electron is $\delta_w(E) \simeq \sqrt{E/E_w^0}$, with E_w^0 the temperature for 100% yield (in the range $E_w^0 \sim 10-100$V, say)[26, 36]. Averaging over the quasi-Maxwellian population p the effective yield satisfies

$$\delta_w(T_p) \simeq \sqrt{T_p/E_w}, \tag{2.12}$$

with $E_w \sim 0.57 E_w^0$. This last relationship allows us to use E_w/T_p instead of δ_w as input parameter for the sheath problem.

Equation (2.11) states that

$$\zeta = \frac{r - r_W}{\lambda_d}, \quad \text{with} \quad \lambda_d = \sqrt{\frac{\epsilon_0 T_p}{e^2 n_{iQ}}}, \tag{2.13}$$

is the natural spatial variable in the sheath. The integration of Poisson equation (2.11) together with Eqs.(2.4)-(2.7) yields the conservation equation

$$\frac{e^2 n_{iQ}}{2T_p}\left[\left(\frac{d\phi}{d\zeta}\right)^2 - \left(\frac{d\phi}{d\zeta}\right)_Q^2\right] = U(e\phi) - U(e\phi_Q) \tag{2.14}$$

with

$$U(e\phi) = n_p T_p + n_s m_e v_{rs}^2 + n_i(m_i v_{ri}^2 + T_i) \tag{2.15}$$

the Sagdeev's potential[45]. First and second derivatives of this function are

$$\begin{aligned} U'(e\phi) &= n_p + n_s - n_i, \\ U''(e\phi) &= \frac{n_p}{T_p} - \frac{n_s}{m_e v_{rs}^2} - \frac{n_i}{m_i v_{ri}^2 - \frac{5}{3}T_i}. \end{aligned} \tag{2.16}$$

Equation (2.14) states the balance of the dynamic and electric pressures of the whole plasma across the sheath. There are three boundary conditions related to Poisson equation. First, plasma quasineutrality at point Q means

$$U'_Q = 0. \tag{2.17}$$

Second, for a solution to exist around point Q with $|d\phi/d\zeta|$ increasing towards the wall, Eq. (2.14) requires that $U''_Q \geq 0$. In terms of the ion velocity (and neglecting the case $m_i v_{riQ}^2 < \frac{5}{3}T_{iQ}$ which does not lead to a valid solution at the wall) this condition is equivalent to

$$m_i v_{riQ}^2 \geq \frac{5}{3}T_{iQ} + T_p \frac{n_{pQ} + n_{sQ}}{n_{pQ} - n_{sQ}\dfrac{T_p}{2e\phi_{WQ}}}, \tag{2.18}$$

which is the sonic/supersonic Bohm condition for this three-species sheath. Since the quasineutral solution of the presheath accepts only a subsonic/sonic transition (see Sec. 2.4.2), the sonic condition

$$U''_Q = 0, \tag{2.19}$$

is the correct one for the sheath/presheath transition. Finally, the analysis of the transition region around point Q shows that the electric field, when measured in the sheath scale, tends asymptotically to zero at the sheath side of point Q,[40, 48]

$$\left.\frac{d(e\phi/T_p)}{d\zeta}\right|_Q \sim \frac{\lambda_d}{d} \to 0. \tag{2.20}$$

The preceding equations and conditions show that the dimensionless solution of the sheath depends on just two parameters, δ_w (or E_w/T_p) and $\hat{T}_{iQ} = T_{iQ}/T_p$. Hobbs and Wesson treated the case of cold ions, $\hat{T}_{iQ} = 0$. Figure 2(a) shows potential profiles for different emission yields and two ion temperatures. For a given potential, a warm ion population has a larger density and a lower velocity than a cold one, according to Eq. (2.3); this implies a smaller Debye length (i.

2.3.2 The charge-saturated regime(CSR)

Hobbs and Wesson showed (for $\hat{T}_{iQ} = 0$) that the sheath reaches the charge saturation limit(CSL) at the wall, characterized by $d(e\phi/T_p)/d\zeta\Big|_W = 0$, when the secondary yield and the potential drop are

$$\delta_w = \delta_w^* \simeq 1 - 8.3\sqrt{\frac{m_e}{m_i}}, \qquad \frac{e\phi_{WQ}}{T_p} = \hat{\phi}_{WQ}^* \simeq 1.02. \tag{2.22}$$

For warm ions (i.e. $\hat{T}_{iQ} > 0$), the situation is similar. We find that the ion temperature has an irrelevant influence on the value of δ_w at the CSL: for xenon, one has $\delta_w^* \simeq 0.983$ for $\hat{T}_{iQ} = 0$ and $\delta_w^* \simeq 0.981$ for $\hat{T}_{iQ} = 1$. The effect of $\hat{T}_{iQ}$ on other magnitudes is small but not negligible: the sheath potential drop at the CSL, $\hat{\phi}_{WQ}^*(\hat{T}_{iQ})$, decreases about a 17% when $\hat{T}_{iQ}$ goes from 0 to 1.

For $\delta_w > \delta_w^*$ the sheath is in the charge-saturated regime(CSR). A potential well is formed near the wall to turn back the excess of secondary flux. Its magnitude, $\Delta\phi_w$, must be such that the secondary flux satisfies the CSL condition $g_{rs} = -\delta_w^* g_{rp}$ at the point of minimum potential. A simple estimate yields

$$\Delta\phi_w \sim (T_w/e)\ln(\delta_w/\delta_w^*). \tag{2.23}$$

Then, in the asymptotic limit $T_w/T_p \to 0$, the potential well can be neglected and the dimensionless solution for the whole charge-saturated regime (CSR) coincides with that of the CSL. In particular, one has, for the CSR,

$$\frac{e\phi_{WQ}}{T_p} = \text{const} = \hat{\phi}_{WQ}^*(\hat{T}_{iQ}). \tag{2.24}$$

A final observation is that Eq.(2.22) implies that $g_{ri}/|g_{rs}| \simeq 8.3\sqrt{m_e/m_i}$, a result which agrees in order of magnitude with the well-known Langmuir condition, $g_{ri}/|g_{rs}| = \sqrt{m_e/m_i}$, for a classical strong double layer (characterized by $e\phi_{WQ}/T_p \gg 1$) [40].

2.4 COMPLETE SOLUTION

2.4.1 Presheath solution

The solution of the sheath is universal for any value of the plasma density and the electron temperature at the sheath entrance. In particular, the net plasma current to the wall, which is constant across the sheath, is determined by the presheath.

For total trapping of secondary emission, the quasineutral plasma of the presheath consists of (i) the population i of ions, which accelerate from point M of maximum potential and zero ion velocity towards the sheath transition points Q' and Q, and (ii) a single population e of confined electrons, which are in Maxwell-Boltzmann equilibrium at temperature T_e. Since population e differs from population p of the sheath, their temperatures (which express the average random energy of the two populations) are different, in general, and the relation between them is part of the complete solution.

According to Ch. 1, for the general case of a plasma flowing axially between two annular walls, the presheath problem depends on the channel geometry (annular ratio $\beta = r_{W'}/r_W$, and channel width h_c), the plasma conditions (ion density and temperature at point M, n_{iM} and T_{iM}, and electron temperature T_e), and effective frequencies for net plasma production (ν_w), ionization (ν_i), and radial friction (ν_r). The presheath problem states that the transition to the (outer) sheath is defined by the sonic Bohm condition [40, 3]

$$m_i v_{riQ}^2 = \frac{5}{3} T_{iQ} + T_e. \tag{2.25}$$

The dimensionless presheath solution depends on just four dimensionless parameters: β, $\tilde{T}_{iM} \equiv T_{iM}/T_e$, $\tilde{\nu}_i \equiv \nu_i/\nu_0$, and $\tilde{\nu}_r \equiv \nu_r/\nu_0$, with $\nu_0 = h_c^{-1}\sqrt{T_e/m_i}$. The relationship

$$\tilde{\nu}_w = \tilde{\nu}_w(\beta, \tilde{T}_{iM}, \tilde{\nu}_i, \tilde{\nu}_r) \tag{2.26}$$

is known as the plasma balance equation; for the no-flowing case of Tonks-Langmuir, one has $\nu_w = \nu_i = \nu_r$ and the plasma balance equation becomes $\tilde{\nu}_i(\beta, \tilde{T}_{iM})$. Figure 2.5, commented below, illustrates the presheath solution with a particular example.

2.4.2 Presheath/sheath matching

The correct matching of the presheath and sheath solutions comes out from three basic conservation equations, which, indeed, have been imposed already: first, there is the particle conservation,

$$n_{pQ} + n_{sQ} = n_{eQ} = n_{iQ};$$

then, there is the continuity of the electron flux,

$$g_{rpQ} + g_{rsQ} = g_{reQ} = g_{riQ},$$

Fig. 2.1(b); and, third, there is the continuity and compatibility of the ion flux, which requires to satisfy the sonic Bohm conditions at the sheath and presheath sides, Eqs. (2.19) and (2.25).

Of course, for no secondary emission, populations p and e coincide and Eqs. (2.19) and (2.25) are the same condition. The demonstration that this sonic condition yields the only valid transition is well established [54, 48, 3]. For $\delta_w > 0$, to consider that Eqs. (2.19) and (2.25) are the same condition is (partially, at least) a postulate based in fundamental properties of the ion flow for the well-known zero-emission case. [A complete demonstration of the postulate would require to specify the transformation of populations p and s into population e in a transition layer centered at point Q.] Adding support to it, this postulate or condition closes the presheath/sheath matching since it provides the relationship we needed between T_p and T_e: equating Eqs. (2.19) and (2.25) one has

$$\frac{T_p}{T_e} = \frac{1 - \dfrac{T_p n_{sQ}}{2e\phi_{WQ} n_{pQ}}}{1 + \dfrac{n_{sQ}}{n_{pQ}}} < 1. \tag{2.27}$$

This way to relate the two temperatures is very adequate to our macroscopic model, more than a method based on the electron distribution functions at the two sides of point Q. Figure 2.4 shows the evolution of the temperature ratio T_p/T_e with δ_w, which is very similar to that of

n_{pQ}/n_{iQ} in Fig. 2.3(c). The fact that both are close to one even at the CSR, leads us to conclude that the details of the modeling of the electron populations is not very critical for the overall model.

In a recent two-dimensional model of the plasma discharge in a Hall thruster, Keidar *et al.*use a radial presheath/sheath model with secondary emission [37]. Their formulation is similar to ours for cold-ions ($T_i = 0$) but the presheath/sheath matching is solved unsatisfactorily. First, they do not explain how they relate the trapped populations in sheath and presheaths and just take $T_p = T_e$, even at the CSR. Second and more important, they impose a subsonic ion flow at the sheath entrance, violating the supersonic/sonic condition (2.18). The authors do not show radial profiles to support their hypotheses.

2.4.3 Results

Figure 2.5 shows an example of a matched sheath/presheath solution for an annular channel. Profiles are shown in the presheath scale, where the sheaths are two wall discontinuities; on the contrary, the sheaths are semi-infinite in the inner scale ($\zeta_Q = -\infty$ in Fig. 2.2). Wall conditions in Fig. 2.5 are such that the two sheaths are in the CSR. The profiles of the inner and outer presheaths are asymmetrical: larger potential drops and lower currents are found in the outer presheath. The presheath asymmetry introduces a very small asymmetry between the two sheaths (less than 1%). An interesting observation is that the potential drop in the presheath is not negligible at all; indeed, in Fig. 2.5, the potential drop in the outer presheath is larger than in the sheaths, $\phi_{QM} > \phi_{WQ}$. The profile of the ion temperature illustrates the competition between the heating effect due to ionization and the cooling effect due to rarefaction, this last one dominating totally in the sheaths and justifying the small effect of the ion temperature on the sheath solution.

The sheath solution showed that the relative potential drop $e\phi_{WQ}/T_p$ decreases as δ_w increases, and remains constant in the CSR. Figure 2.6(a) shows, for different wall materials, the evolution of the sheath potential drop with the electron temperature in the bulk of the channel, T_e. There is a relative maximum of $\phi_{WQ}(T_e)$, followed by a minimum just at the CSL, and then a linear increase with T_e: one has $e\phi^*_{WQ}/T_e \simeq 0.88$ (for xenon and $\hat{T}_{iQ} = 0$). An important point is that ϕ_{WQ} is independent of the wall material once in the CSR. The potential drops in the presheaths, ϕ_{QM} and $\phi_{Q'M}$, must be computed from the presheath solution of Ch. 1.

At a given radial cross-section, the energy fluxes of ion and electron into the (outer) wall are

$$\begin{aligned} \dot{Q}_{iW} &= g_{riQ}\big(\tfrac{1}{2}m_i(v_{riW}^2 + v_{xi}^2) + \tfrac{5}{2}T_{iW}\big) = g_{riQ}\big(e\phi_{WQ} + \tfrac{1}{2}T_e + \tfrac{10}{3}T_{iQ} + \tfrac{1}{2}m_i v_{xi}^2\big), \\ \dot{Q}_{eW} &= g_{rpQ} 2T_p = g_{riQ}\frac{2T_p}{1-\delta_w}, \end{aligned} \tag{2.28}$$

where v_{xi} is the (average) velocity of the ion axial flow in that radial section. The first observed feature is that electron losses depend strongly on the secondary-emission. Indeed, if there is no axial flow, ion energy losses are about 3 times larger than electron energy losses for $\delta_w = 0$, whereas they become equal for $\delta_w \sim 60 - 70\%$, and electron energy losses become two orders of magnitude larger than ion ones in the CSR. Warm and axial flow effects increase ion energy losses: in the acceleration region of a SPT-100 Hall thruster and for charge-saturated conditions, this increase can be up to one order of magnitude. Figures 6(b)-6(c) show the evolution of electron and ion energy losses with E_w and T_e. Notice the large gradients of $\dot{Q}_{eW}$ with T_e below the SCL. Again, the influence of the wall material disappears at the CSR, when $\dot{Q}_{eW}$ scales as $T_e^{3/2}$.

2.5 DISCUSSION

The presheath/sheath model with total trapping of secondary emission presented here is based in considering wall-emitted electrons as a free population within the thin, collisionless sheaths, and as part of a unique population of confined electrons within the presheath. As a consequence the populations of confined electrons in sheath and presheath are somewhat different. The presheath and the sheaths are solved separately and then matched using continuity equations for the plasmas density and fluxes. The sheath model is an extension of the Hobbs-Wesson model to warm ions, and presents a charge-saturated regime. The presheath model is the one developed recently by us for plasmas flowing axially, and of application to planar, cylindrical, and annular geometries. The imposition of sonic Bohm conditions at the two sides of the transition point closes the problem and relates the temperature of the confined electron populations in sheaths and presheath. It is found that, even at charge saturation, the density of secondary electrons entering into the presheath is small and the temperatures of the confined electron populations in sheaths and presheath are similar.

The complete sheath/presheath solution depends on five dimensionless parameters: β, $\tilde{\nu}_i$, $\tilde{\nu}_r$, $\tilde{T}_{iM}$, and E_w/T_e. The first four determine the presheath solution whereas the sheath solution depends mainly on the fifth one. At the charge-saturated regime the solution becomes independent of the wall material. A relevant feature is that particle losses to the walls are determined totally by the presheath, whereas the sheath solution gives only the energy losses per particle. Electron energy losses change drastically with secondary emission. Ion energy losses depend weakly on δ_w, have a contribution from the plasma axial flow, and dominate for low secondary emission.

The sheath does not vanish at the charge-saturated regime. The sheath potential drop presents a maximum for an intermediate value of δ_w and a relative minimum at the charge-saturated limit; then, it becomes proportional to the electron temperature. A non-zero ion temperature does not modify the emission yield necessary for charge saturation but diminishes the relative sheath potential at the charge-saturation regime. The potential drops in the inner and outer presheaths are negligible never. Furthermore, they can be larger than the sheath drops for large secondary emissions and large radial frictions. For annular channels, the inner and outer presheaths are asymmetric, but the two sheaths are practically identical (for the same wall material).

The model developed here is for total trapping of the secondary emission, which corresponds to the collisional regime, $\lambda_d \ll \lambda_{col} \ll h_c$. For the collisionless regime, $\lambda_{col} \gg h_c$, which is more typical of Hall thruster discharges, secondary electrons could cross the whole presheath from the emission wall and be collected at the opposite wall if they had enough radial energy to reach it. For instance, for the potential profile of Fig. 2.5(a), $\lambda_{col} \gg h_c$, and cold walls, electrons emitted from the outer wall will be collected back at the inner wall, whereas electrons emitted from the inner wall will be reflected back at the outer wall and will become either trapped in the plasma or collected back by the inner wall too. However, the presence of free populations of secondary electrons modifies in turn the radial of the electric potential in sheaths and presheath. Therefore,the present model is not applicable to partial trapping of secondary emission and a more general must be developed.

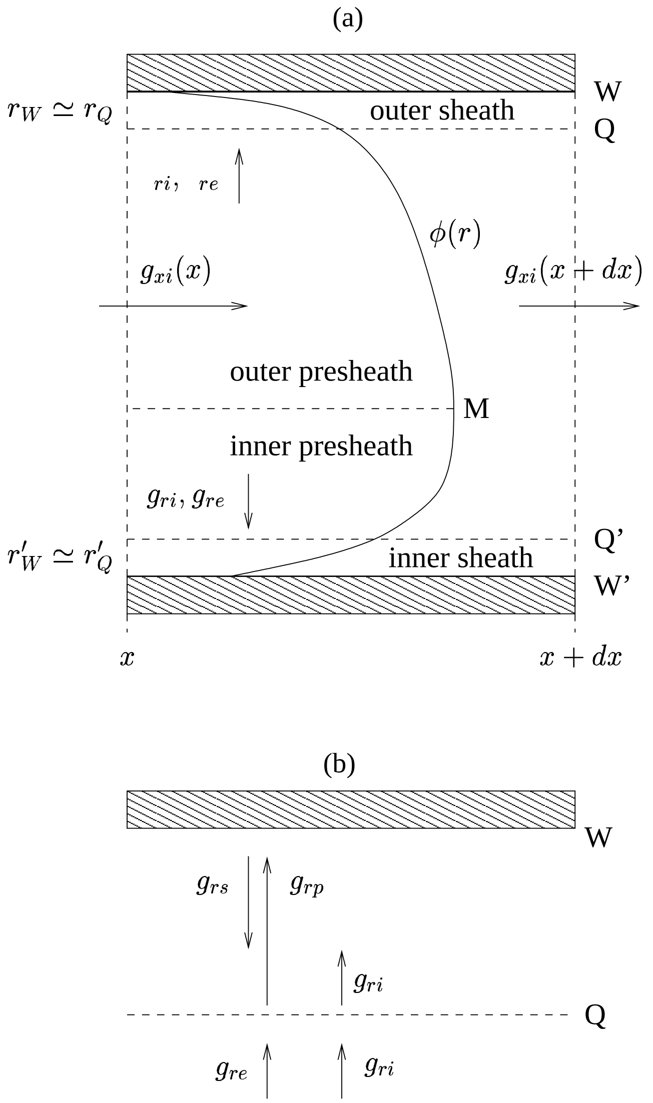
(a)
W
$r_W \simeq r_Q$
outer sheath
Q
ri, re
$\phi(r)$
$g_{xi}(x)$
$g_{xi}(x + dx)$
outer presheath
M
inner presheath
g_{ri}, g_{re}
Q'
$r'_W \simeq r'_Q$
inner sheath
W'
x
$x + dx$
(b)
W
g_{rs}
g_{rp}
g_{ri}
Q
g_{re}
g_{ri}

Figure 2.1: (a) A generic radial section of a long annular channel between two dielectric walls; g_x and g_r represent axial and radial particle fluxes, respectively; $\phi(r)$ sketches the electric potential, which is maximum at at intermediate point M; points Q and Q$'$ represent the transitions to the two sheaths, which actually are discontinuities in the quasineutral scale. (b) Treatment of the electron populations in radial presheath and sheath: in each sheath, primary(p) and secondary(s) electron populations are defined; in the presheath, a single population(e) is defined; zero-current condition plus conservation conditions at the presheath/sheath transition mean $g_{ri} = g_{re} = g_{rp} + g_{rs}$ there.

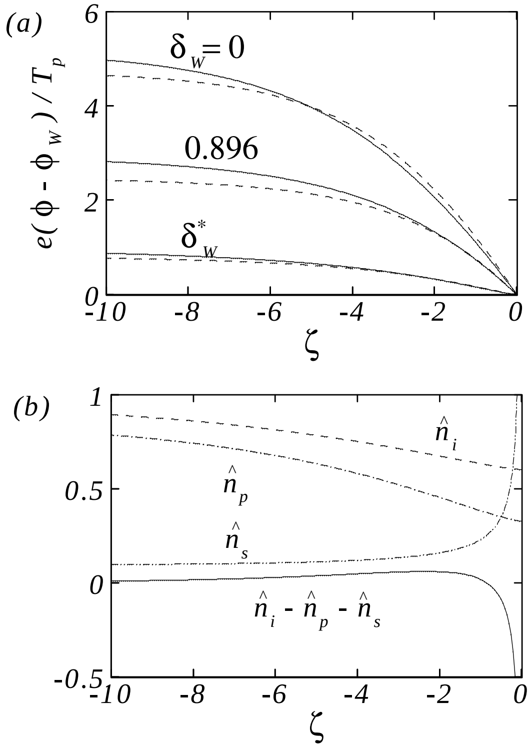

Figure 2.2: (a) Potential profile for different values of the secondary emission yield and $\hat{T}_{iQ}$ =0 (solid lines) and 1 (dashed lines). The cases $\delta_w = \delta^*_w(\hat{T}_{iQ})$ correspond to $d\hat{\phi}/d\zeta|_W = 0$, marking the charge-saturation limit of the sheath. (b) Profiles of the different plasma species for $\hat{T}_{iQ}$ =0 and $\delta_w = \delta^*_w$; $\hat{n}_i - \hat{n}_p - \hat{n}_s$ is the net electric charge in the sheath.

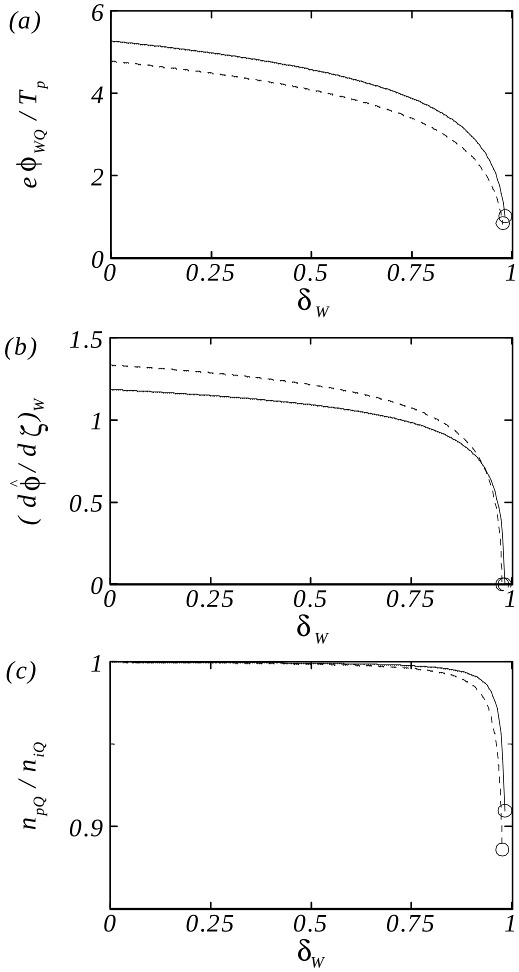

Figure 2.3: Evolution with δ_w of the sheath potential drop, the electric field at the wall, and the density of secondary electrons at point Q for $\hat{T}_{iQ}$ =0 (solid lines) and 1 (dashed lines). Circles correspond to the charge saturation limit. At the SCL $\hat{\phi}^*_{WQ}$ goes from 1.02 at $\hat{T}_{iQ} = 0$ to 0.846 at $\hat{T}_{iQ} = 1$.

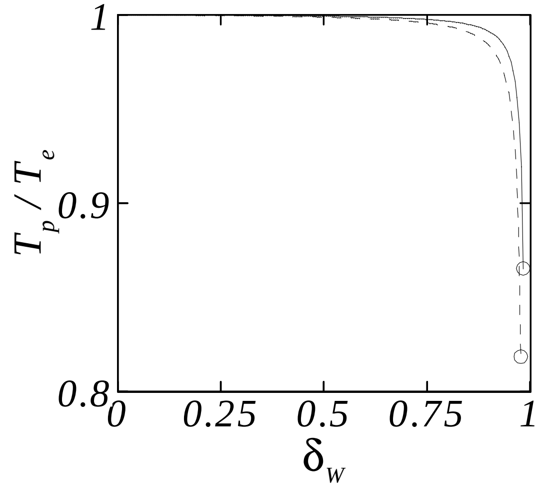

Figure 2.4: Evolution with δ_w of the temperature ratio for the confined electron populations p of sheath and e of presheath for $\hat{T}_{iQ}$ =0 (solid lines) and 1 (dashed lines). At the SCL $(T_p/T_e)^*$ goes from 0.865 at $\hat{T}_{iQ} = 0$ to 0.819 at $\hat{T}_{iQ} = 1$.

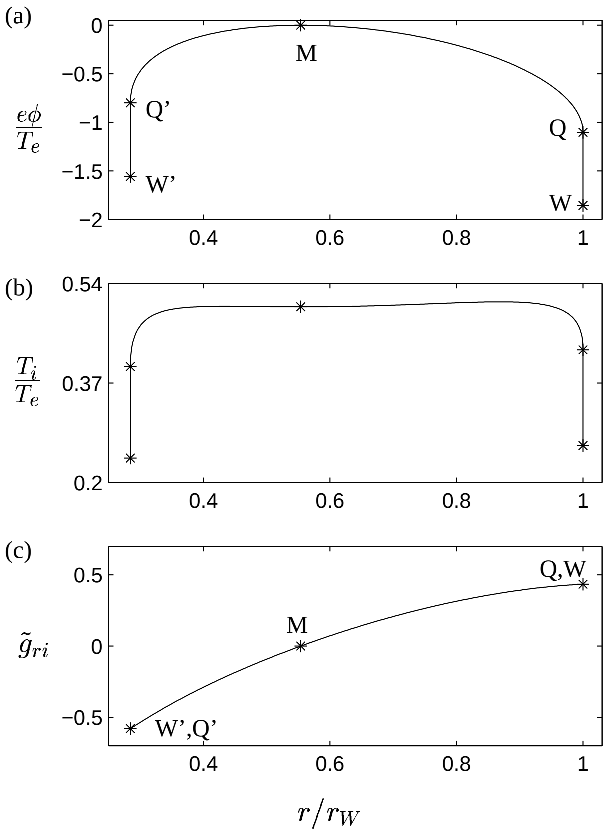

Figure 2.5: Complete presheath/sheaths solutions for an annular channel with $\beta = 0.285$, $T_{iM}/T_e = 0.50$, $\tilde{\nu}_r = \tilde{\nu}_i = 3.49$, and charge-saturated conditions at the two sheaths, $Q'W'$ and QW. The representation is in the quasineutral scale. In (c) $\tilde{g}_{ri} = (n_{iM}\sqrt{T_e/m_i})^{-1} g_{ri}$ is the dimensionless flux, which is constant across each sheath.

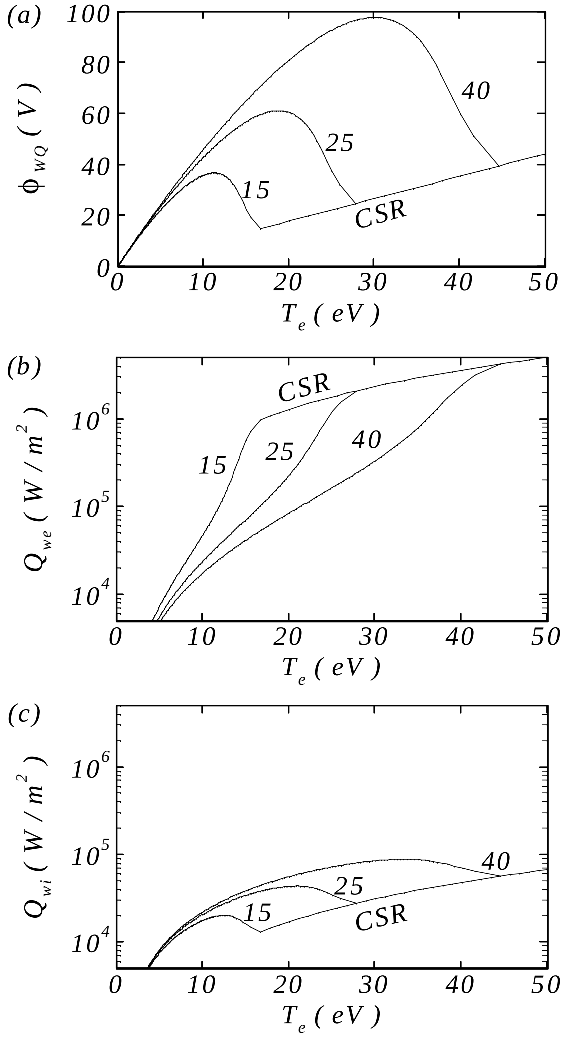

Figure 2.6: (a) Sheath potential drop, (b) electron energy losses, and (c) ion energy losses as function of T_e for xenon, $T_{iQ}/T_e = 0$, and three wall materials: E_w = 15, 25 and 40 eV. The curves are independent of E_w at the CSR. Plots (b) and (c) are for $n_{iQ} = 10^{18}\mathrm{m}^{-3}$; for other densities, particle and energy losses scale proportional to n_{iQ}.

Chapter 3

PARTIAL TRAPPING OF SECONDARY ELECTRON EMISSION

3.1 INTRODUCTION

Chapter 2 presented a macroscopic model of the interaction of a plasma with two parallel, electron-emitting, dielectric walls. The model is of application to quiescent and flowing plasmas, and planar, annular, and cylindrical geometries. The zero Debye-length limit was applied to develop a sheath/presheath/sheath model in the radial direction (i.e. perpendicular to the walls), with the maximum of the electrostatic potential around the center of the channel cavity. From each wall, secondary electron emission(SEE) is accelerated by the adjacent sheath into the bulk of the plasma. The central issue of that chapter was the treatment of the SEE once in the presheath. The analysis of the chapter was restricted to the collisional (or total-thermalization or total-trapping) case, when the two SEE beams collide with the main plasma, their radial momentum is dispersed in all directions, they cannot reach the opposite wall, and they thermalize eventually with the main population of confined electrons. The model took advantage of the two-scale analysis to treat SEE as independent beams within the emission sheaths, but as parts of a single electron population within the presheath. The warm-ion extension of the three-species model of Hobbs and Wesson [34] was used in the sheaths, and a two-species model of the presheath for flowing plasmas in annular geometries developed recently too was used in the presheath [3]. Appropriate conditions at the presheath/sheath transitions had to be defined to match consistently the different plasma models in sheaths and presheath.

This chapter addresses the extension of the model of Ch. 2 to partially-collisional and collisionless cases. This study is of direct application to Hall thrusters discharges [36]. For instance for a conventional, 1.5kW thruster (like a SPT-100) the channel width is about 15 mm, whereas the effective mean-free path for the SEE is estimated to range between 20 and 200mm, depending on the chamber zone [49].

There are several conclusions of the previous chapter which are worth to remind now. First, the losses of plasma current to the walls are determined totally by the presheath solution, whereas the energy lost by impacting electron/ion depends on the SEE properties of the walls. Second, for total-trapping the sheaths become charge saturated for a SEE yield near 100%. Third, the presheath structure depends on several parameters and can present larger potential drops than the sheaths. Four, for annular chambers, the presheath solution is asymmetric, and the two sheaths are different, in general.

The extension to the partial-trapping case we present here is however restricted to planar chambers when the solution is symmetrical with respect to the chamber mid-plane. The reason is that for annular chambers, the number of variables and types of solutions increases, the effects of partial-thermalization become mixed with those due to asymmetries, making difficult a complete and clear discussion of the problem.

3.2 MODEL FORMULATION

A sketch of the model is shown in Fig. 3.1. The hypotheses configuring it are the following:

(1) Zero net-current is considered at the lateral walls. This implies, in general, a radial potential profile with a single maximum at a point M, placed at the center of the channel (for planar geometry). Small potential wells near the wall at charge-saturation and other possible profiles which could arise for large SEE will be commented later.

(ii) We consider a planar chamber with the the two walls made of the same material. Then, symmetry considerations are of application to the plasma populations and the electric potential.

(iii) The zero-Debye-length asymptotic limit

$$\lambda_d/h_c, \lambda_d/\lambda_{col} \to 0 \tag{3.1}$$

holds, where λ_d is the plasma typical Debye length h_c the channel width, and λ_{col} the effective mean-free-path for SEE. This allows us to carry out a two-scale sheath/presheath/sheath analysis.

(iv) The plasma is constituted by: ions(i) being attracted by the low wall potential; confined, primary electrons(p); and two SEE populations(s), one from each wall. SEE from one wall is accelerated away from it by the electrostatic potential of the adjacent sheath. Assuming the wall temperature, T_w, much smaller than the sheath potential (which is typically of the order of the electron temperature T_p) the SEE enters the presheath as a monoenergetic beam.

(v) The evolution of the SEE beams in the presheath depends on the collision probability,

$$\delta_c = \exp(-\lambda_{col}/h_c). \tag{3.2}$$

The collisional (total-trapping) case studied in Ch. 2 corresponds to $\delta_c \simeq 1$. In the collisionless (or zero-trapping) limit, $\delta_c \simeq 0$, the SEE beam emitted from one wall is expected to cross freely the presheath and to be collected at the opposite wall, unless the potential difference between the two walls turn the beam back; in this last case, it will be collected back by the emission wall. Finally, for the partially-collisional case, it is expected that one fraction of each SEE beam be trapped and thermalized within the main plasma, and the other part be collected back at the wall with the largest potential.

(vi) The collision probability δ_c is used to split each SEE beam in two parts: one, proportional to δ_c, which becomes trapped and thermalized with the main electron population, and another, proportional to $1 - \delta_c$, which crosses freely the presheath, arrives to the second wall with exactly the (small) radial momentum it had at the emission wall, and is collected by it. As in Ch. 2, in the presheath, the trapped SEE is included into the confined electron population. The free SEE is modeled in the same way in presheath and sheath and, due to its small impact energy, does not produce extra SEE when it is collected back.

(vii) The ion population is considered cold: $T_i/T_e \to 0$. This is just a minor simplification and not a real restriction, since warm-ion effects are qualitatively the same independently of the level of SEE trapping. By eliminating the energy equation for ions we focus the discussion on the main issue of the chapter: the plasma response with SEE partial-trapping.

3.3 SHEATH ANALYSIS

Figure 3.1(b) sketches the different plasma populations in one sheath: primary electrons(p) diffusing from the presheath, secondary electrons(s) emitted by the wall, and the free secondary electrons(f) remaining from the beam emitted by the opposite wall. The symmetry of the problem means that the conditions of populations f and s are the same except for the direction of their radial velocity.

The plasma conservation equations for the collisionless sheath are,

$$n_\alpha v_{r\alpha} \equiv g_{r\alpha} = \text{const}, \quad (\alpha = i, p, s, f), \tag{3.3}$$

$$n_p = n_{pW} \exp \frac{e(\phi - \phi_W)}{T_p}, \tag{3.4}$$

$$v_{ri} = \sqrt{v_{riQ}^2 + \frac{2e}{m_i}(\phi_Q - \phi)}, \tag{3.5}$$

$$v_{rf} = -v_{rs} = \sqrt{v_{rsW}^2 + \frac{2e}{m_e}(\phi - \phi_W)}, \tag{3.6}$$

In the last equation we will take $m_e v_{sW}^2/T_e \sim T_w/T_e \simeq 0$.

The ion flux into the sheath g_{riQ} is determined mainly by the presheath. Assuming population p to be Maxwellian-like at temperature T_p, the flux of primary electrons at the wall is given by

$$g_{rpQ} = n_{pW}\sqrt{T_p/2\pi m_e}, \tag{3.7}$$

The equations relating the different fluxes are

$$g_{riQ} = g_{rpQ} + g_{rsW} + g_{rfQ}, \tag{3.8}$$

$$g_{rsW} = -\delta_w g_{rpQ}, \tag{3.9}$$

$$g_{rfQ} = (1 - \delta_c)(-g_{rsW}), \tag{3.10}$$

with $\delta_w(T_p)$ the SEE yield, which depends on the wall material. Notice that Eqs. (3.6) and (3.10) yield

$$n_f = (1 - \delta_c) n_s. \tag{3.11}$$

For $\zeta = (r - r_W)/\lambda_d$, with $\lambda_d = \sqrt{\epsilon_0 T_p / e^2 n_{iQ}}$, the natural spatial variable in the sheath,

$$U(e\phi) = n_p T_p + (n_s + n_f) m_e v_{rs}^2 + n_i m_i v_{ri}^2 \tag{3.12}$$

the Sagdeev's potential, and applying the boundary condition

$$\left.\frac{d(e\phi/T_p)}{d\zeta}\right|_Q = 0, \tag{3.13}$$

the integration of the quasiplanar Poisson equation yields

$$\frac{e^2 n_{iQ}}{2T_p}\left(\frac{d\phi}{d\zeta}\right)^2 = U(e\phi) - U(e\phi_Q). \tag{3.14}$$

Two other boundary conditions at point Q are needed to close the sheath problem. These are plasma quasineutrality,

$$0 = U'_Q \equiv n_{pQ} + n_{sQ} + n_{fQ} - n_{iQ}, \tag{3.15}$$

and the Bohm condition

$$0 = U''_Q \equiv \left(\frac{n_p}{T_p} - \frac{n_s + n_f}{m_e v_{rs}^2} - \frac{n_i}{m_i v_{ri}^2}\right)\Big|_Q. \tag{3.16}$$

Solving this last one for the ion velocity, one has

$$m_i v_{riQ}^2 = \frac{2e\phi_{WQ} T_p n_{iQ}}{2e\phi_{WQ} n_{pQ} - T_p(n_{sQ} + n_{fQ})}. \tag{3.17}$$

It will be shown that the last term in the denominator of Eq. (3.17) is small always, leading to $v_{riQ} \simeq \sqrt{T_p/m_i}$.

One magnitude of interest is the heat deposited at the walls by the currents of ions and primary electrons. This energy flux (per unit of channel length) satisfies

$$q_{rW} = 2T_p g_{rpQ} + \frac{1}{2} m_i v_{riW}^2 g_{riQ} = \left(\frac{2T_p}{1 - \delta_c \delta_w} + \frac{1}{2} m_i v_{riQ}^2 + e\phi_{WQ}\right) g_{riQ}, \tag{3.18}$$

(for zero axial flow of the plasma).

3.3.1 Dimensionless solution

Parameters T_p and n_{iQ} are used to non-dimensionalize the sheath equations; hats will be used to call non-dimensional variables (i.e. $\hat{\phi} = e\phi/T_p$). Then, the dimensionless sheath solution depends on just two parameters, δ_w and δ_c. Figures 3.2(a) and3.2(b) show the sheath potential profile for different values of δ_c and δ_w. For δ_w given [Fig. 3.2(a)], the net SEE flux,

$$g_{rfQ} + g_{rsW} = \delta_c \delta_w g_{rpW}, \tag{3.19}$$

decreases with the collision parameter, δ_c. Then, in order to satisfy the zero-current condition, which can be expressed as

$$g_{riQ} = (1 - \delta_c \delta_w) n_{pQ} \exp \frac{-e\phi_{WQ}}{T_p} \sqrt{\frac{T_p}{2\pi m_e}}, \tag{3.20}$$

a larger ϕ_{QW}, is required. A similar reasoning explains the evolution of the profiles with δ_w in Fig. 3.2(b); this figure can be compared with a similar one for $\delta_c = 1$ in Ch. 2.

Solving for $\hat{\phi}_{WQ}$, Eq. (3.20) yields

$$\hat{\phi}_{WQ} \equiv \frac{e\phi_{WQ}}{T_p} = \ln \sqrt{\frac{m_i}{2\pi m_e}} + \ln(1 - \delta_c \delta_w) + \ln\left(\frac{n_{pQ}}{n_{iQ}} \sqrt{\frac{T_p}{m_i v_{riQ}^2}}\right). \tag{3.21}$$

Then, as long as $1-\delta_c\delta_w < O(\sqrt{m_e/m_i})$, one has $\hat{\phi}_{WQ} \simeq \ln\sqrt{m_i/2\pi m_e}$. A very interesting fact is that $\hat{\phi}_{WQ}$ depends on δ_c and δ_w mainly through the product $\delta_c\delta_w$. Physically, it means that $\hat{\phi}_{WQ}$ is fixed by the ratio $g_{rpQ}/g_{riQ} = 1-\delta_c\delta_w$. Since, in addition, the typical Debye length of the sheath does not depend practically on the SEE, cases with the same value of $\delta_c\delta_w$ are going to have very similar sheath profiles. Figures 3.3(a) and 3.3(b), show density profiles for two very dissimilar cases, and confirm that conclusion; in Fig. 3.3(b), notice that the SEE density modifies only a local region near the wall and has no global impact on the sheath solution.

3.3.2 Charge-saturation

When the product $\delta_c\delta_w$ becomes close to one, $\hat{\phi}_{WQ}$ decreases and the sheath approaches the charge-saturation limit (CSL). This is characterized by the condition $d\phi/d\zeta|_W = 0$ or, using Eq. (3.14), by

$$0 = U(e\phi_W) - U(e\phi_Q). \tag{3.22}$$

This condition yields the relation, $\delta_w = \delta_w^*(\delta_c)$, the two sheath parameters satisfy at the CSL. Figure 3.4 shows that δ_w^* increases as δ_c decreases, and attains very large values for $\delta_c \ll 1$; one has $1-\delta_w^* \simeq 8.31\sqrt{m_e/m_i}$ for $\delta_c = 1$, and $\delta_w^* \simeq 0.24\sqrt{m_i/m_e}$ for $\delta_c = 0$. For real materials, the maximum SEE yield, δ_{wm}, is between 1 to 2 for many metals, and of the order of 10 for some dielectrics [55, 43]. This leads to the important conclusion that the sheath does not reach charge-saturated conditions in low-collisional plasmas, more precisely, for $\delta_c < 1/\delta_{wm}$.

For wall and plasma conditions leading to $\delta_w > \delta_w^*(\delta_c)$ the sheath is in the charge-saturated regime(CSR): a potential well is formed near the wall to reduce the actual flux ratio of population s reaching the bulk of the plasma to δ_w^*. For $T_w/T_p \to 0$, the potential well is negligible and the dimensionless sheath solution for the CSR is the same that for the CSL.

The CSL relation $\delta_w = \delta_w^*(\delta_c)$ is explained from the pressure balance implicit in Eq. (3.22). Extending the analysis of Ch. 2 to $\delta_c < 1$, the dominant terms in Eq. (3.22) at the CSL yield

$$\sqrt{\frac{m_i}{m_e}} \sim \frac{|g_s| + g_f}{g_i} \equiv \frac{\delta_w^*(2-\delta_c)}{1-\delta_c\delta_w^*}. \tag{3.23}$$

Indeed the approximation

$$\sqrt{\frac{m_i}{m_e}}\frac{1-\delta_c\delta_w^*}{\delta_w^*(2-\delta_c)} = 2.35 + 5.64\delta_c \tag{3.24}$$

fits very well the exact solution for $\delta_w^*(\delta_c)$; both are indistinguishable in Fig. 3.4. Finally, Eq. (3.23) yields

$$\begin{aligned} |g_s| &\sim g_p \gg g_i \quad \text{if} \quad \delta_c = O(1), \\ |g_s| &\gg g_p \simeq g_i \quad \text{if} \quad \delta_c \ll 1. \end{aligned} \tag{3.25}$$

indicating that, at the CSL, the electrical current balance among the different species depends on the SEE collisionality.

3.3.3 Results

Figures 3.5(a)-3.5(c) show the influence of δ_w and δ_c on some important sheath magnitudes; in Fig.3.5(c)

$$\hat{q}_{rw} \equiv \frac{q_{rw}}{T_p g_{riQ}} = \frac{2}{1-\delta_w\delta_c} + \hat{\phi}_{WQ} + \frac{1}{2-(1+2\hat{\phi}_{WQ}^{-1})(2-\delta_c)\hat{n}_{sQ}} \tag{3.26}$$

is the (dimensionless) energy flux deposited at the wall per ion impinging it and unit of channel length. The region of valid sheath solutions turns out to be bounded by four limit cases: (i) total-trapping, (ii) zero-trapping, (iii) maximum SEE yield, and (iv) sheath charge-saturation.

Figures 3.6(a)-3.6(c) are similar to the preceding ones but emphasize that the role of the plasma temperature T_p and a maximum SEE yield. For $\delta_w(T_p)$ we used the Lye-Dekker formula [referenced by Vaughan[55]]

$$\delta_w(T_p) = \delta_{wm} \frac{f(z_m T_p / T_{pm})}{f(z_m)}, \tag{3.27}$$

where T_{pm} is the electron temperature where δ_{wm} is reached, $f(z) = z^{-0.35}[1 - \exp(-z^{1.35})]$, $z_m \simeq 1.84$, and $f(z_m) \simeq 0.725$.

3.4 PLANAR PRESHEATH ANALYSIS

The presheath problem is formulated and solved as in Ch. 2, so that we can avoid to justify every point. The plasma in the presheath consists of ions(i), the two symmetrical populations(f) of free SEE, and a population e of confined electrons. Th as the transition (or Bohm) condition at the presheath side of point Q. Both Eqs. (3.17) and (3.33) are generalized forms of the sonic Bohm condition for multi-species plasmas. Physically, the sonic condition on a single fluid is related to the balance between convection and pressure. In this multi-species plasma, the quasineutral electrostatic interaction of the ions with several electron populations is felt like a pressure term by the ion fluid, the right sides of Eqs. (3.17) and (3.33) being the effective pressure (divided by n_{iQ}) on the ion fluid.

Imposing v_{riQ} to satisfy the right-hand sides of Eqs. (3.17) and (3.33), the relation between T_e and T_p we sought is obtained,

$$\frac{n_{eQ}}{T_e} = \frac{n_{pQ}}{T_p} - \frac{n_{fQ}}{2e\phi_{WQ}}, \tag{3.34}$$

The conservation of the electron flux and density at point Q,

$$n_{eQ} = n_{pQ} + \delta_c n_{sQ}, \quad g_{eQ} = g_{pQ} + \delta_c g_{sQ}, \tag{3.35}$$

completes the matching conditions for the electron populations in sheaths and presheath.

Since the sheath problem is solved already, it is convenient to integrate the presheath problem from point Q towards point M, with

$$\eta = \frac{(r_Q - r)\nu_w}{\sqrt{T_p/m_i}} \tag{3.36}$$

as independent variable, and using n_{iQ} and T_p to non-dimensionalize. In this way, apart from δ_w and δ_c, the presheath solution depends on one extra parameter, $\alpha_r = \nu_r/\nu_w$.

The integration ends at $v_{riM} = 0$ (or $\partial\phi/\partial r|_M = 0$) and defines the value of η at point M,

$$\eta_M = \eta_M(\delta_w, \delta_c, \alpha_r) \tag{3.37}$$

Since the channel width h_c is known, η_M determines, in fact, the production frequency,

$$\nu_w = \frac{2\eta_M\sqrt{T_p/m_i}}{h_c}. \tag{3.38}$$

Using the characteristic frequency $\nu_0 = h_c^{-1}\sqrt{T_e/m_i}$, and calling $\tilde{\nu}_\alpha = \nu_\alpha/\nu_0$, $(\alpha = w, r)$ the functional relation (3.37) becomes

$$\tilde{\nu}_w = \tilde{\nu}_w(\tilde{\nu}_r, \delta_w, \delta_c) \tag{3.39}$$

which is the *plasma balance equation*of this plasma, and shows that the net production frequency is not an independent parameter [54]. For total-thermalization ($\delta_c = 1$) $\tilde{\nu}_w$ did not depend on δ_w, just on $\tilde{\nu}_r$. For $\delta_c < 1$, both δ_w and δ_c affect $\tilde{\nu}_w$. However, since the density of the f-populations is small [according to Fig. 3.5(b), $2n_{fQ}/n_{iQ}$ is always less than 15%] the influence of the free SEE on the presheath solution is small. Figure 3.7 plots $\tilde{\nu}_w(\tilde{\nu}_r)$ for different values of (δ_w, δ_c), showing that the influence of these two parameters is rather irrelevant.

3.5 CONCLUSIONS

The model presented here assumes that if SEE is partially-collisional, it can be split in two groups, one trapped and eventually thermalized with the main plasma, the second one constituted by two free counterstreaming beams, which, for the planar case, are collected back at the wall opposite to the emission one.

The density of the two free SEE beams is low in most of the sheath and the whole presheath. Then, the presheath solution is practically identical to the total-trapping case. The ion flux into the walls is determined by presheath properties: plasma temperature, channel width, and one contribution from the axial behavior.

Net SEE flux increases with the product $\delta_c \delta_w$, and reduces the flux of primary electrons, g_{rpW}, needed to keep the zero-current condition. The sheath potential drop is self-adjusted to collect the required g_{rpW}. As a consequence, the sheath solution is almost invariant for $\delta_w \delta_c = \text{const}$. This explains that charge saturation requires a larger SEE yield as the SEE collisionality in the plasma decreases. Indeed, for low SEE collisionality, the maximum SEE yield of the wall material, δ_{wm}, will be below δ_w^*, and charge saturation cannot be reached.

Finally, the collisionless or zero-thermalization case does not pose any particular problem. For all practical cases, the sheath solution is the same than for the zero SEE case.

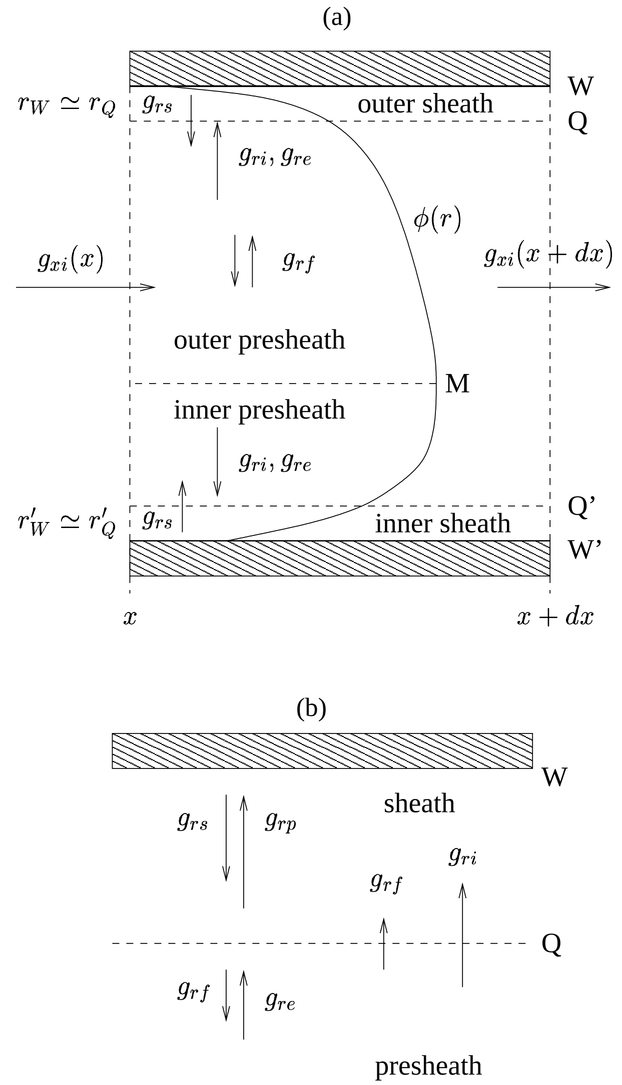
(a)
W
$r_W \simeq r_Q$
g_{rs}
outer sheath
Q
g_{ri}, g_{re}
$\phi(r)$
$g_{xi}(x)$
g_{rf}
$g_{xi}(x+dx)$
outer presheath
M
inner presheath
g_{ri}, g_{re}
Q'
$r'_W \simeq r'_Q$
g_{rs}
inner sheath
W'
x
$x+dx$
(b)
W
sheath
g_{rs}
g_{rp}
g_{ri}
g_{rf}
Q
g_{rf}
g_{re}
presheath

Figure 3.1: Sketch of the radial models in (a) presheath and (b) sheath.

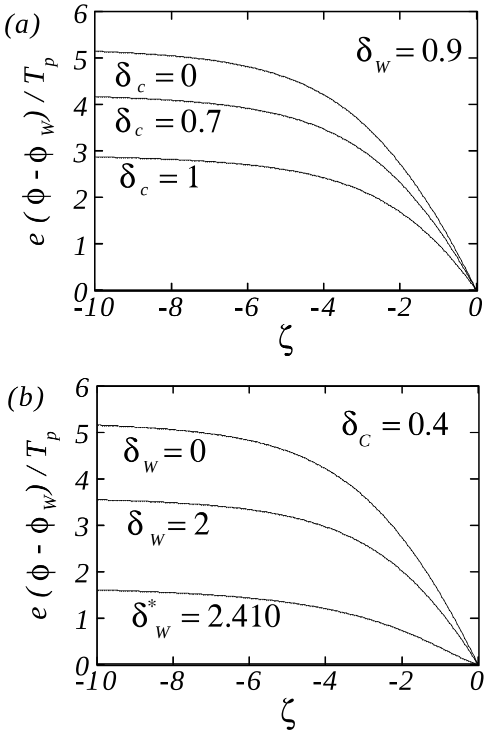

Figure 3.2: Sheath solution. Profiles of the electrostatic potential for: (a) $\delta_w = 0.9$ and several values of δ_c from 0 t[illegible]

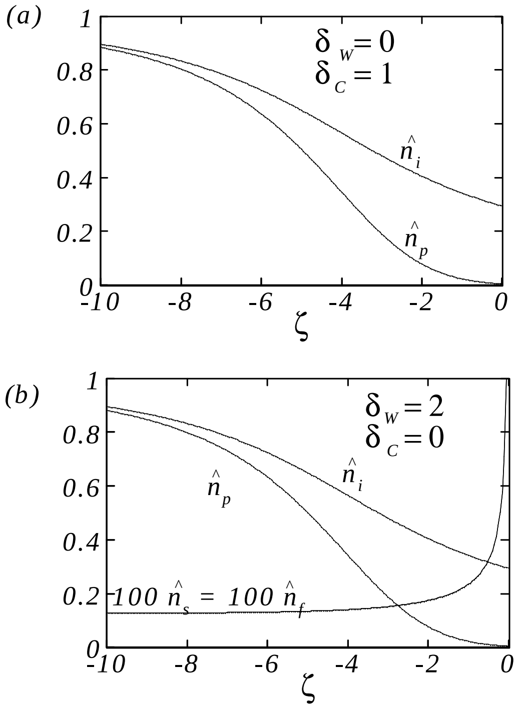

Figure 3.3: Sheath solution. Profiles of the different density species for: (a) $\delta_w = 0$ and $\delta_c = 1$; (b) $\delta_w = 2$ and $\delta_c = 0$.

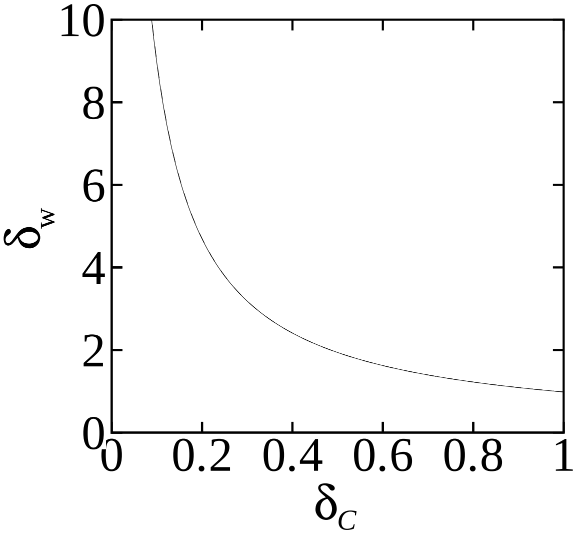

Figure 3.4: Sheath solution. The charge-saturation limit.

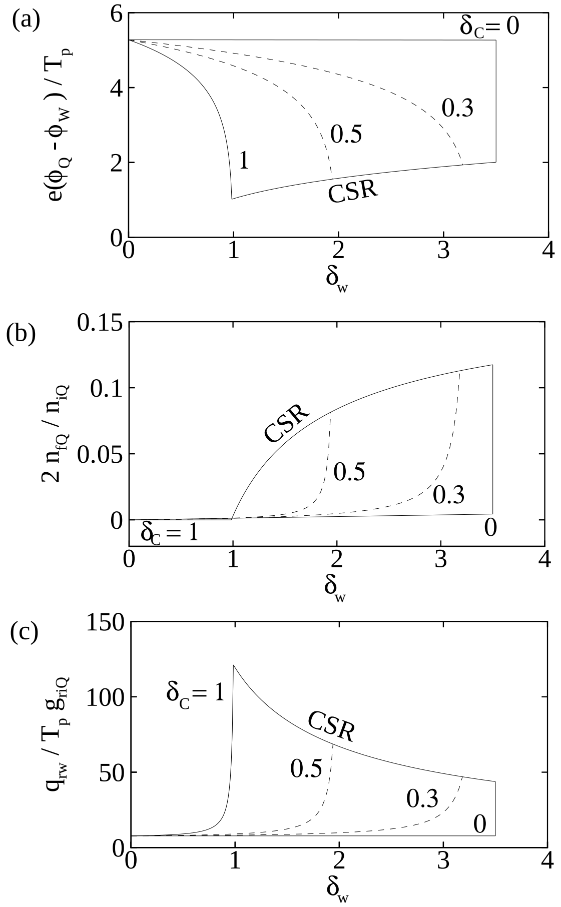

Figure 3.5: Sheath solution. (a) Potential drop, (b) relative free SEE density of at the sheath transition, and (c) radial energy losses in terms of δ_w and δ_c, up to the CSR.

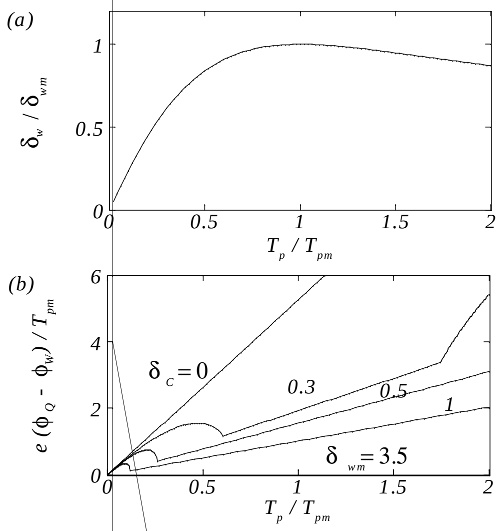
(a)
δ_w / δ_{wm}
0
0.5
1
0
0.5
1
1.5
2
T_p / T_{pm}
(b)
$e(\phi_Q - \phi_W) / T_{pm}$
0
2
4
6
$\delta_C = 0$
0.3
0.5
1
$\delta_{wm} = 3.5$
0
0.5
1
1.5
2
T_p / T_{pm}

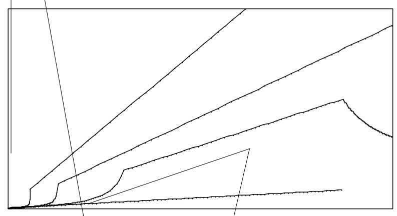

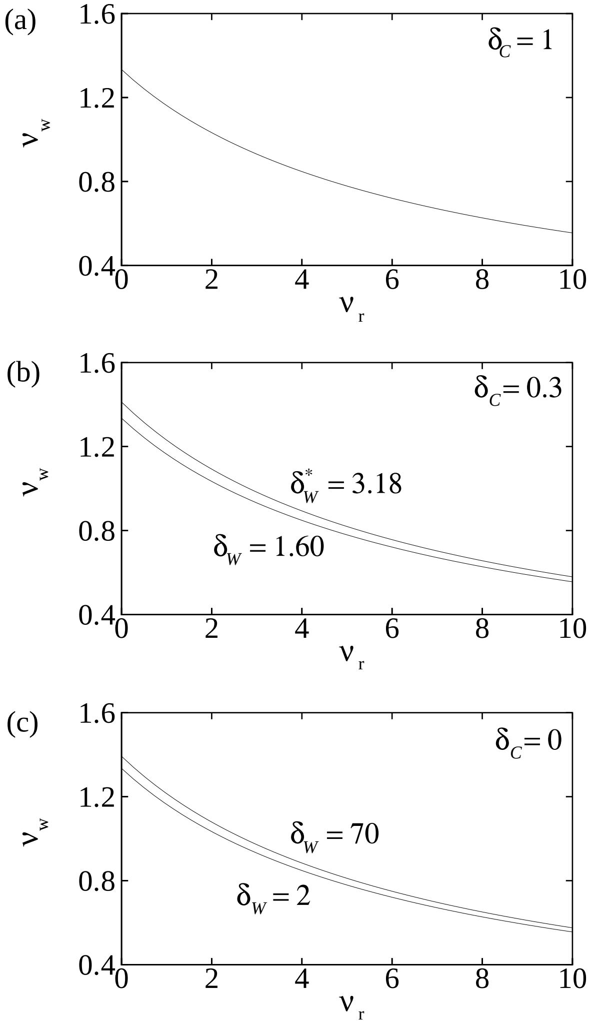

Figure 3.7: $\tilde{\nu}_w$ versus $\tilde{\nu}_r$ for different values of δ_c and δ_w.

Chapter 4

AXIAL MODEL WITH HEAT CONDUCTION

4.1 INTRODUCTION

Recently we presented a one-dimensional(1D) model (hereafter called Model I) of the stationary axial structure of the plasma discharge inside a Hall thruster and in the near-plume[10]. The structure consisted in an anode sheath, a region of free-diffusion for electrons and reverse flow for ions, the ionization zone, and the acceleration region, which extends into the plume, Fig. 4.1. Although quantitative accuracy could not be expected from Model I, it reproduced rather well most of the main features of the experimental data [15, 31, 38, 32]. Compared to previous 1D models[39, 28, 19], Model I unveiled the combined importance of the electron pressure and the reverse flow of ions in shaping the plasma structure. In addition, the inclusion of the near-plume (with the neutralization surface) allowed closure of the formulation with realistic boundary conditions, and parametric studies on thruster performance. Of particular interest was the determination of the parametric domain of stationary solutions, which was bounded by the case of zero ion reverse flow[6, 8].

The main defect of Model I came from the simplified treatment of the electron energy equation, which included neither heat conduction nor the losses coming from the interaction with the lateral walls of the chamber. The resulting temperature profile had too large gradients around the ionization region and a too large peak temperature. A hybrid (particle/fluid) numerical model by Fife, which includes heat conduction and wall losses, yields smoother temperature profiles[25]. In this chapter we present a 1D macroscopic model (hereafter called Model II) which adds heat conduction to Model I. The first point to be emphasized is that heat conduction is not a new forcing term added to the equations of Model I: it transforms the electron energy equation from first to second order for the electron temperature, a fact having major implications in the mathematical treatment and the parametric domain of stationary solutions. The effects of the plasma interaction with lateral walls are not included in Model II. Two are the reasons: first, a detailed radial model of that interaction, to be coupled to the axial model, is still under investigation[9]; and second, it is of interest to understand the plasma response in thrusters where lateral losses are small.

The chapter includes the detailed formulation of Model II, the discussion of the spatial response, and a parametric investigation on the thruster stationary performances. In addition, three issues, not treated in detail in Ref.[10], are analyzed here. The first one, treated more or less explicitly in the recent literature, is the evaluation of the diffusive approximation for the electron motion. Tahara *et al.* [53] and Barral *et al.* [13] have added different inertial terms into their 1D macroscopic models; Fedotov *et al.* [24] suggest the presence of unmagnetized and magnetized populations of electrons near the thruster exit; Haas and Gallimore[32] conclude, from their experiments, that the drift energy can be high enough to contribute to ionization. The second issue is the computation of the ion temperature, seeking a confirmation that it can be neglected everywhere compared to either the electron temperature or the ion beam velocity. And the third one is a detailed evaluation of the thrust: computations based in the momentum thrust of the plasma either at the channel exhaust (as we did in Ref.[10]), or in the far-plume (as simulation models usually do[25]) are not accurate enough.

The chapter is organized as follows. In Sec. II we formulate the quasineutral model, including a detailed discussion on the diffusive approximation for electrons. In Sec. III we discuss the model singular points, the anode sheath, the boundary conditions, and the numerical procedure. In Sec. IV we analyze the spatial solution, the different collision frequencies, the validity of the diffusive approximation, and the ion temperature. In Sec. V we discuss the thruster performance in the parametric domain of stationary solutions. Conclusions are written in Sec. VI.

4.2 THE QUASINEUTRAL MODEL

Geometrical sketches of the thruster and the axial model are drawn in Fig. 4.1(a)-4.1(b). The general hypotheses of the present Model II are the same as in Model I. In the 1D axial approximation, plasma variables represent average values on each cross-section and depend only on the axial variable x. The macroscopic formulation will consist of fluid-like equations for ions(i), electrons(e) and neutrals(n). The thruster channel is of length L and radial area A_c. The plasma discharge extends outside the thruster into a plasma plume of radial area $A(x)$ to be determined. The magnetic field is considered purely radial, $\boldsymbol{B} = B(x)\mathbf{1}_r$, with the maximum field placed near the thruster exit, and two different semi-Gaussian axial profiles will be used inside the thruster and in the near-plume. Electrons are injected into the plume at a neutralization surface (point P) placed at a distance L_{EP} from the channel exit (point E). The voltage difference between anode (point A) and point P is the discharge voltage, V_d, and the electron current delivered at the neutralization surface is the discharge current, I_d. One part of this current flows outwards and neutralizes the ion current I_{iP}; the other part, $I_d - I_{iP}$, diffuses inwards across the radial lines of the applied magnetic field and ionizes the mass flow of neutrals, $\dot{m}_A$, injected at the anode; subscript ∞ will refer to downstream conditions far away from the cathode P. No effects of the radial interaction of the plasma with the lateral walls of the chamber will be included in this model.

The axial plasma flow is considered quasineutral everywhere except in a thin, electron-repelling sheath attached to the anode (region AB in Fig. 4.1, with $x_B \simeq x_A = 0$ in the quasineutral scale). The potential jump in the sheath, $\phi_{AB} = \phi_B - \phi_A > 0$, adjusts the small diffusive electron flow in the channel to the thermal flow collected at the anode. Since all ions are created by ionization within the thruster, plasma quasineutrality implies back-flow of ions in the rear part of the channel.

4.2.1 Electron dynamics

We review here the closed-drift, diffusive-motion model in order to evaluate the importance of inertial effects in the electron dynamics. Also, the diffusive equation for heat conduction is formulated.

The vector equation for the electron momentum is

$$m_e n_e \boldsymbol{v}_e \cdot \nabla \boldsymbol{v}_e = -\nabla n_e T_e + e n_e \nabla \phi - e n_e \boldsymbol{v}_e \wedge \boldsymbol{B} - \boldsymbol{R}_e. \tag{4.1}$$

Apart from conventional symbols,

$$\boldsymbol{R}_e = m_e n_e (\nu_e \boldsymbol{v}_e - \nu_{ei} \boldsymbol{v}_i - \nu_{en} \boldsymbol{v}_n)$$

is the friction force due to collisions, with

$$\nu_e = \nu_{en} + \nu_{ei} + \nu_{ano}, \tag{4.2}$$

the total collision frequency for electrons. This includes contributions from electron-neutral collisions (ν_{en}), electron-ion collisions (ν_{ei}), and anomalous effective collisions representing Bohm-like diffusion [20], which is expressed as

$$\nu_{ano} = \alpha_B \omega_e,$$

with $\omega_e = eB/m_e$ the electron gyrofrequency and α_B an empirical parameter (with a 'classical' value of 1/16). When current losses to lateral walls are taken into account, ν_e has another contribution from near-wall-conductivity [21, 9].

In the 1-D axial approximation, the electron velocity field is $\boldsymbol{v}_e = v_{xe}\mathbf{1}_x + v_{\theta e}\mathbf{1}_\theta$, and spatial gradients reduce to the axial direction, $\nabla \equiv \mathbf{1}_x d/dx$. Then, applying the closed-drift hypothesis,

$$\omega_e \gg \nu_e, \tag{4.3}$$

and the ansatz $|v_{\theta e}/v_{xe}| \sim \omega_e/\nu_e$, Eq. (4.1) simplifies into

$$0 \simeq m_e n_e \omega_e v_{\theta e} - \frac{d}{dx} n_e T_e + e n_e \frac{d\phi}{dx}, \tag{4.4}$$

$$v_{xe} \frac{dv_{\theta e}}{dx} \simeq -\omega_e v_{xe} - \nu_e v_{\theta e}. \tag{4.5}$$

The first term in Eq. (4.5) is the inertia of the electron azimuthal motion and is the dominant convective contribution. Then, the diffusive approximation requires

$$\frac{1}{\omega_e}\left|\frac{dv_{\theta e}}{dx}\right| \ll 1, \tag{4.6}$$

and reduces Eq. (4.5) to

$$v_{\theta e}/v_{xe} \simeq -\omega_e/\nu_e. \tag{4.7}$$

The equation for the electron internal energy reads

$$\nabla \cdot \left(\frac{3}{2} n_e T_e \boldsymbol{v}_e + \boldsymbol{q}_e\right) = -n_e T_e \nabla \cdot \boldsymbol{v}_e - \boldsymbol{v}_e \cdot \boldsymbol{R}_e - \nu_i n_e \alpha_i E_i. \tag{4.8}$$

Here, $\boldsymbol{q}_e$ is the electron heat conduction,

$$\boldsymbol{v}_e \cdot \boldsymbol{R}_e \simeq m_e n_e \nu_e v_{\theta e}^2$$

is the Joule heating (we assumed $v_n \ll v_{xi} \sim v_{xe} \ll v_{\theta_e}$), and the last term on the right side accounts for ionization and excitation losses; E_i is the ionization energy, α_i is the ionization cost factor (taking into account excitation and multistep ionization), and $\nu_i = n_n R_i(T_e)$ is the ionization frequency. Only single ionization will be considered, Dugan's formula[22]

$$\alpha_i(T_e) \simeq 2 + \frac{1}{4} \exp \frac{2E_i}{3T_e},$$

will be used, and the expression for the ionization rate, $R_i(T_e)$, will be taken from Ref.[10].

Equation (4.8) for the internal energy identifies clearly the effects contributing to the electron heating. Thus, it is more adequate to use than the equation for the electron total energy, where the contributions to the internal and mechanical energy are mixed. Indeed, the equation for the mechanical energy comes out from Eqs. (4.4)-(4.5):

$$n_e v_{xe} \frac{d}{dx}\left(\frac{1}{2} m_e v_{\theta e}^2\right) = -v_{xe} \frac{d}{dx} n_e T_e - \nu_e m_e n_e v_{\theta e}^2 + e n_e v_{xe} \frac{d\phi}{dx}. \tag{4.9}$$

Notice that the term on the left side corresponds to the convective contribution, and *must* be neglected when the diffusive limit (4.7) is used.

Tahara *et al.* [53] incur an inconsistency by including the electron mechanical energy in the total energy equation while using, at the same time, the diffusive approximation in the momentum equation. Barral *et al.* [13] proposed a non-stationary model which, in the stationary limit, reduces to Eqs. (4.4)-(4.5) and (4.8). However, (i) in the non-stationary formulation, they omit the temporal term $\partial v_{\theta e}/\partial t$ associated to the azimuthal inertia, and (ii), it is unclear whether they really include the inertia term in the numerical integration, since they omit explicitly a boundary condition for $v_{\theta e}$.

To close the equations for electron dynamics, a transport equation is needed for $\boldsymbol{q}_e$. In the diffusive approximation, that equation is[17]

$$\frac{5}{2} n_e T_e \nabla T_e + e \boldsymbol{q}_e \wedge \boldsymbol{B} + m_e \nu_e \boldsymbol{q}_e \simeq 0,$$

from where the azimuthal and axial components of $\boldsymbol{q}_e$ satisfy

$$0 \simeq -\omega_e q_{xe} - \nu_e q_{\theta e}, \tag{4.10}$$

$$0 \simeq -\frac{5p_e}{2m_e} \frac{dT_e}{dx} + \omega_e q_{\theta e}. \tag{4.11}$$

The resulting equation for q_{xe} coincides with the one obtained by Fife [25] from the postulate of equal diffusitivities for heat and mass transport.

4.2.2 Quasineutral equations

Equations for ions and neutrals are the same as in Model I. Adding them to the above diffusive model for the electrons, the stationary model for the quasineutral plasma consists of

$$\frac{1}{A} \frac{d}{dx}(A n_e v_{xi}) = \frac{1}{A} \frac{d}{dx}(A n_e v_{xe}) = -\frac{1}{A} \frac{d}{dx}(A n_n v_n) = n_e \nu_i, \tag{4.12}$$

$$v_n = \text{const}, \tag{4.13}$$

$$\frac{1}{A}\frac{d}{dx}(Am_i n_e v_{xi}^2) = -en_e\frac{d\phi}{dx} + m_i n_e \nu_i v_n - \frac{dn_e T_i}{dx}, \tag{4.14}$$

$$0 = -\frac{d}{dx}n_e T_e + en_e\frac{d\phi}{dx} - \nu_d m_e n_e v_{xe}, \tag{4.15}$$

$$\frac{1}{A}\frac{d}{dx}A\left(\frac{3}{2}T_e n_e v_{xe} + q_{xe}\right) = -n_e T_e\frac{dv_{xe}}{dx} + \nu_d m_e n_e v_{xe}^2 - \nu_i n_e \alpha_i E_i, \tag{4.16}$$

$$\frac{dT_e}{dx} = -\frac{2m_e\nu_d}{5n_e T_e}q_{xe}. \tag{4.17}$$

Symbols are conventional or were defined already in Ref. [10]. Equations (4.7) and (4.10) have been used to eliminate $v_{\theta e}$ and $q_{\theta e}$ in the Ohm law (4.15) and the Fourier law (4.17), respectively. The axial discharge is governed by two effective frequencies: the axial diffusion frequency for the magnetized electrons,

$$\nu_d = \omega_e^2/\nu_e, \tag{4.18}$$

and the ionization frequency $\nu_i = n_n R_i(T_e)$. The area $A(x)$ and thickness $h(x)$ of the annular cross-section of the plasma jet, remain constant within the channel, and they satisfy

$$\frac{d}{dx}\ln A = \frac{d}{dx}\ln h = \frac{2}{h}\tan\delta = \frac{2c_{pl}}{v_{xi}h}, \tag{4.19}$$

in the plume; here $\delta(x)$ is the 'mean' semi-angle of divergence of the plume and c_{pl} is the velocity of lateral expansion of the plume, which we will define below.

To close the set of Eqs. (4.12)-(4.19), an equation for the ion temperature is needed. For the moment, we apply the ansatz $T_i \ll T_e$, which allows us to neglect the ion pressure in Eq. (4.14) and thus to drop T_i from the equations. The ion temperature and the validity of the ansatz will be discussed later.

The quasineutral model applies between the entrance to the anode sheath (point B) and $x = +\infty$, except for a discontinuity on the electron current at the neutralization surface (point P). The anode sheath must be solved separately, in its own natural scale (the Debye length), and provides boundary conditions for the quasineutral model at point B.

Some magnitudes of interest are the particle flows $\Gamma_\alpha = An_\alpha v_\alpha$, $(\alpha = i, e, n)$; the anode mass flow, $\dot{m}_A = m_i\Gamma_m$, and the discharge current, $I_d = e\Gamma_d$, with

$$\Gamma_m = \Gamma_i(x) + \Gamma_n(x) = \text{const},$$

$$\Gamma_d = \Gamma_i(x) - \Gamma_e(x) = \text{const};$$

the utilization efficiency and the ionization fraction,

$$\eta_u = \eta_{i\infty}, \quad \eta_i(x) = \Gamma_i(x)/\Gamma_m;$$

and the current parameter,

$$i_d = \frac{m_i I_d}{e\dot{m}_A} \equiv \frac{\Gamma_d}{\Gamma_m}.$$

4.3 MODEL INTEGRATION

4.3.1 Singular/sonic points

Solving Eqs. (4.12)-(4.19), with $T_i = 0$, for the spatial derivatives we obtain a matrix relation of the form

$$(1 - M^2)\frac{d\boldsymbol{Y}}{dx} = \boldsymbol{F}(\boldsymbol{Y}), \tag{4.20}$$

where

$$M = \frac{v_{xi}}{\sqrt{T_e/m_i}}$$

is the isothermal Mach number for the ion axial flow, $\boldsymbol{Y}$ groups the eight plasma variables n_e, n_n, v_{xi}, v_{xe}, v_n, T_e, q_{xe}, and ϕ , and $\boldsymbol{F}(\boldsymbol{Y})$ is a regular function. In particular, the scalar equation for v_{xi} can be written as

$$\frac{dv_{xi}}{dx} = \nu_i - v_{xi}\Big[\frac{G}{T_e(1 - M^2)} + \frac{1}{A}\frac{dA}{dx}\Big]$$

with

$$G \equiv -\nu_d m_e v_{xe}\Big(1 - \frac{2q_{xe}}{5n_e T_e v_{xe}}\Big) - \nu_i m_i(2v_{xi} - v_n) + m_i v_{xi}^2 \frac{d\ln A}{dx}. \tag{4.21}$$

Sonic points, $M = \pm 1$, are singular points of Eq. (4.20). Notice that the definition of the Mach number in Model II does not include the specific heat ratio 5/3 of Model I, and function G is different too. As in Ref. [10] we will look for solutions with a regular sonic transition,

$$G_S = 0 \quad \text{and} \quad M_S = 1 \tag{4.22}$$

inside the thruster (point S in Fig. 4.1) and a supersonic plasma flow at the thruster exhaust.

4.3.2 Anode sheath

The Debye sheath attached to the anode (region AB in Fig. 4.1) completes the 1-D model of the channel and defines boundary conditions at point B for the quasineutral equations. Under usual conditions, the sheath is electron-repelling and the space-charge field adjusts the potential jump in the sheath, $\phi_{AB} \equiv \phi_B - \phi_A > 0$, to a value such that the flow of electrons reaching the anode is equal to the diffusive flow coming from the quasineutral channel.

In the distinguished limit $\lambda_D/L \to 0$, the problem in the sheath reduces to collisionless, conservation equations. In particular, particle and energy flows are constant. Assuming a quasi-Maxwellian electron distribution with temperature T_{eB}, electron magnitudes at points A and B are related by

$$\begin{aligned}(n_e v_{xe})_B &= -\frac{1}{4} n_{eB} \exp\frac{-e\phi_{AB}}{T_{eB}}\sqrt{\frac{8T_{eB}}{\pi m_e}},\\ (\frac{5}{2}n_e v_{xe} T_e + q_{xe})_B &= (2T_{eB} + e\phi_{AB})(n_e v_{xe})_B.\end{aligned} \tag{4.23}$$

The matching of this ion-attracting sheath with the quasineutral plasma at point B requires the plasma to verify the Bohm condition

$$M_B = -1, \tag{4.24}$$

which states that the ions must flow into the sheath with the plasma local sound speed. Using Eqs. (4.23) the potential jump across the sheath satisfies

$$\frac{e\phi_{AB}}{T_{eB}} = \ln\sqrt{\frac{T_{eB}}{2\pi m_e v_{xeB}^2}} = \ln\Big(\sqrt{\frac{m_i}{2\pi m_e}}\big|\frac{\Gamma_{iB}}{\Gamma_{eB}}\big|\Big), \tag{4.25}$$

and the electron energy flux deposited by conduction into the anode sheath is

$$q_{xeB} = (n_e v_{xe} T_e)_B \big(\frac{e\phi_{AB}}{T_{eB}} - \frac{1}{2}\big). \tag{4.26}$$

4.3.3 Boundary conditions

Following Refs. [10] and [44] the appropriate velocity for the plume radial expansion is the plasma sound velocity at the thruster exhaust,

$$c_{pl} = \sqrt{T_{eE}/m_i}. \tag{4.27}$$

Equations (4.12)-(4.17) need eight boundary conditions. Seven of them are similar to Model I and there is one additional condition for q_{xe}. The eight conditions are

i)-ii) The injected flow and the velocity of neutrals at the anode, $\dot{m}_A$ and $v_{nA}(= v_{nB})$, are known.

iii) The electron temperature at the neutralization surface, T_{eP}, is known.

iv) The discharge voltage, $V_d = \phi_A - \phi_P$, is known.

v) There is a regular sonic point inside the channel characterized by Eq.(4.22).

vi)-viii) The matching with the anode sheath yields conditions (4.24)-(4.26).

4.3.4 Integration procedure

From the preceding equations and conditions, it turns out that the quasineutral model requires input parameters of different kinds. There are design parameters (A_c, L), control parameters (V_d, $B(x)$, $\dot{m}_A$), plasma parameters(T_{eP}, v_{nB}), and 'empirical' parameters (L_{EP}, α_B). The main output parameters are the discharge current I_d, the thrust F, and the thrust efficiency η, the two last ones to be defined later. Other output parameters of interest are the position of the sonic point, x_S, the divergence angle at the thruster exhaust, δ_E, and several partial efficiencies.

Plasma equations are non-dimensionalized as in Model I; hereafter, an upper tilde will indicate dimensionless variables. Then, they are integrated with Runge-Kutta plus shooting routines from point S towards points B and P independently. This means that plasma parameters at point S are used as input parameters of integration. A Taylor expansion solves the indeterminacy $G_S/(1-M_S^2) = 0/0$ and yields the slopes of plasma variables at point S. Using Eq. (4.21), the regularity condition (4.22) can be expressed as

$$\frac{\nu_i m_i}{\nu_d m_e} = \frac{-v_{xe} + 2q_{xe}/(5n_e T_e)}{2v_{xi} - v_n} \tag{4.28}$$

It is easily seen that this equation relates η_{iS} to $\tilde{T}_{eS}$, $\tilde{q}_{xeS}$, and i_d. The integration uses these three quantities as input parameters instead of the natural ones, $\tilde{T}_{eP}$, $\tilde{q}_{xeB}$, and $\tilde{V}_d$. As a consequence, an iteration is needed to reproduce the desired operating conditions. An additional difficulty of Model II, compared to Model I, is that the solutions departing from point S do not converge easily to the boundary conditions at point B. Thus, we were forced to launch solutions from point S and B separately and to match them at an intermediate point.

Once the region between points B and P is solved the solution is continued to $x = +\infty$ by just exchanging the condition $\Gamma_{xeP^-} = \Gamma_{xiP} - \Gamma_d$ by $\Gamma_{xeP^+} = \Gamma_{xiP}$.

4.4 ANALYSIS OF THE SPATIAL SOLUTION

4.4.1 Axial structure of the discharge

Figure 4.2 shows the axial profiles of main plasma variables for an SPT-100 type of thruster; design and control parameters are given in the figure caption. The discharge presents a similar structure to the one obtained in Model I and sketched in Fig. 4.1, consisting of the anode sheath, the diffusion region, the ionization layer, the internal acceleration region, and the plume. However, heat conduction introduces some differences of relevance. First, there is the desired smoothing of the temperature profile, with a peak temperature around 60 eV, instead of the 90 eV of Model I. Second, the sharp transition between the diffusion and ionization regions found in Model I has been smoothed too, yielding a shorter diffusion region here. Notice that a simple dimensional analysis of Eqs. (4.15)-(4.17) suggests that heat conduction is of the same order of the convective energy flow. Figure 4.2(f) shows that heat conduction is even larger than the convective flow in certain regions (besides, heat conduction is towards the anode in most of the channel, but away from it in the plume).

Plasma equations and boundary conditions seem to force an almost monotonic profile of q_{xe} between B and S. Therefore, q_{xe} at point S is negative and the point of maximum temperature (i.e., $q_{xe} = 0$) is placed downstream of point S, near the channel exit. Function G of Model II, Eq. (4.21), shows that the energy balance allowing the regular sonic transition at point S involves losses by ionization, Joule heating, and heat conduction. However, it turns out that point S is practically in the acceleration region and the ionization contribution to the above balance is small, which makes a difference with Model I. For the case of Fig. 4.2, the ionization layer ends at $x_H \sim 15.3$ mm approximately, and we have $x_S \simeq 16.4$ mm, and $q_{xe} = 0$ at $x \simeq 22.6$ mm.

Figure 4.3(a) compares the contributions of different collision terms to the electron collision frequency ν_e. The main conclusion is that Bohm-like diffusion provides the main contribution downstream of the ionization layer, a result supported experimentally by ν_e by Meezan and Capelli[42]. However, we still adjust α_B 'empirically' to obtain a satisfactory solution; the value we use is of the order of the one used by Fife[25], and both are much smaller than the 'classical' value of Bohm. Figure 4.3(a) shows that $e-i$ collisions dominates over $e-n$ collisions in the rear part of the channel; this is due to the high electron density and low electron temperature arising when the ionization region is thin.

Figure 4.3(b) depicts the two frequencies governing the axial discharge, ν_i and $\bar{\nu}_d = \nu_d m_e/m_i$ [with the mass ratio in $\bar{\nu}_d$ coming out from the dimensional analysis of Eqs. (4.12)-(4.17)]. The plots show that $\nu_i \ll \bar{\nu}_d$ even at the peak of ν_i. This makes the structure of the diffusion plus ionization region (region BH in Fig. 4.1) not simple to analyze: on the one hand, η_i, v_{xi}, and the total length L_{AH} of the region are governed by ν_i; on the other hand, Eqs. (4.15) and (4.17) yield that the profile of n_e and T_e are controlled mainly by $\bar{\nu}_d$. Changes of ϕ in region BH are small, of the order of T_e there; for the case of Fig. 4.2, one has that ϕ increase by 1 V from point B to the point with $v_{xi}=0$, and the voltage drop between point B and point S (already in the acceleration region) is $\phi_{BS} \simeq 23.1$V only.

The structure of the internal and external acceleration regions (region HP in Fig. 4.1) is simpler because ionization is negligible there. The quasineutral model simplifies to the conservation relations

$$\Gamma_\alpha \equiv A n_\alpha v_\alpha = \text{const}, \tag{4.29}$$

$$\frac{1}{2} m_i v_i^2 + e\phi = \text{const}, \tag{4.30}$$

$$\frac{5}{2} T_e - e\phi + \frac{q_{xe}}{n_e v_{xe}} = \int T_e \, \mathrm{d}\ln A, \tag{4.31}$$

plus Eqs. (4.15) and (4.17) for electron momentum and heat conduction. These two last equations show that $\int(-v_{xe}) m_e \nu_d dx$ is the relevant integration variable for the acceleration regions. Quasineutrality and Eq. (4.29) state the electrons must counterflow against the ions with a velocity

$$-v_{xe} = (i_d/\eta_u - 1) v_{xi}. \tag{4.32}$$

Adding to these facts the conditions that the ion low is mostly supersonic and most of the voltage drop takes place in the region HP, the integration of Eq. (4.15) yields

$$\sqrt{\frac{2eV_d}{m_i}} \sim \int_H^P \left(\frac{i_d}{\eta_u} - 1\right) \frac{m_e \omega_e^2}{m_i \nu_e} dx. \tag{4.33}$$

This expression suggests

$$V_d^{1/2} \propto (i_d - 1) \frac{B_{max}^2}{\nu_e} L_{HP} \tag{4.34}$$

as an important scaling law among the main thruster parameters for efficient operation.

Kim derived a similar law[38]. Then, assuming that (i) $L_{HP} \sim$ const (for a given geometry), (ii) $i_d - 1 \sim$ const, and (iii) $\nu_e \sim V_d^{1/2}/h_c$ (from an estimate based in the dominance of wall collisions and h_c being the channel width), he concluded that optimum operation required $B_{max} \propto V_d^{1/2}$. Curiously, when Bohm diffusion dominates one has $\nu_e \sim \alpha_B B_{max}$ and the scaling law $B_{max} \propto V_d^{1/2}$ still holds, provided that the condition $i_d - 1 \sim$ const applies. We will come back to this discussion on optimum operation in Sec.4.6.2.

4.4.2 Inertial effects on electrons

We evaluate now the assumptions of closed-drift and diffusive electron dynamics. Figure 4.4 plots, for the case of Fig.4.2, three parameters related to electron dynamics: the inverse Hall parameter, the drift-to-internal energy ratio, and the convective-to-magnetic time ratio. We see, first, that the closed-drift approximation, Eq. (4.3), is verified in the whole domain, even near the cathode, where the magnetic field is vanishing. However, the diffusive approximation, Eq. (4.6), fails in the vicinities of anode and cathode. Electron convective effects around the anode come from $v_{xe} \propto v_{xi}$ and the acceleration of the plasma having to meet the Bohm condition at point B. These effects are rather local and we believe they are not significant globally. On the contrary, the inertia effects in the plume could have more impact in the plasma discharge since they are less localized and the magnetic field becomes residual there. From Eq. (4.5), one has

$$\frac{v_{xe}}{v_{\theta e}} \simeq -\frac{\nu_e}{\omega_e + dv_{\theta e}/dx} \sim -\frac{\nu_e}{\omega_e}(1 - \frac{dv_{\theta e}}{dx}), \tag{4.35}$$

with $dv_{\theta e}/dx < 0$ in the plume, yielding thus a larger value of $v_{xe}/v_{\theta e}$ than the diffusive approximation. This can be interpreted as an extra collisionality and could be an important and independent contribution to the overall 'anomalous' diffusion. However, without solving the coupled equations (4.4)-(4.5) together with the other ones, it is difficult to predict the overall effect of the convective term on the discharge characteristics.

In spite of the large values reached by the convective azimuthal term, Fig. 4.4 shows that the drift energy remains small in the whole domain. The explanation lies in the azimuthal inertia term of Eq. (4.5) being balanced by the azimuthal component of the Lorentz force, which yields no contribution to the drift energy. In any case, we must be aware that $v_{\theta e}$ is very sensitive to the local values of the magnetic and electric fields, and relatively small variations of these magnitudes could make $m_e v_{\theta e}^2/2T_e \sim 1$ locally, as it has been found in the experiments of Haas and Gallimore[32]. Were this the case, the drift energy should be taken into account to compute the ionization rate, R_i.

4.4.3 Ion temperature

The evolution equation for the ion temperature is

$$v_{xi}\frac{d}{dx}\frac{3}{2}T_i = -\frac{T_i}{A}\frac{d}{dx}Av_{xi} + \nu_i\big[\frac{1}{2}m_i(v_{xi} - v_{xn})^2 + \frac{3}{2}(T_n - T_i)\big], \qquad (32) \qquad (4.36)$$

where T_n is the temperature of neutrals (which we are ignoring). Equation (32) requires a boundary condition for T_i and, at the same time, introduces a new singular point at $v_{xi} = 0$. The correct boundary condition for a regular solution comes from making zero the right-hand side of Eq. (32) at $v_{xi} = 0$: this yields $T_i = (3T_n + m_i v_{xn}^2)/5$. Again a Taylor-expansion problem must be solved to determine the value of dT_i/dx for a regular crossing.

Figure 4.5 plots $T_i(x)$, obtained from the integration of Eq. (4.36) using $v_{xi}(x)$ and $A(x)$ from the cold-ion solution of Fig. 4.2, and $T_n/T_e \to 0$. It confirms that T_i is totally negligible and the ion beam behaves as monoenergetic. Clearly, the small value of T_i and the drawback of a new singular point at $v_{xi} = 0$ makes inadvisable to add Eq. (4.36) to the set of Eqs. (4.12)-(4.19).

The low ion temperature is due to the short ionization region and the absence of lateral recombination. The experimental Retarding Potential Analyzer data show that $T_i \sim 2 - 3$ eV at exit. The discrepancy might be related to the spreading of the ionization zone when there is wall recombination; ion-ion and ion-neutral collisions could contribute too.

4.5 THRUST AND EFFICIENCY

4.5.1 Thrust

The electrostatic interaction between ions and electrons plus the magnetic forces on the electrons are the mechanisms by which plasma thrust is transferred to the solids parts of the engine. Since the magnetic field extends some distance outside the chamber and the plasma plume presents some radial divergence, neither the momentum thrust of the plasma at the chamber exhaust (point E) nor in the far plume (point ∞) evaluate accurately the thrust.

Assuming the engine to be at rest by some thrust balance device and zero external pressure, the axial momentum balance for the system constituted by the thruster plus the internal plasma yields

$$F = F_{pE} + F_{ext}, \tag{4.37}$$

where F is the thrust (exerted on the thruster balance),

$$F_p(x) = \left(m_i n_i v_i^2 + m_i n_n v_n^2 + n_e T_e\right) A \tag{4.38}$$

is the total axial momentum of the plasma at a given axial section, and

$$F_{ext} = \int_E^\infty (-e n_e \boldsymbol{v}_e) \wedge \boldsymbol{B} \cdot \mathbf{1}_x A(x) dx \simeq \int_E^\infty e n_e v_{\theta e} B A(x) dx \tag{4.39}$$

is the external thrust due to the magnetic force on the electrons *in the plume.* Therefore, the leakage of the magnetic field outside the thruster channel yields a contribution to the thrust, which is a unique characteristic of this type of electric thrusters.

From Eq. (4.14)-(4.15), the axial momentum of the whole plasma satisfies

$$\frac{dF_p}{dx} = n_e T_e \frac{dA}{dx} + e n_e v_{\theta e} B A, \tag{4.40}$$

where we wrote $e v_{\theta e} B \simeq -v_{xe} \nu_d$ for the magnetic force exerted on an electron. Integrating Eq. (4.40) along the plume and using Eq. (4.37) one has

$$F = F_{p\infty} - D_{ext}, \tag{4.41}$$

where

$$D_{ext} = \int_E^\infty n_e T_e \frac{dA}{dx} dx \tag{4.42}$$

is a drag contribution due to the plume lateral expansion. Expressions (4.37) and (4.41) yield the difference between the actual thrust and the momentum thrust at points E and ∞. One has

$$F_{p\infty} - F_{pE} = F_{ext} + D_{ext}, \tag{4.43}$$

which means that the external acceleration of the ions is transferred only partially to thrust (via ion-electron electrostatic interaction plus electron-thruster magnetic interaction). A relevant point is that were the magnetic field zero outside the thruster, all external acceleration would go to plume radial expansion. For the case of Fig. 4.2 we have that the contribution of the external magnetic field amounts to $F_{ext}/F \simeq 15.8\%$ whereas the external acceleration of ions is $(F_{p\infty} - F_{pE})/F \simeq 19.7\%$.

4.5.2 Thrust efficiency

The thrust efficiency is defined as

$$\eta = \frac{F^2}{2\dot{m}_A I_d V_d}, \tag{4.44}$$

and is conveniently factorized into four terms

$$\eta = \eta_u \eta_d \eta_e \eta_o, \tag{4.45}$$

where η_u is the utilization efficiency, and

$$\eta_d = \frac{I_{i\infty}}{I_d} \equiv \frac{\eta_u}{i_d} \quad \eta_e = \frac{m_i v_{xi\infty}^2}{2eV_d}, \quad \eta_o = \frac{F^2}{(m_i \Gamma_i v_{xi})_\infty^2}, \tag{4.46}$$

are efficiencies for discharge, beam-energy, and other effects (plume expansion, anode sheath,...), respectively. For the case of Fig. 4.2, one has $\eta_u \simeq 100\%$, $\eta_d \simeq 85.6\%$, $\eta_e \simeq 101.4\%$, $\eta_o \simeq 93.4\%$, and $\eta \simeq 81.1\%$; the thin ionization region and the fact that the maximum voltage is not at point A but at $v_{xi} = 0$ are responsible of $\eta_e > 100\%$. Notice that the definition of η is based in the anode mass flow and does not include the power spent in the magnetic circuit.

The discharge efficiency is the main factor reducing the thrust efficiency. The relation between η_d (or i_d) and the ionization losses is deduced from the energy balance for the whole plasma. From the model equations, the energy balance for the plasma is

$$I_d V_d = \sum_{\alpha=i,e} (W_{\alpha\infty} - W_{\alpha A}) + Q_{ion} \tag{4.47}$$

with

$$W_\alpha = \left[n_\alpha v_{x\alpha} (\frac{1}{2} m_\alpha v_{x\alpha}^2 + \frac{5}{2} T_\alpha) + q_{x\alpha}\right] A \tag{4.48}$$

the energy flow rate of each species, and

$$Q_{ion} = \int_A^\infty \nu_i \alpha_i E_i n_e A dx \tag{4.49}$$

the ionization losses. Grouping in Eq. (4.47) the non-dominant contributions into Q_r, and calling $W'_{i\infty} = \frac{1}{2} m_i (n_i v_{xi}^2)_\infty$ the energy balance becomes

$$I_d V_d = W'_{i\infty} + Q_{ion} + Q_r. \tag{4.50}$$

From the efficiency definitions and for $\eta_u, \eta_e \sim 1$, one has

$$i_d - 1 \simeq 1 - \eta \sim \frac{Q_{ion} + Q_r}{I_d V_d}. \tag{4.51}$$

This expression together with Eq. (4.49) complements the scaling law (4.34). For the case of Fig. 4.2, one has $Q_{ion}/I_d V_d \simeq 9.3\%$ and $Q_r/I_d V_d \simeq 3.7\%$ (with $q_{xe\infty}$ the main contribution to Q_r).

4.6 THRUSTER PERFORMANCE

4.6.1 Domain of stationary solutions

Model I showed that the parametric domain of stationary solutions was restricted to $\eta_{iB} \leq 0$ (i.e. $\Gamma_{iB} \leq 0$). When the thruster parameters cross the line $\eta_{iB} = 0$ the plasma is unable to provide the ion back-flow needed to keep plasma quasineutrality near the anode, and an oscillatory plasma response is expected. Indeed, both in Ref. [10] and here we are being more restrictive with the minimum value of $|\eta_{iB}|$. The anode sheath vanishes when $\phi_{AB} = 0$, which, from Eq. (4.25), corresponds to

$$\frac{-\eta_{iB}}{i_d - \eta_{iB}} = \sqrt{\frac{2\pi m_e}{m_i}}, \quad v_{xeB} = -\sqrt{\frac{T_{eB}}{2\pi m_e}}. \tag{4.52}$$

Although it is possible to extend Model II to treat cases with no anode sheath, we will take the case of sheath collapse as the practical limit of existence of stationary solutions. Two are the reasons: first, the limit $\Gamma_{iB} = 0$ is very close; and second, Eq. (4.52) [and Fig. 4.4] show that the electron velocity when $\phi_{AB} = 0$ is formally beyond the limit of validity of the diffusive model.

An important novelty of Model II is that heat conduction introduces an upper restriction to $|\eta_{iB}|$. This comes from the Bohm condition at point B. To have $dv_{xi}/dx|_B \geq 0$ requires $G_B \geq 0$, which using Eq.(4.21) and $\nu_{iB} \simeq 0$ means

$$q_{xeB} \leq \frac{5}{2}(n_e T_e v_{xe})_B. \tag{4.53}$$

Were $G_B < 0$, the reverse ion velocity would reach a minimum subsonic value at an intermediate point and the sonic condition at point B would not be met. Physically, this means again the impossibility to establish a stationary sheath at the anode, and a possible oscillatory response of the plasma.

Using Eqs. (4.25) and (4.26), Model II restricts the domain of of stationary solutions to

$$0 \leq e\phi_{AB}/T_{eB} \leq 3, \tag{4.54}$$

or, in terms of plasma currents (and for xenon),

$$5 \cdot 10^{-3} \leq |I_{iB}|/I_d \leq 0.114.$$

4.6.2 Optimum performance

Figure 4.6(a) shows the domain of stationary solutions in the plane of input parameters (V_d, B_{max}). Figures 4.6(b)-4.6(d) depict the corresponding bands of output parameters. As expected from Eq. (4.54) the domain of solutions is rather narrow. Figure 4.6(b) confirms two known features of the specific impulse $I_{sp} = F/\dot{m}$: first, it is proportional to $V_d^{1/2}$ and, second, it is practically independent of the magnetic field strength (within the high efficiency regime). More interesting to discuss are the other plots.

Figure 4.6(a) shows that B_{max} must increase with V_d to maintain a stationary solution. This same trend is found experimentally for optimum thruster performance, which supports that optimum performance is related to a non-oscillatory response. Accepting that idea, Fig. 4.6(a) suggests

$$B_{max} \propto V_d \tag{4.55}$$

as the correct law for optimum performance, instead of $B_{max} \propto V_d^{1/2}$ proposed by Kim. The discrepancy comes from the behavior of $i_d - 1$, which Kim assumed independent of V_d, whereas, in our case, Figs. 4.6(c) and 4.6(d) suggest the laws

$$i_d - 1 \sim 1 - \eta \propto V_d^{-1/2}. \tag{4.56}$$

This last behavior can be justified from Eq. (4.51). First, for zero wall losses, one expects $T_e \propto V_d$; indeed, our computations yield

$$T_{e,max} \simeq V_d/5, \tag{4.57}$$

with $T_{e,max}$ the maximum electron temperature (but we could not find a precise justification of the factor 1/5). Then, from Eq. (4.49), one has

$$Q_{ion} + Q_r \sim Q_{ion} \propto \nu_i \propto T_e^{1/2} \propto V_d^{1/2}, \tag{4.58}$$

assuming n_e to be weakly affected by V_d. Since $i_d - 1$ is small, we can take $I_d = \dot{m} i_d \simeq$ const in Eq. (4.51), leading finally to the scaling law (4.56).

The scaling law (4.55) and the increase of η with V_d were obtained also by Blateau *et al.*in their simulation model (with metallic walls) [18]. Experimental data by Manzella *et al.* [41] with a thruster with ceramic walls, fit well with $B \propto V_d^{1/2}$ but η does not increase clearly with V_d. Therefore, our conclusions are that Eqs. (4.34) and (4.51) seem to be the main relationships among thruster parameters, whereas the particular scaling laws for the evolution of B_{max} and $(1 - \eta)$ with V_d depend on the thruster operating point and the mechanism dominating energy losses.

4.7 CONCLUSIONS

The inclusion of heat conduction in our previous Model I has produced the following changes in both the treatment of the mathematical model and the stationary solutions: (i) a new boundary condition on the heat flow at the anode is needed, (ii) the singular points are modified, (iii) the integration procedure requires more involved iteration routines, and (iv) a new restriction to the parametric domain of stationary solutions has arisen. The new restriction bounds the maximum ion reverse flow compatible with a Bohm transition to the anode sheath, and depends very much on the new boundary condition. The lower and upper bounds on the ion reverse flow leave the parametric domain of stationary solutions rather narrow. Since both bounds on the ion flow are related to the establishment of a stationary anode sheath, oscillatory responses are expected outside the parametric region of stationary solutions.

Model II recovers an axial structure of the discharge consisting mainly of the diffusion plus ionization regions, on the rear part of the chamber, followed by the internal and external acceleration regions. The conductive energy transport turns out to be as important as the convective one and is able to smooth the temperature profile. Because of the short ionization region, the ion temperature is found to be negligible, and the transmission of electrostatic energy into the monoenergetic ion beam is very efficient.

The discussion of the inertial effects in the electron dynamics and the electron drift energy has yielded some important conclusions. First, it has been shown that the dominant inertial term comes the azimuthal electron motion. Second, this term can produce an anomalous-like collisionality in the near-plume, which could be an important feature to understand the plasma discharge there; further investigation on this issue seems crucial. Third, the fact that the electron inertia can be significant in a certain region does not imply necessarily the electron drift energy to be important too.

A detailed evaluation of the thrust has determined the external contribution coming from the magnetic force between thruster and external electrons. This external thrust is a fraction of the ion acceleration in the plume, which is transmitted to the electrons through the quasineutral electrostatic field. Another fraction of the ion acceleration goes to the plume radial expansion and does not produce thrust. Indeed, the external thrust would be zero if the magnetic field did not leak outside the thruster chamber. Therefore, for more accurate computations it is very important to have an accurate knowledge of the profile of the external magnetic field, the approximate position of the neutralization surface, and the external electron dynamics.

A relevant novelty of Model II is that the parametric domain of stationary solutions is very narrow. This is the consequence of upper and lower restrictions on the ion back-flow needed to sustain a steady solution near the anode. The domain of steady discharges in the (B_{max}, V_d) plane seems to agree with the experimental curves for optimum performance. The two basic relationships among governing parameters at optimum operation have been derived. Both scaling laws $B_{max} \propto V_d$ and $B_{max} \propto V_d^{1/2}$ are possible depending on the main mechanism for energy losses, which determines the scaling law for $(1 - \eta)$ too.

The high thrust efficiency obtained by Model II (about 75-85% based in the anode mass flow) and the still high peak temperature, indicate that energy losses due to the plasma interaction with lateral walls (in thrusters with long, ceramic chambers, which are the main reference for our model) are an effect of dominant order, which produces energy losses as large as the ionization ones; this would agree with the results reported by Kim[38]. Therefore, efforts made to include in a consistent way this wallinteraction into Model I [7] will be extended to Model II.

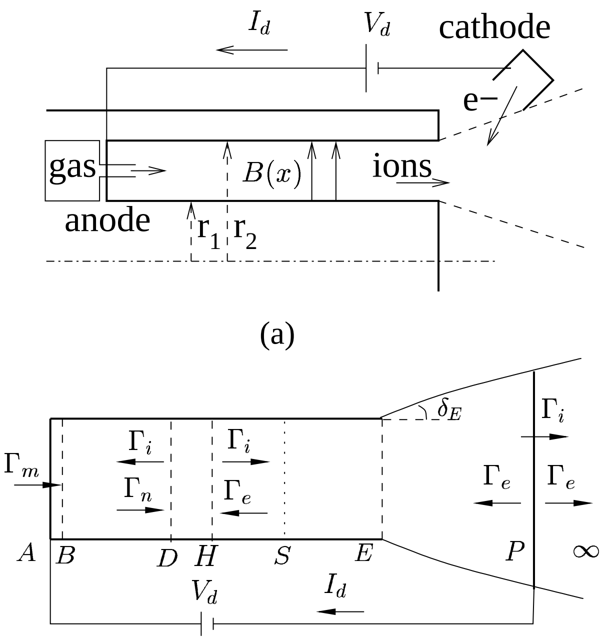
I_d
V_d
cathode
e−
gas
$B(x)$
ions
anode
r$_1$
r$_2$
δ_E
Γ_i
Γ_m
Γ_i
Γ_n
Γ_i
Γ_e
Γ_e
Γ_e
A
B
D
H
S
E
P
∞
V_d
I_d

(a)

(b)

Figure 4.1: Sketches of (a) the Hall thruster, and (b) the axial model. $\Gamma_\alpha = A_c n_\alpha v_{x\alpha}$, $\alpha = i, e, ...$ are axial flows of particles of the different species. Point A is the anode, point P is the neutralization surface, and point S is the forward sonic point of the ion flow. Plasma regions: AB is the anode sheath, BD the diffusion region, DH the ionization layer, HE the internal acceleration zone, EP the near-plume, and P∞ the far-plume.

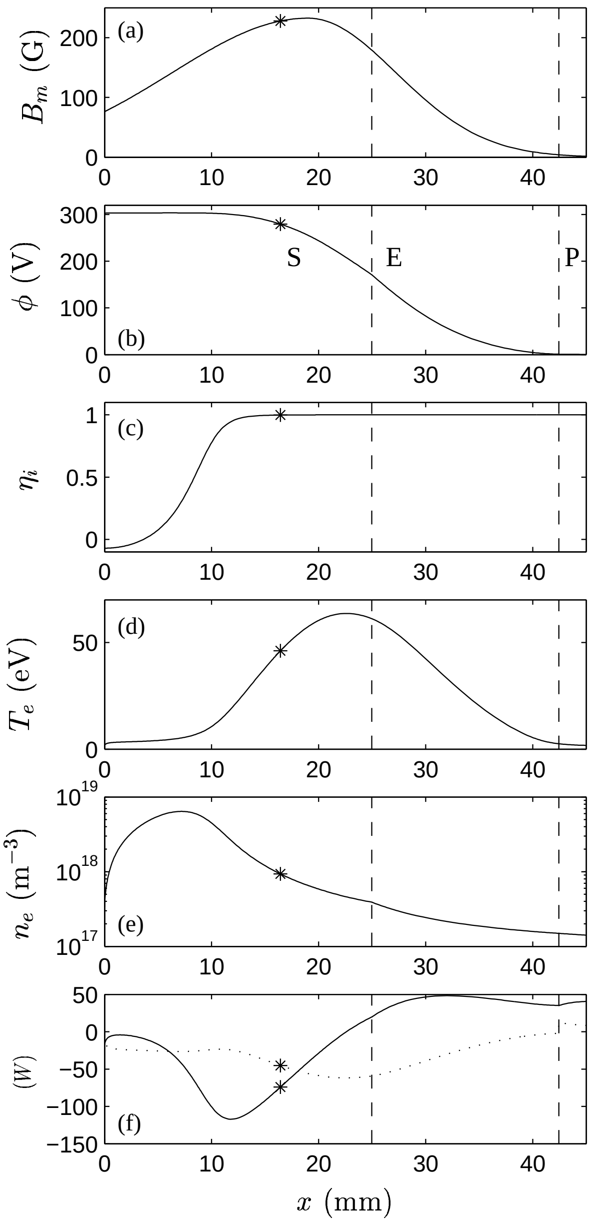

Figure 4.2: Axial structure of the plasma for xenon, $L = 25$mm, $L_{EP} = 17.4$mm, $A_c = 45\text{cm}^2$, $\dot{m}_A = 5.3$mg/s, $V_d = 298$V, $T_{eP} = 2.5$eV, $16\alpha_B \simeq .068$, and $B(x)$ as shown in (a). Output parameters: $I_d = 4.51$ A, $F = 0.108$ N, $\eta = 80.8\%$, $\eta_{iB} = -7.1\%$, $\phi_{AB} \simeq 4.4$ V, $x_S = 16.4$ mm, $\delta_E \simeq 25.7$ deg. The vertical, dashed lines are the thruster exhaust and the neutralization surface; the asterisk situates point S. In (f) the solid line corresponds to the conductive electron power, $A_c q_{xe}$, and the dashed line to the convective one, $A_c \frac{5}{2} T_e n_e v_{xe}$.

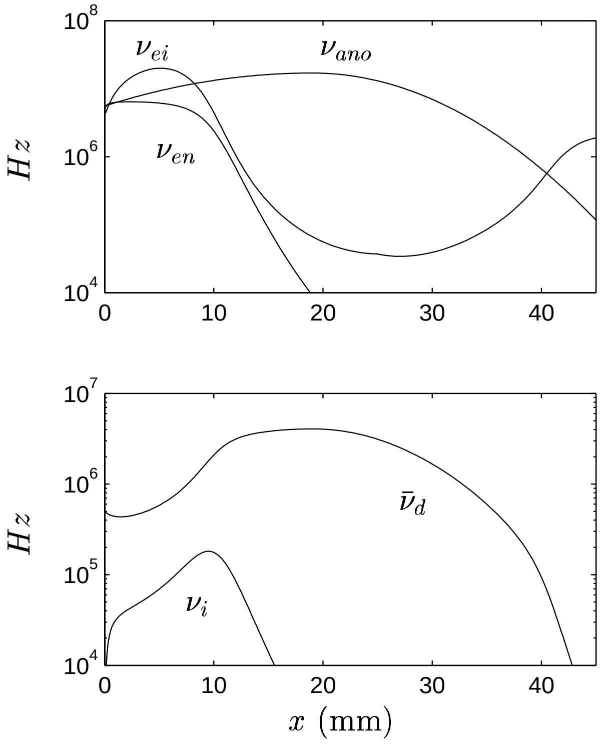

Figure 4.3: For the solution of Fig. 4.2: (a) contributions of different processes to the total electron collision frequency ν_e; and (b) ionization frequency, ν_i, and axial electron diffusion frequency, $\bar{\nu}_d = \nu_d m_e/m_i$.

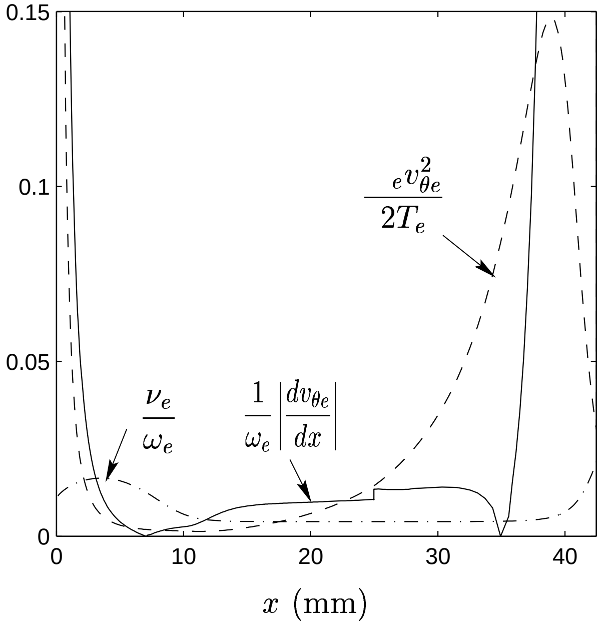

Figure 4.4: Profiles of the Hall parameter, ω_e/ν_e, the drift-to-internal energy ratio, $m_e v_{\theta e}^2/2T_e$, and the convective-to-magnetic time ratio, $\omega_e^{-1}|dv_{\theta e}/dx|$, for the case of Fig. 4.2.

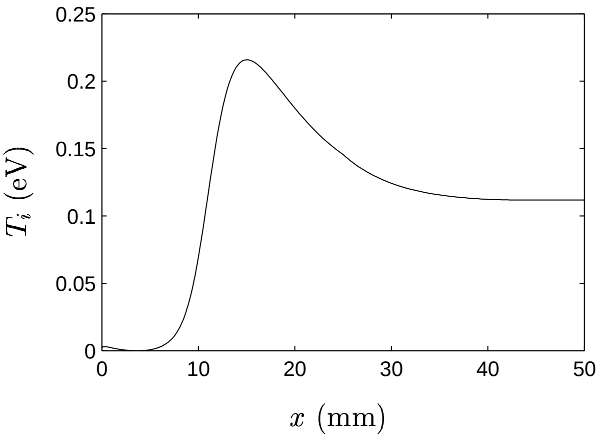

Figure 4.5: Profile of the ion temperature for the case of Fig. 4.2.

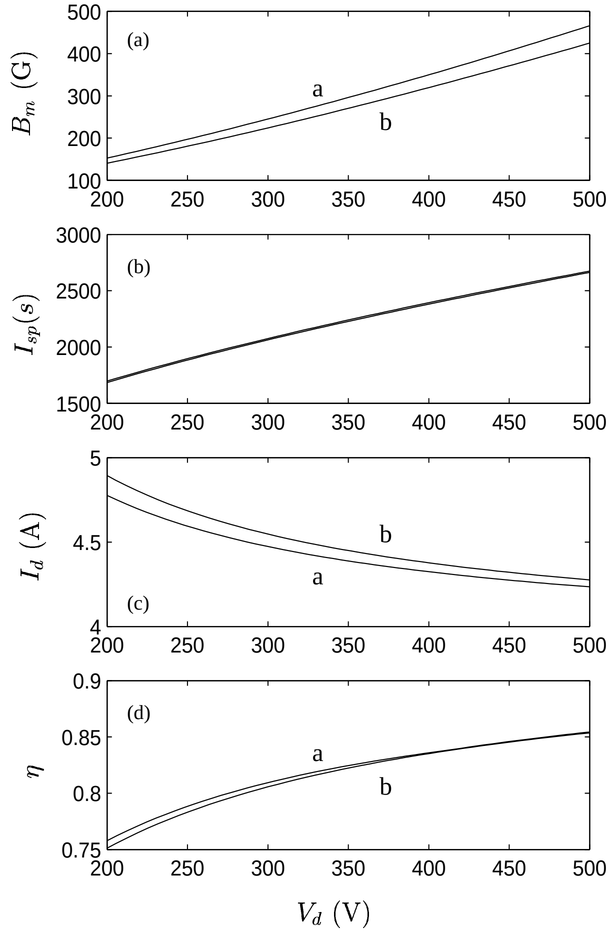

Figure 4.6: Band of stationary solutions for input parameters V_d and B_{max} as in (a) and the rest of input parameters as in Fig. 4.2; $I_{sp} \equiv F/\dot{m}_A$. Lines 'a' and 'b' correspond to the lower ($\phi_{AB} = 0$) and upper ($G_B = 0$) restrictions to $|\eta_{iB}|$.

Chapter 5

AXIAL MODEL WITH LATERAL WALL EFFECTS

5.1 INTRODUCTION

The walls of the discharge channel of the SPT class of Hall thrusters is made of a ceramic insulator. The interaction of the plasma with these dielectric walls affects greatly the plasma discharge and the thruster characteristics[46]. From simple reasoning several phenomena are expected. First, the zero current condition at the dielectric wall implies, in general, the formation of an electron-repelling sheath there. Second, ions attracted to the walls are recombined, thus reducing the actual propellant utilization and the thruster efficiency. Third, energetic electrons arriving at the wall deposit their energy there, affecting the average temperature of the plasma in the channel and, consequently, the ionization process. Four, ceramic materials present large yields for secondary electron emission. On the one hand, these electrons modify the sheath structure, which could attain charge saturation conditions[36]. On the other hand, since these electrons are replacing primary electrons, which were magnetically-guided, there is an extra near-wall collisionality for the average electron population[21].

The effects of the radial interaction can be taken into account in a one-dimensional(1D), radially-averaged model of the discharge through appropriate source terms for the different radial phenomena [26, 11]. However, an accurate form of these terms requires to know in detail the radial plasma response and this is not a simple problem. A variety of phenomena come into play, like the formation of a radial presheath/sheath structure, the wall secondary electron emission(SEE), the trapping of the SEE into the main plasma, the sheath charge-saturation, the annular geometry of the chamber, and the effects of the axial flow on the radial dynamics. References [3, 2, 12] present the development of a detailed radial presheath/sheath model, which tries to include all this phenomena.

This chapter analyzes solutions resulting from the inclusion of radial-interaction terms into the axial model with heat conduction of Ch. 4. The modeling of radial effects is the same presented in Ref. [7], which is valid for total-trapping of SEE. Related work from other authors is found in Refs. [25, 13].

5.2 MODEL FORMULATION

Figure 5.1 presents a geometrical sketch of the axial model; for the radial model see Ref. [12]. We summarize here the general hypotheses of the 1D axial model, already discussed in previous works [7, 5]. In the 1D axial approximation, plasma variables represent average values on each cross-section and depend only on the axial variable x. The macroscopic formulation consists of fluid-like equations for ions(i), electrons(e) and neutrals(n). The annular channel is of length $L_c \equiv x_E - x_A$, radial area A_c, and radial width h_c. The plasma discharge extends outside the thruster into a plasma plume of varying radial area $A(x)$. The magnetic field is considered purely radial, $\boldsymbol{B} = B(x)\mathbf{1}_r$, with the maximum field, B_{max}, placed near the thruster exit, and different semi-Gaussian axial profiles are used for $B(x)$ inside the thruster and in the near-plume. Electrons are injected into the plume at a neutralization surface (point P) placed at a distance $L_{cat} \equiv x_P - x_E$ from the channel exit (point E). The voltage difference between anode (point A) and point P is the discharge voltage, V_d, and the electron current delivered at the neutralization surface is the discharge current, $I_d \equiv e\Gamma_d$. One part of this current flows outwards and neutralizes the ion beam current there, I_{iP}; the other part, $I_d - I_{iP}$, diffuses inwards across the radial lines of the applied magnetic field and ionizes the mass flow of neutrals, $\dot{m}_A \equiv m_i\Gamma_m$, injected at the anode. Only single ionization is considered. Subscript ∞ will refer to downstream conditions far away from the cathode P.

The plasma is considered quasineutral everywhere except in a thin, electron-repelling sheath attached to the anode (region AB in Fig. 5.1, with $x_B \simeq x_A = 0$ in the quasineutral scale). The macroscopic equations for the quasineutral plasma are [7]

$$\frac{d\Gamma_i}{dx} = \frac{d\Gamma_e}{dx} = -\frac{d\Gamma_n}{dx} = An_e(\nu_i - \nu_w), \tag{5.1}$$

$$\begin{aligned}\frac{1}{A}\frac{d}{dx}(m_i v_{xi}\Gamma_i) &= -en_e\frac{d\phi}{dx} \\ &\quad + m_i n_e(\nu_i v_n - \nu_w v_{xi}),\end{aligned} \tag{5.2}$$

$$\frac{d}{dx}(m_i v_n \Gamma_n) = Am_i n_e(\nu_w v_{nw} - \nu_i v_n), \tag{5.3}$$

$$0 = -\frac{d}{dx}n_e T_e + en_e\frac{d\phi}{dx} - \nu_d m_e n_e v_{xe}, \tag{5.4}$$

$$\begin{aligned}\frac{1}{A}\frac{d}{dx}\left(\frac{5}{2}T_e\Gamma_e + q_{xe}A\right) &= en_e v_{xe}\frac{d\phi}{dx} \\ &\quad - \nu_i n_e \alpha_i E_i - \nu_{we} n_e T_e,\end{aligned} \tag{5.5}$$

$$\frac{dT_e}{dx} = -\frac{2m_e\nu_d}{5n_e T_e}q_{xe}, \tag{5.6}$$

For a complete listing of symbols and definitions see Ref. [10] and Ch. 4. The ionization frequency follows $\nu_i = n_n R_i(T_e)$; the axial diffusion frequency ν_d for the magnetized electrons satisfies Eq. (4.18) with

$$\nu_e = \nu_{en} + \nu_{ei} + \alpha_{ano}\omega_e + \nu_{wm}$$

the electron collision frequency, grouping contributions from $e - n$ and $e - i$ collisions, Bohm anomalous diffusion [35], and effective wall collisions; ν_w and ν_{we} are frequencies accounting for particle and energy losses, to be defined below; v_{nw} is the axial velocity of ions after wall recombination and accommodation. $\Gamma_\alpha = An_\alpha v_\alpha, \alpha = i, e, n$ are particle flows, and follow $\Gamma_n + \Gamma_i = \text{const} = \Gamma_m$, and $\Gamma_i + \Gamma_e = \text{const} = \Gamma_d$. The area $A(x)$ and thickness $h(x)$ of the plasma jet cross-section, are constant within the channel and satisfy Eq. (4.19) in the plume.

The radial plasma-wall interaction is modeled through the effective frequencies [7]:

$$\nu_w = \tilde{\nu}_w h_c^{-1}\sqrt{T_e/m_i}, \tag{5.7}$$

$$\nu_{wm} = \beta_m \nu_w, \quad \beta_m(\delta_w) = \frac{\delta_w}{1-\delta_w}, \tag{5.8}$$

$$\nu_{we} \simeq \beta_e \nu_w, \quad \beta_e(\delta_w) \sim 5.62 + \frac{1.65}{1-\delta_w}, \tag{5.9}$$

Here, $\tilde{\nu}_w(x)$ is a dimensionless parameter, which depends on the characteristics of the radial response in each axial position; since there is not yet an accurate way to estimate it, we just take $\tilde{\nu}_w(x)$ constant and equal to a value fitting the experimental data. Functions $\beta_m(\delta_w)$ and $\beta_e(\delta_w)$ depend on the effective secondary emission yield,

$$\delta_w(T_e) \simeq \begin{cases} \sqrt{T_e/T_1}, & T_e \leq T_e^* \\ \\ \delta_w^* & T_e > T_e^* \end{cases} \tag{5.10}$$

with T_1 the electron temperature of a quasi-Maxwellian electron population for 100% SEE, and $\delta_w^* \simeq 0.983$, $T_e^* \simeq 0.967\ T_1$, the values of the SEE yield and the electron temperature for the lateral sheaths to be charge-saturated (yielding $\beta_m^* \sim 60$ and $\beta_e^* \sim 105$). The value of T_1 is estimated from $T_1 \sim 0.66 E_1$, with E_1 the energy of a monoenergetic beam yielding 100% SEE; E_1 depends on the wall material and is the quantity generally found in empirical data. Notice that, since T_e changes along the channel, the sheath properties (potential drop, SEE yield, etcetera) are local too. In particular, the lateral sheaths are not expected to be charge-saturated along the whole channel. For the axial velocity of neutrals created by recombination at lateral walls, v_{nw}, we assume it depends on a wall accommodation factor a_w, through $v_{nw} = a_w v_n + (1 - a_w) v_{xi}$.

5.2.1 Boundary conditions and structure of the discharge

Since the radial-source terms do not modify the mathematical characteristics of the set of equations, the treatment of the present model is identical to the no wall-losses case developed in Ch. 4. The eight boundary conditions (5 at point B, 2 at point P, and one at the sonic point S) and the numerical integration algorithm are the same now. We remind that these boundary conditions correspond to solutions including an anode sheath AB and a region BD of reverse ion flow (Fig. 5.1). This type of solutions would represent conditions of optimum thruster operation. According to Ch. 4, these solutions exists only in a narrow interval of reverse flows, from $-\eta_{iB} \sim 1\%$ to $-\eta_{iB} \sim 12 - 18\%$, roughly, where $\eta_i = \Gamma_i(x)/\Gamma_m$ is the ion flux ratio.

5.3 STRUCTURE OF THE DISCHARGE

Figures 5.2 to 5.5 show axial profiles of the main plasma variables for a particular operation point of a SPT-100 type of thruster. Design and control parameters are given in the caption of

Fig. 5.2 and the profile of the radial magnetic field is in Fig. 5.2(a); the thruster exhaust is at $x_E = 25$ mm and the neutralization surface at $x_P = 33.5$ mm.

Points D and S, delimiting the ionization region are placed at $x_D \sim 2.6$mm and $x_S \simeq 12.9$ mm. The ion flux ratios at different locations are $\eta_{iB} \simeq -3\%$, $\eta_{iS} \simeq 79.9\%$, $\eta_{iE} \simeq 82.3\%$, $\eta_u \equiv \eta_{i\infty} \simeq 83.3\%$. Figure 5.3(a) shows the axial evolution of both the particle production and recombination terms,

$$S_i = Aen_e\nu_i, \quad S_w = Aen_e\nu_w, \tag{5.11}$$

respectively; see ν_i and ν_w in Fig. 5.4(a) too. The total electron and ion current lost into the walls, $I_w = \int_A^E eS_w dx$, amounts to 0.77A, whereas the discharge current is $I_d \simeq 4.83$A, and the ion beam current is $I_{i\infty} \simeq 2.9$A. An interesting result is that the discharge self-adjusts the ionization fraction at the exit of the ionization layer to a value such that ion production and recombination tend to be balanced in the acceleration region, $\nu_i \simeq \nu_w$. This implies a linear relation between the wall-loss factor $\tilde{\nu}_w$ (= 0.191, here) and the ionization inefficiency, $1 - \eta_u$:

$$\frac{\tilde{\nu}_w}{1-\eta_u} \sim \sqrt{\frac{8m_i}{\pi m_e}} \frac{v_{nA}}{v_{nE}} h_c \sigma_{iE} n_{nA}, \tag{5.12}$$

with $\sigma_i(T_e) = R_i(T_e)\sqrt{\pi m_e/8T_e}$. For the example of Fig. 5.2 the right-hand side is about one; for the case with $\nu_w = 0$ discussed in Ch. 4 we had $\eta_u \simeq 100\%$.

Characteristic values of the electron temperature in Fig. 5.2(d) are $T_{eB} \simeq 3.4$ eV, $T_{eD} \simeq 5.3$ eV, $T_{eS} \simeq 21.9$ eV, $T_{eE} \simeq 38.7$ eV, and $T_{eP} \simeq 4.4$ eV. Since we used $T_1 \simeq 39.9$eV to characterize the SEE yield of the wall material, energy losses to the walls are clearly bounding the maximum electron temperature in the chamber. The axial evolution of the SEE yield, δ_w in Fig. 5.3(b), shows that the two lateral sheaths are charge saturated ($\delta_w \simeq 0.983$) *only* in a very tiny region (less than 1mm) around the chamber exhaust. Figure 5.3(c) compares the wall energy losses, $Q_w = \nu_{we} n_e T_e A_c$, and the collisional heating, $Q_d = \nu_d n_e m_e v_{xe}^2 A$. The large energy losses for charge-saturated conditions reduce quickly the electron temperature below the CSL value to a level where they can be compensated by the Joule heating. This rough balance is kept for most of the acceleration region.

Figure 5.4(a) compares the four frequencies involved in the plasma equations. Notice that, in the region near the exhaust, the relation between ν_{we} and $\bar{\nu}_d = \nu_d m_e/m_i$ reproduces the relation between Q_w and Q_d. Figure 5.4(b) shows that the wall collisionality, with a maximum of 5×10^6 s^{-1} at the chamber exit, is clearly insufficient to justify the effective axial collisionality of the electrons, ν_e. This leaves Bohm-like diffusion as the most likely phenomenon explaining the measured electron diffusion [35].

Taking the origin of potentials at the anode in Fig. 5.2(b), potential drops in the different regions are $\phi_{AB} \simeq 4.75$ V, $\phi_{BD} \simeq 1.92$ V, $\phi_{DS} \simeq -14.3$ V, $\phi_{SE} \simeq -168.0$ V, $\phi_{EP} \simeq -126.8$ V, and the total discharge voltage is $V_d = 302.5$ V. Thus, the potential drop is of the order of T_{eB} in the sheath, negligible in the reverse flow region, and of the order of $T_{eS}/2$ in the ionization region. Indeed, the equation for the ion mechanical energy integrated across the ionization region yields

$$-e\phi_{DS} = \frac{T_{eS}}{2} + \int_D^S \nu_i m_i (v_{xi} - v_n) dx \tag{5.13}$$

so that the part of the electrostatic energy not transformed in beam energy is 3.38eV per ion. Most of the potential drop takes place in the acceleration region; in particular, the drop is

55.6% of V_d in the internal region SE and 41.9% in the external region EP. In the near plume, one should find T_{eE} of the order of $2e\phi_{EP}/5$, the difference between these two magnitudes being due mainly to heat conduction effects; in the present case we have $2e\phi_{EP}/5 \simeq$50.74eV, so that 1/4 of the external Joule heating is transmitted through conduction.

In Ch. 4 we reviewed the closed-drift, collisional model for the electron dynamics, and we evaluated the importance of the inertial effects and the electron drift energy. A summary of the pertinent electron equations is presented in Appendix A. The closed-drift, collisional model applies if conditions (4.3) and (4.6) apply. Figure 5.5 plots the inverse Hall parameter, the magnetic-to-convective time ratio, and the drift-to-thermal energy ratio. We observe that the closed-drift approximation, Eq. (4.3), is verified in the whole domain, even near the cathode, where the magnetic field is vanishing. However, the azimuthal convection and energy tends to be large in the vicinities of anode and cathode; a similar behavior was found for $\nu_w = 0$. Further studies are needed to elucidate the global relevance of these effects.

The ion temperature should be of the order of electrostatic energy not transformed into beam kinetic energy. A computation of T_i using the same equation than in Ch. 4 yields $T_{iS} \sim 1$ eV and $T_{i\infty} \simeq 3.9$ eV. This confirms that ion pressure effects can be dropped from the main set of equations modeling the discharge. The comparison of the present values of T_i with those obtained for no wall losses (we had $T_{i\infty} \simeq 0.11$ eV in Ch. 4 for a similar case) demonstrates that wall losses, by extending ionization into the acceleration region, are the main phenomena contributing to T_i.

5.4 THRUST AND EFFICIENCY

The electrostatic interaction between ions and electrons plus the magnetic forces on the electrons are the mechanisms by which plasma thrust is transferred to the solids parts of the engine. Since the magnetic field extends some distance outside the chamber and the plasma plume presents some radial divergence, neither the momentum thrust of the plasma at the chamber exhaust (point E) nor in the far plume (point ∞) evaluate correctly the thrust.

Calling

$$F_p(x) = \Big(m_i n_i v_{xi}^2 + m_i n_n v_{xn}^2 + n_e T_e\Big) A(x) \tag{5.14}$$

the total axial momentum of the plasma at a given axial section,

$$F_{mP_1P_2} = \int_{P_1}^{P_2} e n_e v_{\theta e} B A(x) dx, \tag{5.15}$$

the magnetic force on the electron flow between two channel sections (P$_1$ and P$_2$), and

$$D_{plu} = \int_E^\infty n_e T_e dA \tag{5.16}$$

the axial pressure component due to the plume lateral expansion, the thrust F satisfies the two relations

$$F = F_{pE} + F_{mE\infty} = F_{p\infty} - D_{plu}. \tag{5.17}$$

The leakage of the magnetic field outside the thruster channel yields a contribution to the thrust, $F_{mE\infty}$, which is a unique characteristic of this type of electric thrusters. Also, the balance

$$F_{p\infty} - F_{pE} = F_{mE\infty} + D_{plu} \tag{5.18}$$

shows that one part of the external acceleration of the ions comes from the plume lateral expansion and does not contribute to thrust. Thus, were the magnetic field zero outside the thruster, all external acceleration would be the reaction to plume radial expansion. For the case of Fig. 5.2 we have $F \simeq 84.9$ mN, $F_{pE} \simeq 72.5$ mN, and $F_{p\infty} \simeq 86.1$ mN, so that the external magnetic field contributes a 14.6% to the thrust whereas D_{plu} is only a 9% of the ion external acceleration.

The energy balance for the whole plasma can be expressed as

$$P_d = P_{i\infty} + P_w + P_{ion} + P_{rest},$$

where

$$P_{i\infty} = \Gamma_{i\infty} m_i v_{xi\infty}^2/2,$$

is the external ion energy flow,

$$P_w = A_c \int_A^E \nu_w \left[\frac{1}{2} m_i (v_{xi}^2 - v_{nw}^2) + \beta_e T_e\right] n_e dx \tag{5.19}$$

is the energy lost at the lateral walls,

$$P_{ion} = A_c \int_A^\infty \nu_i \alpha_i E_i n_e A dx$$

is the ionization loss, and P_{rest} groups other contributions (electron heat flow at A and ∞, anode losses, energy flow of neutrals...). For the case of Fig. 5.2, we have $P_d = I_d V_d \simeq 1461$ W, $P_{i\infty} \simeq 849$ W, $P_w \simeq 377$ W, $P_{ion} \simeq 135$ W, and $P_{rest} \simeq 100$ W. Thus, $P_{i\infty}$ amounts to a 58% of P_d, and wall losses turn to be 2.5 times larger than ionization losses. The electron energy flow represents 90% of P_{rest}.

The thrust efficiency satisfies Eqs.(4.44)-(4.45). The current utilization is related to the energy losses through

$$\eta_d \eta_e = \frac{P_{i\infty}}{P_d} = 1 - \frac{P_{ion} + P_w + P_{rest}}{P_d}. \tag{5.20}$$

Since η_e is very close to one, the inefficiency in current utilization comes from the energy losses. For the case of Fig. 5.2, one has $\eta \simeq 51.6\%$, $\eta_u \simeq 83.3\%$, $\eta_e \simeq 96.9\%$, $\eta_d \simeq 60\%$, $\eta_o \simeq 106.5\%$. For $a_w = 0$, the neutrals have a non-negligible contribution to the thrust, which explains that $\eta_o > 100\%$. These values must be compared with $\eta \simeq 81.1\%$, $\eta_u \simeq 100\%$, and $\eta_d \simeq 85.6\%$ of the similar case with $\nu_w = 0$, discussed in Ch. 4.

5.5 PARAMETER INVESTIGATION

Following Ch. 4, scaling laws involving the length of the ionization and acceleration regions, L_{AS} and L_{SP}, respectively, are

$$L_{AS} \sim \frac{\sqrt{\alpha_i E_i/m_i}}{\sqrt{\bar{\nu}_d \nu_i}}, \quad (\nu_i \gg \nu_w), \tag{5.21}$$

$$L_{SP} \sim \frac{\sqrt{2eV_d/m_i}}{\bar{\nu}_d}\frac{\eta_d}{1-\eta_d}, \tag{5.22}$$

with $\bar{\nu}_d = \nu_d m_e/m_i$ and $L_{AS} + L_{SP} = L_c + L_{cat}$.

Figures 5.6 and 5.7 show the influence of the discharge voltage and the magnetic field strength, on the thruster performance. Some plotted parameters are

$$\epsilon_w = P_w/P_d, \quad \epsilon'_w = I_w/I_d, \quad \epsilon_{ion} = P_{ion}/P_d. \tag{5.23}$$

The increase of V_d implies mainly the increase of the electron temperature, Fig. 5.6(d). This is more evident outside the channel where there are no wall losses limiting T_e. For $V_d > 300$V, there is charge-saturation of the lateral sheaths in a region near the exit, whose extension increases with $T_{eE} - T_1$. This explains that $P_w = \epsilon_w P_d$ increases faster than P_d and the decrease of η_d. The moderate increase of T_{eS} explains the decrease of L_{AS}, Eq. (5.21), and the no variation of $\epsilon_{ion} = P_{ion}/P_d$. Since η_u depends weakly on T_e [according to Eq. (5.12) and within the range of Fig. 5.6] η_u does not change with V_d.

Since Bohm-like diffusion is dominant, the magnetic field strength affects the axial diffusion through $\nu_d \sim \omega_e \alpha_{ano}^{-1} \propto B_{max}$. As B_{max} increases, L_{AS} in Eq. (5.21) decreases; then, L_{SP} increases and η_d in Eq. (5.22) increases. A larger L_{SP} means a smaller electric field, and then a lower T_{eE}.

Figure 5.8 shows the 'optimum' operation line for the parameters (V_d, B_{max}). As expected, B_{max} increases with V_d, but at a path slower than in the zero-wall case. The efficiency increases slowly with V_d. Further analysis of these results is needed.

Finally, Appendix C presents studies on other parameters of the model. These numerical results have not been analyzed carefully too.

5.6 CONCLUSIONS

The influence of different source terms of the radial interaction on the axial plasma discharge behavior has been studied. The solutions obtained with the resulting model show a reasonable agreement with trends observed in experimental data.

The SEE yield function of the ceramic insulator is crucial for the energy balance. For V_d high enough, the external heating of the electron population leads to 100% SEE in a region around the channel exit. This means a very large energy loss and a reduction of the electron temperature to a level where energy losses at the walls become comparable to the Joule heating. Wall losses and ionization losses are the phenomena reducing the current utilization.

Wall collisionality depends on the level of SEE too, but even for 100% SEE, this collisionality turns out to be much smaller than the effective collisionality dictated by experimental measurements. This leaves Bohm-like diffusion as the main phenomenon explaining the enhanced electron diffusion.

Since the discharge presents a very high beam-energy efficiency, thrust efficiency is determined mainly by the product of the current and propellant utilizations. The current efficiency is related directly to the electron energy losses, and these are dominated by losses at lateral walls. The propellant utilization is determined by the balance between volume production and wall recombination of plasma in the acceleration region.

To obtain propellant utilizations in the range 80-90%, the parameter measuring wall recombination corresponds to a value below the one corresponding to free, radial acceleration of the ions. The present understanding of the radial plasma/wall interaction [3, 2, 12] indicates that the only phenomenon able to inhibit the radial ion flux would be a strong coupling with the axial motion, in other words, the two-dimensional character of the discharge. Therefore, research on the radial model must be pursued in order to understand better the mutual coupling between the axial and radial dynamics.

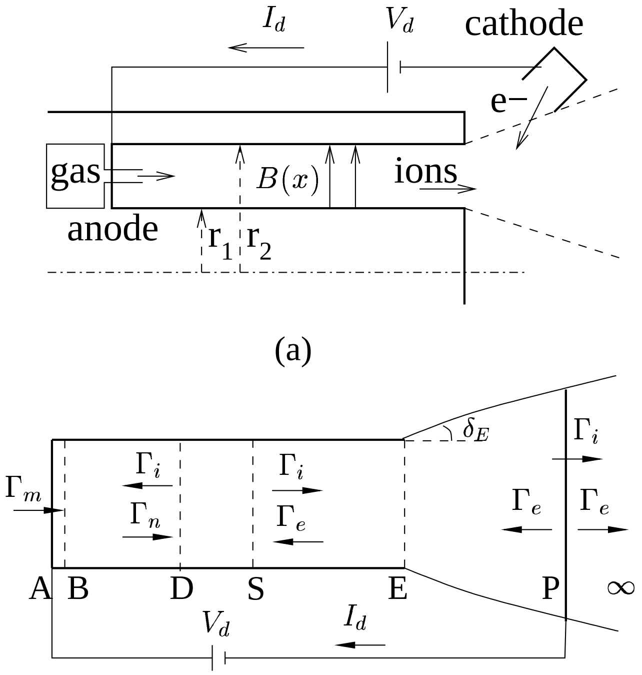
I_d
V_d
cathode
e−
gas
$B(x)$
ions
anode
r$_1$
r$_2$
δ_E
Γ_m
Γ_i
Γ_n
Γ_i
Γ_e
Γ_i
Γ_e
Γ_e
A
B
D
S
E
P
∞
V_d
I_d

(a)

(b)

Figure 5.1: Sketches of (a) the Hall thruster, and (b) the axial model. $\Gamma_\alpha = A_c n_\alpha v_{x\alpha}$, $\alpha = i, e, ...$ are axial flows of particles of the different species. The anode is at point A, the thruster exhaust at point E, and the neutralization surface at point P. Region AB is the anode sheath, BD the reverse-flow region, DS the ionization layer, SE the internal acceleration region, EP the near-plume, and P∞ the far-plume. Points B, D, and S are defined by ion velocities $v_{xiB} = -\sqrt{T_{eB}/m_i}$, $v_{xiD} = 0$, and $v_{xiS} = \sqrt{T_{eS}/m_i}$.

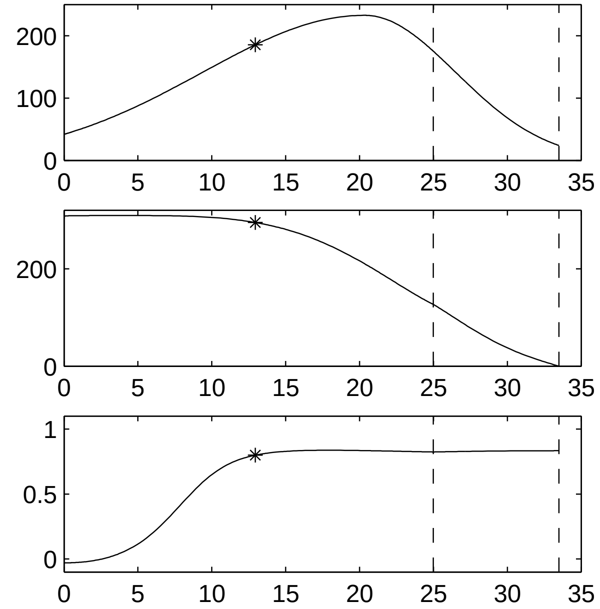
200
100
0
0 5 10 15 20 25 30 35
200
0
0 5 10 15 20 25 30 35
1
0.5
0
0 5 10 15 20 25 30 35

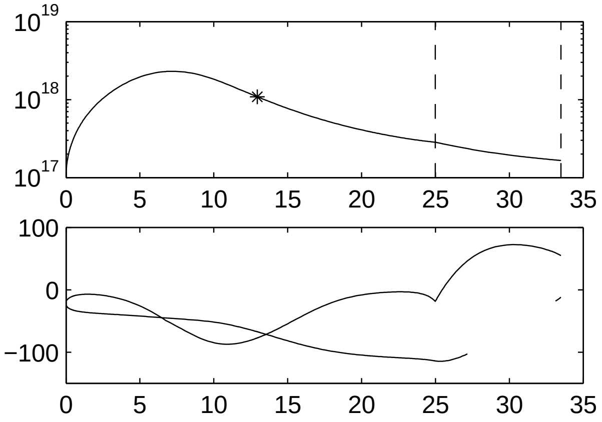
10^{19}
10^{18}
10^{17}
0 5 10 15 20 25 30 35
100
0
−100
0 5 10 15 20 25 30 35

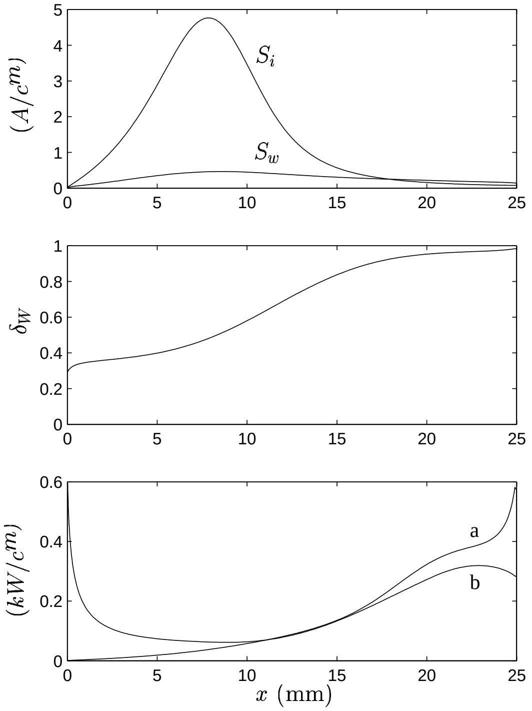

Figure 5.3: Evaluation of wall losses for the solution of Fig. 5.2. In last subplot: 'a' is Q_w and 'b' is Q_d.

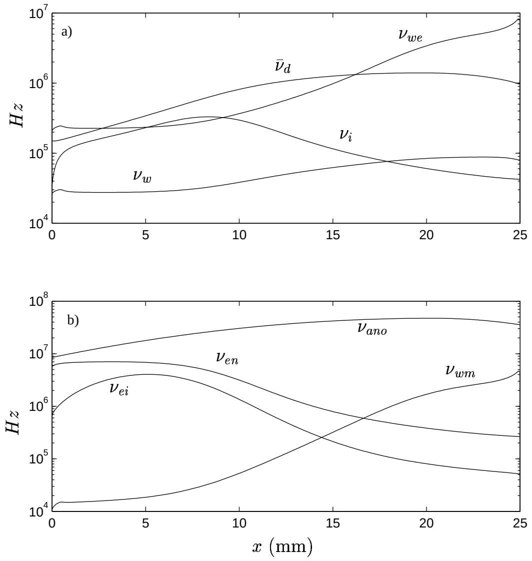

Figure 5.4: Evaluation of different collision frequencies for the case of Fig. 5.2.

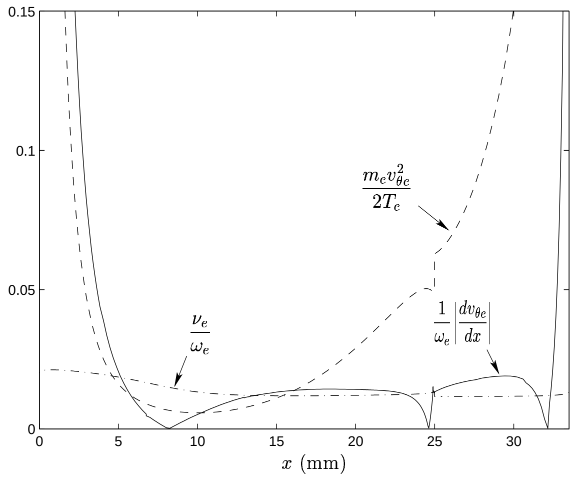

Figure 5.5: Evaluation of parameters related to electron dynamics for the case of Fig. 5.2. Maximum values of $m_e v_{\theta e}^2/2T_e$ are 11.5 at point B and 0.7 near the cathode.

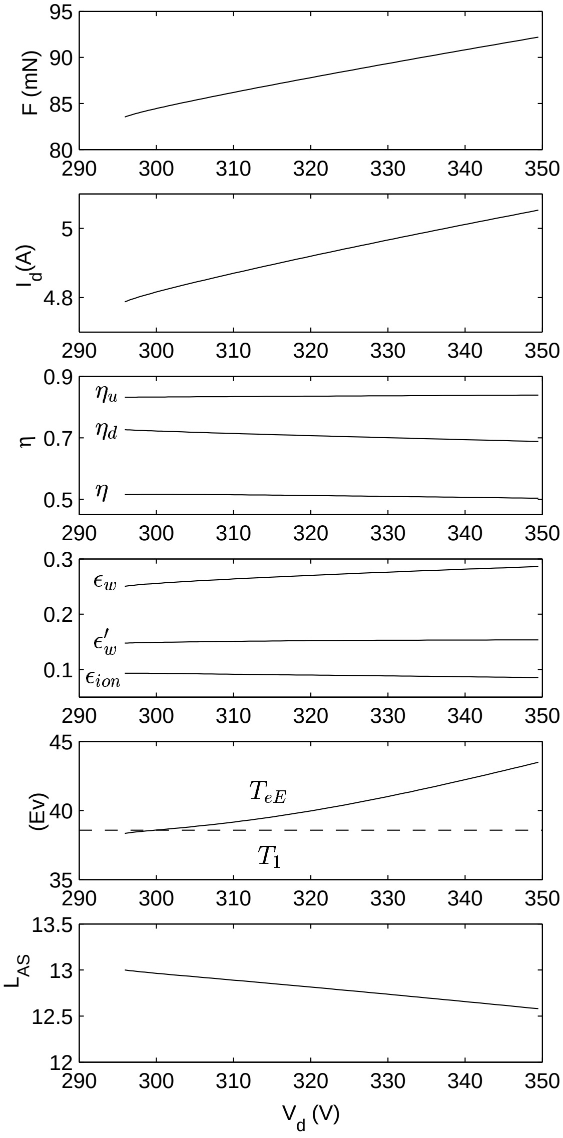

Figure 5.6: Influence of the discharge voltage on thruster performance. Rest of parameters as in Fig. 5.2.

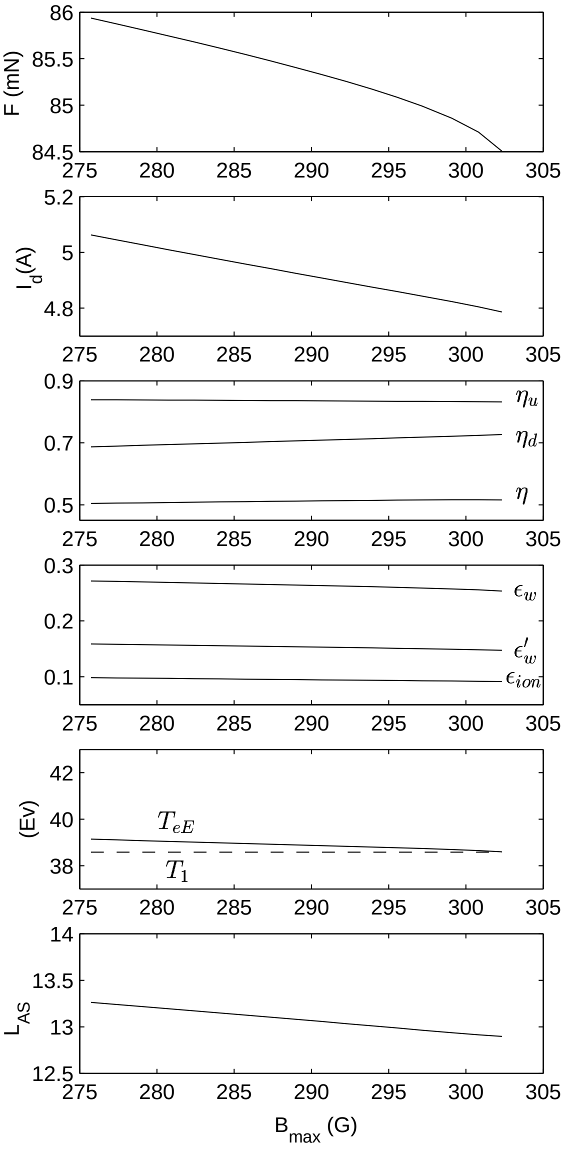

Figure 5.7: Influence of the magnetic field strength on thruster performance. Rest of parameters as in Fig. 5.2.

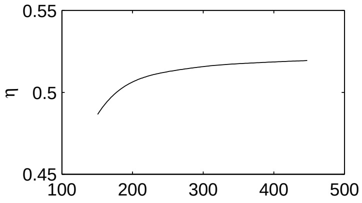
0.55
0.5
0.45
η
100
200
300
400
500

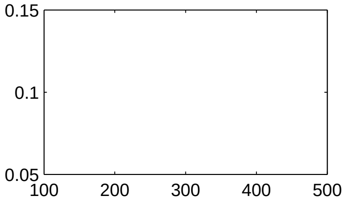
0.15
0.1
0.05
100
200
300
400
500

Chapter 6

MODEL WITH AN INTERMEDIATE ELECTRODE

6.1 INTRODUCTION

Use of internal electrodes to control the electric field and improve the thruster performance is being experimented actively [47, 27]. Intermediate electrodes control the discharge profile by (i) being biased to a given voltage and (ii) exchanging the necessary electron current with the surrounding plasma. Active electrodes can collect or emit electron currents depending on the operational conditions, while passive electrodes can only extract electrons from the plasma.

Hall thrusters without intermediate electrode but operating efficiently are known to reach ionization and beam-energy efficiencies around 90%. The thrust efficiency is penalized mainly by the current utilization, that is by the ratio between the downstream ion-current and the discharge current. Therefore, the role of an intermediate electrode should be to increase the current utilization without worsening the two other partial efficiencies. This suggests to place an electron-emitting electrode in the acceleration region of the channel to deliver a fraction of the discharge current. This chapter investigates this idea theoretically extending the axial model presented in Ch. 5 to include the interaction with the additional electrode. A detailed energy equation for electrons is employed and the parameter investigation departs from stationary solutions with high thrust efficiency already without the intermediate electrode.

Fruchtman *et al.* [29] showed recently that an electrode placed *exactly* at the sonic transition of the ion flow can enhance the thruster efficiency. Some comments are worth to be made. First, the study is restricted to electron-absorbing electrodes. Second, in the examples they present the thruster without the intermediate electrode has a low thrust efficiency, mainly because of the ionization region occupies the whole channel; by modifying the electric field, the intermediate electrode forces the ionization region to occupy only one part of the channel, improving thus the propellant and the beam-energy efficiencies. Third, the position of the ion sonic transition changes with the operational conditions and only for very particular values of the operation parameters, it will coincide with the position of the intermediate electrode. And four, they use a model with $T_e = \text{const}$ along the whole channel (and no reverse-flow region, no plume). The temperature profile and the energetic balance are known to be fundamental in determining the discharge characteristics.

6.2 MODEL FORMULATION

Figure 6.1 presents a geometrical sketch of the thruster and the axial discharge. Except for the intermediate electrode, the rest of the model is identical to the one presented in Ch. 5. The intermediate electrode [point R in Fig. 6.1], placed at $x = x_R$, is treated very similarly to the external neutralizer cathode, placed at point P in the plume. The bias voltages between anode A, electrode R, and neutralizer P are known; we call $V_d = \phi_A - \phi_P$ and $V_{int} = \phi_A - \phi_R$. On the contrary, the electrical current exchanged between the internal plasma and electrodes at R and P, $I_{int} \equiv I_{dR}$ and I_{dP}, respectively, depend on the discharge conditions and are determined as part of the solution. The total discharge current reaching the anode is

$$I_d \equiv I_{dA} = I_{dP} + I_{dR};$$

I_{int} is positive or negative depending on the electrode R emitting or absorbing electrons.

The electron currents exchanged at points R and P introduce discontinuities in some plasma magnitudes. Except for these two discontinuity surfaces (and the anode sheath) the plasma is continuous and quasineutral, and satisfies the set of equations

$$\frac{d\Gamma_i}{dx} = -\frac{d\Gamma_n}{dx} = S_i - S_w, \tag{6.1}$$

$$\begin{aligned}\frac{d}{dx}(m_i v_{xi}\Gamma_i) = -en_e A\frac{d\phi}{dx}\\ + m_i(v_n S_i - v_{xi} S_w),\end{aligned} \tag{6.2}$$

$$\frac{d}{dx}(m_i v_n \Gamma_n) = m_i(v_{nw} S_w - v_n S_i), \tag{6.3}$$

$$\frac{d\Gamma_e}{dx} = S_i - S_w + S_P + S_R \tag{6.4}$$

$$0 = -\frac{d}{dx}n_e T_e + en_e\frac{d\phi}{dx} - \nu_d m_e n_e v_{xe}, \tag{6.5}$$

$$\begin{aligned}\frac{d}{dx}\left(\frac{5}{2}T_e\Gamma_e + q_{xe}A\right) = en_e v_{xe} A\frac{d\phi}{dx} - \alpha_i E_i S_i\\ - \beta_e T_e S_w + \frac{5}{2}T_P S_P + \frac{5}{2}T_R S_R,\end{aligned} \tag{6.6}$$

$$\frac{dT_e}{dx} = -\frac{2m_e\nu_d}{5n_e T_e}q_{xe}, \tag{6.7}$$

Here, $\nu_d = \omega_e^2/\nu_e$ and the four source terms are

$$\begin{aligned} S_i &= An_e\nu_i, & S_P &= \delta(x - x_P)I_{dP}/e,\\ S_w &= An_e\nu_w, & S_R &= \delta(x - x_R)I_{dR}/e,\end{aligned} \tag{6.8}$$

$\delta(x)$ the Dirac function, and T_R and T_P the temperatures of the electrons emitted at electrodes R and P, respectively. See previous chapters for the definitions of the rest of symbols and variables. Notice that only the particle and energy equations of the electrons are affected by the exchange of current. On the contrary, for a collisional electron motion, ν_d and the Ohm's law are unaffected.

To integrate the equations across point R the jump conditions there must be defined. Clearly, Eq. (6.4) states that the jump in the electron flow is

$$\Gamma_{eR}^{+} - \Gamma_{eR}^{-} = I_{dR}/e. \tag{6.9}$$

The next issue is whether a discontinuity in the plasma potential takes place at point R. This would mean the presence of a double layer (i.e. a double Debye sheath with total electrical charge equal to zero). Although a detailed study of the Poisson equation has not been completed, the analysis of the plasma conditions suggests that a double layer cannot develop there. Then, we have $\phi_R^+ = \phi_R^-$, and the ion equations yield $v_{xiR}^+ = v_{xiR}^-$ and $n_{eR}^+ = n_{eR}^-$. As a consequence, the jump in electron current implies a jump in electron velocity:

$$v_{xeR}^{+} - v_{xeR}^{-} = I_{dR}/en_{eR}. \tag{6.10}$$

Finally, using Eqs. (6.6) and (6.9), the jump of the heat conduction flux is

$$(q_{xeR}^{+} - q_{xeR}^{-})A_c = \frac{5}{2}(T_R - T_{eR})\frac{I_{dR}}{e}. \tag{6.11}$$

Here, T_{eR} is the temperature at point R of the (unique) electron population, whereas T_R is the temperature of the electrons exchanged between the plasma and the electrode. Thus, one has $T_R = T_{eR}$ for an absorbing electrode, whereas T_R is given for an emissive electrode (we will take $T_R \sim T_P$). Notice that at the emissive neutralizer P we take $T_{eP} = T_P$ since all electrons there come from the cathode.

The rest of boundary conditions needed to integrate the plasma equations are identical to the case without electrode R. The integration procedure depends on the position of the ion sonic point S (defined by $v_{xiS} = \sqrt{T_{eS}/m_i}$) relative to the electrode R. That position is determined as part of the solution and marks the beginning of the acceleration region. In this chapter we solve cases where point S is *upstream* of the electrode R. On the one hand, they allow us to use the same integration scheme than in the previous chapter. On the other hand and as we commented above, these cases should correspond to the appropriate configuration to maximize the thruster efficiency.

We define the relative flows of the different species as

$$\eta_\alpha(x) = \Gamma_\alpha(x)/\Gamma_m. \tag{6.12}$$

To compare the different cases we define the thrust efficiency as

$$\eta = \frac{F^2}{2\dot{m}_A P_d} = \eta_e \eta_u \eta_d \eta_o \beta_{int}, \tag{6.13}$$

with F the thrust, defined as in Ch. 5,

$$P_d = I_{dP}V_d + I_{dR}V_{int} \equiv I_d V_d - I_{int}(V_d - V_{int}) \tag{6.14}$$

the power spent in the discharge,

$$\beta_{int} = I_d V_d / P_d \tag{6.15}$$

the power gain due to the intermediate electrode, and

$$\eta_u = \frac{m_i \Gamma_{i\infty}}{\dot{m}_A}, \qquad \eta_d = \frac{e\Gamma_{i\infty}}{I_d},$$
$$\eta_e = \frac{m_i v_{xi\infty}^2}{2eV_d}, \qquad \eta_o = \frac{F^2}{(\Gamma_i m_i v_{xi})^2_\infty}, \tag{6.16}$$

the propellant utilization, the current utilization, the beam-energy efficiency, the other-effects efficiency (plume radial expansion, thrust of neutrals, anode sheath,...), respectively.

6.3 STRUCTURE OF THE DISCHARGE

Figure 6.2 shows a solution for a conventional mid-power thruster without intermediate electrode and for near-optimum operational conditions. Then, an intermediate electrode is placed at $x_R = 18$ mm, and solutions are sought departing from the one shown in Fig. 6.2 (which has $I_{int} = 0$ and $V_{int} = \phi_A - \phi_R = 52$ V). Figure 6.3 shows the solution for $V_{int} = 73.5$ V, when the electrode R is emitting $I_{int} = 0.5$ A. Comparing the thruster performances for the cases of Figs. 6.2 and 6.3, we find a relative gain of 3% in discharge power and of 5% in efficiency, when a 10% of the discharge current is emitted by electrode R. Thrust and propellant utilization do not change practically.

Notice in Fig. 6.3 that only Γ_e and dT_e/dx are discontinuous at R. By decreasing ϕ_R we are forcing lower potentials and electric fields in the plume; the electron current between R and P decreases with I_{int} too. The consequence is a smaller electron temperature at the thruster exhaust with the subsequent reduction of the wall energy losses. We showed in Ch. 5 that these losses are related directly to the current inefficiency, $1 - I_{i\infty}/I_{dP}$; from Fig. 6.2 to Fig. 6.3, $I_{i\infty}/I_{dP}$ has increased a 5%. This increment explains the improvement of η, since the rest of partial efficiencies change very little; in particular, the variation of η_u is small because of the electrode R is downstream of the ionization region.

6.4 PARAMETER INVESTIGATION

Steady solutions with a reverse-flow region exist only in the narrow band $1\% < |\eta_{iB}| < 15\%$, roughly(Ch. 5). Figures 6.2 and 6.3 show the increase of the reverse flow with I_{int}. That narrow parameter band would represent 'optimum' points of operation, as we discussed in Ch. 5. To keep the thruster operating in that band, we look for pairs of control parameters yielding solutions which keep $\eta_{iB} \sim$ const within that range. Figure 6.4 shows the optimum operational points of the pair (V_{int}, B_{max}), $-\eta_{iB} = 2.5\%$, and the rest of parameters as in Fig. 6.2; notice that I_{int}, although represented in the abscissa, is an output parameter. Both absorbing ($I_{int} < 0$) and emitting ($I_{int} > 0$) electrodes have been considered; $I_{int} = 0$ correspond to the case of Fig. 6.2. The thruster efficiency increases with the electron emission at R, provided that magnetic field is increased too; η goes from 51.5% to 60%, for I_{int} changing from 0 to 1.3 A and B_{max} from 233 gauss to 362 gauss. Since η/β_{int} and the total discharge current I_{dA} vary very little with I_{int}, the gain in efficiency comes directly from the gain in discharge power, β_{int}.

Let us try to understand now the existence of a maximum of η (for $I_{int} \sim 1.3$ A). The lower, ideal limit for the electron current delivered by the cathode is $I_{dP} = I_{iP}$. Since I_{dA}

and I_{iP} remain almost constant with I_{int}, the difference $I_{dA} - I_{iP}$ yields the maximum value of the intermediate current. Figure 6.4 shows that the derivative $-\partial V_{int}/\partial I_{int}$ increases as I_{int} approaches that maximum. The consequence is that $I_{int}(V_d - V_{int})$ in Eq.(6.14), and, therefore, β_{int} and η reach a maximum.

For the parameter evolution of Fig. 6.4, point S moves downstream with I_{int} increasing; for $I_{int} = 1.2$ A it is placed at $x_S \sim 10$ mm. According to the law

$$x_S \equiv L_{AS} \sim \frac{1}{\omega_e}\sqrt{\frac{\alpha_i E_i}{m_e}\frac{\nu_e}{\nu_i}} \tag{6.17}$$

the displacement of point S is due to the change of B_{max}.

Figure 6.4 shows that the case $I_{int} < 0$, corresponding to an electron-absorbing electrode, is clearly disadvantageous, at least when the thruster is operating efficiently without intermediate electrode. As I_{int} becomes more negative, point S approaches point R. The situation considered by Fruchtman *et al.*, with the sonic point just at the electrode R is reached for a particular value of the intermediate current around -1.2 A; the thrust efficiency then is 43% only.

Figure 6.5 shows the structure of the discharge for the case of maximum efficiency in Fig. 6.4. Here, the phenomena we observed in Fig. 6.3, are more pronounced. The most evident one is the large modification of the temperature profile. The low Joule heating between R and S yield low electron temperatures there. For this case, lateral sheaths are far from being charge-saturated. Indeed, the increment of the electric field between R and S, yield a large Joule heating which produces the intermediate maximum of T_e, but this one is still below the charge-saturation limit.

6.5 CONCLUSIONS

A previous model of the plasma discharge has been extended to include the exchange of electrical current with an internal electrode biased to a given voltage. The electrode can either emit or absorb electrons. Only configurations with the electrode placed in the plasma acceleration region have been treated but these are thought to be the most interesting ones in practice.

It has been demonstrated that the efficiency of a mid-power thruster can be increased from about 50% to 60% with 1/4 of the electron current emitted from the intermediate electrode. The increase in efficiency is the consequence of a reduction in discharge power, for given discharge voltage and mass flow. When the electrode potential is decreased, the plasma increases the exchange of the intermediate current, whereas the total discharge current, the thrust, and the propellant utilization are kept almost constant. The consequences are lower electron heating, lower wall losses, and larger utilization of the neutralizer current.

A parameter investigation on the pair magnetic-field-strength/intermediate-emitted-current concludes that B_{max} must be increased with I_{int} to follow points of stationary, efficient operation. It also demonstrates that there exist an intermediate current which gives maximum efficiency. This maximum is related to the fact that the total discharge current varies weakly with the intermediate current, and this one is upper bounded by the cathode current required to neutralize the ion flow in the plume. Finally, it has been shown that an absorbing electrode placed in the acceleration region has only negative effects on the thruster performance, when the thruster is operated correctly. Further optimization studies are needed.

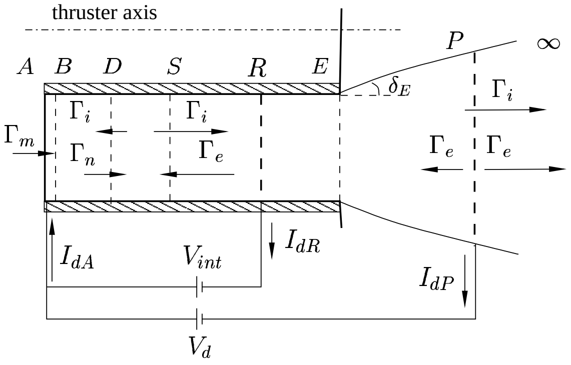
thruster axis
A
B
D
S
R
E
P
∞
δ_E
Γ_m
Γ_i
Γ_i
Γ_n
Γ_e
Γ_i
Γ_e
Γ_e
I_{dA}
V_{int}
I_{dR}
I_{dP}
V_d

Figure 6.1: Sketches of the axial model. The anode is at point A, the thruster exhaust at point E, the neutralization surface at point P, and the intermediate electrode at point R. The ionization region will correspond to the region between point D of zero velocity and the sonic point S. Region AB is the anode sheath. The voltages V_d and V_{int} are known, whereas I_{dR} and I_{dP} are determined by the thruster/plasma response. $\Gamma_\alpha = A_c n_\alpha v_{x\alpha}$, $\alpha = i, e, ...$ are axial flows of particles of the different species.

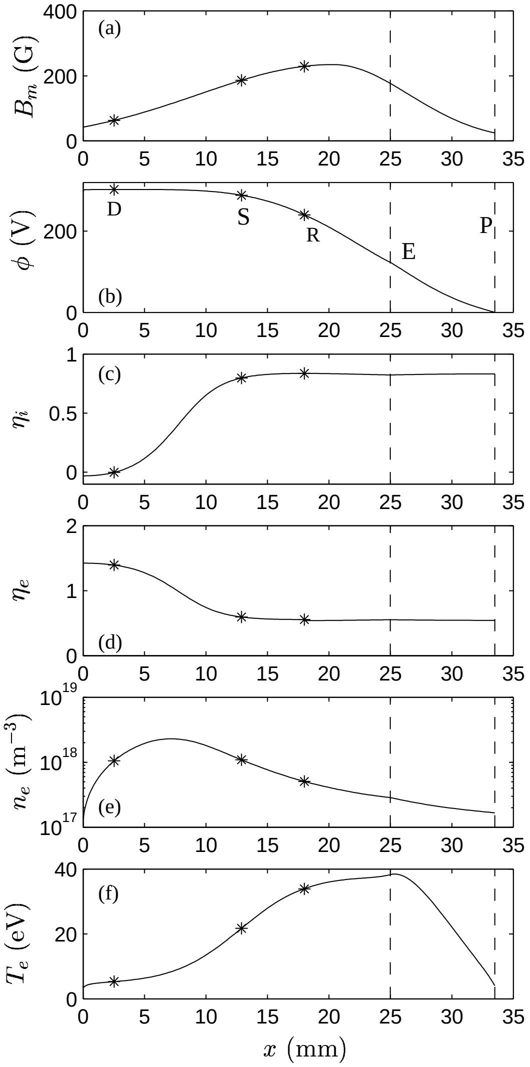

Figure 6.2: Axial structure of the plasma discharge. Input parameters: $L_c = 25$mm, $L_{cat} = 8.5$mm, $A_c = 40\text{cm}^2$, $V_d = 296$V, $\dot{m} = 4.78$mg/s, $T_{eP} = 4.4$eV, $16\alpha_{ano} \sim 0.1986$, $T_1 \simeq 39.93$eV, $\tilde{\nu}_w \simeq 0.191$, $a_w = 0$. The intermediate electrode is placed at $x_R = 18$ mm and is biased at a voltage $V_{int} = \Phi_A - \phi_R = 52$ V.

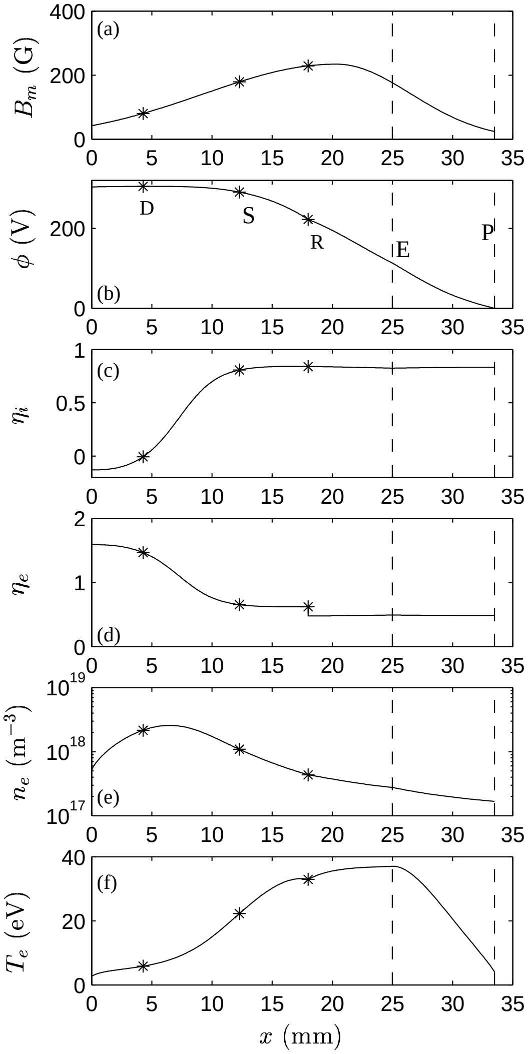

Figure 6.3: Plasma response with an intermediate electrode at $x_R = 18$ mm, biased to $V_{int} = \Phi_A - \phi_R = 73.5$ V, and emitting $I_{int} = 0.5$ A. The rest of parameters are as in Fig. 6.2. (where $\phi_A - \phi_R = 52$ V).

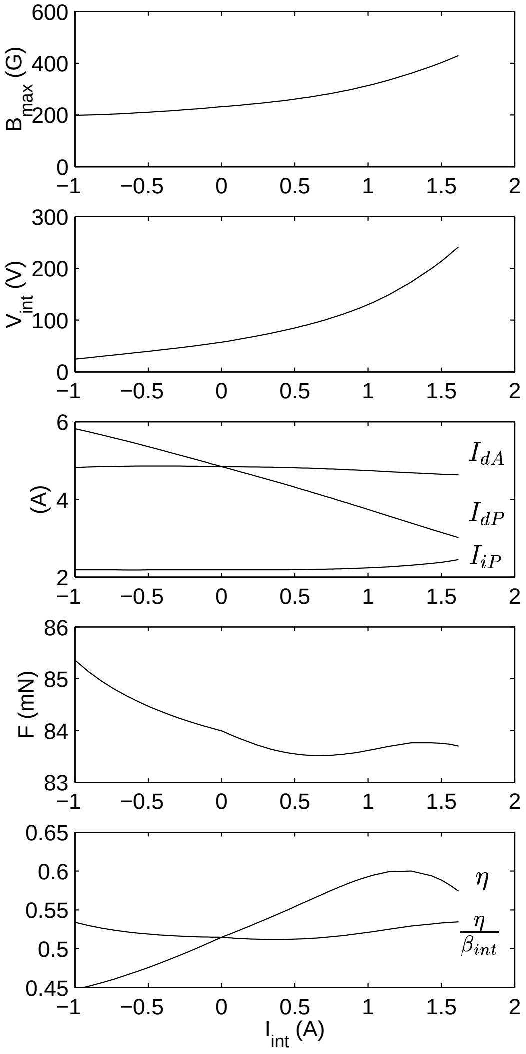

Figure 6.4: Optimum operation: Values of V_{int} and B_{max} keeping $-\eta_{iB}$ = const = 2.5% and the electrode at $x_R = 18$ mm. The rest of parameters are as in Fig. 6.2. $I_{int} < 0$ correspond to an absorbing electrode, $I_{int} = 0$ to no electrode, and $I_{int} > 0$ to an emitting electrode.

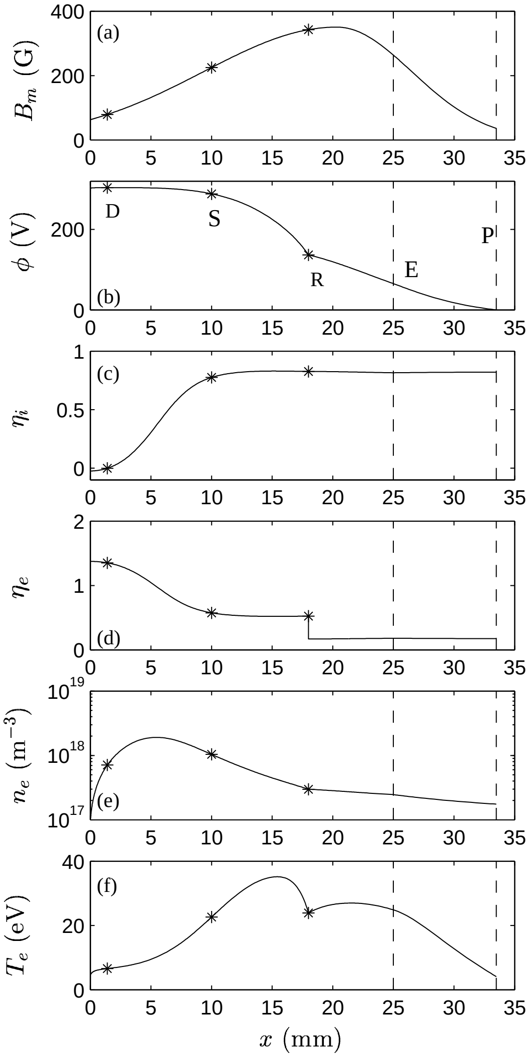

Figure 6.5: Plasma response with an intermediate electrode for the point with $I_{int} = 1.3$ A in Fig. 6.4.

Appendix A

DERIVATION OF THE RADIAL PRESHEATH MODEL

In a Hall thruster, ions are created by electron impact of a neutral gas, most of them are singly-charged, and magnetic effects on them can be ignored. From the whole axisymmetric model, the equations relevant to study radial ion dynamics are

$$\frac{1}{r}\frac{\partial}{\partial r} r n_i v_{ri} + \frac{\partial}{\partial x}(n_i v_{xi}) = \nu_i n_i, \tag{A.1}$$

$$m_i n_i \Big(v_{ri}\frac{\partial v_{ri}}{\partial r} + v_{xi}\frac{\partial v_{ri}}{\partial x}\Big) = -\frac{\partial}{\partial r}(n_i T_i) - e n_i \frac{\partial \phi}{\partial r} - \nu_i m_i n_i v_{ri}, \tag{A.2}$$

$$\begin{aligned}\frac{1}{r}\frac{\partial}{\partial r}(r\frac{3}{2}T_i n_i v_{ri}) + \frac{\partial}{\partial x}(\frac{3}{2}T_i n_i v_{xi}) + T_i n_i\Big(\frac{1}{r}\frac{\partial}{\partial r}(r v_{ri}) + \frac{\partial v_{xi}}{\partial x}\Big)&\\ = \nu_i n_i\Big(\frac{1}{2}m_i(v_{ri}^2 + v_{xi}^2) + \frac{3}{2}T_n\Big),&\end{aligned} \tag{A.3}$$

Here ν_i is the ionization frequency, T_n is the temperature of the neutral gas, and the rest of symbols are conventional. Ion heat conduction is difficult to estimate; here it has been disregarded, based in the conclusions of Scheuer and Emmert[50]. In Hall thrusters, T_n is negligible compared to the plasma temperature T_e; here, it is kept to compare our model with previous ones.

From the preceding equations, in each axial section of the chamber, ion radial dynamics verify

$$\frac{1}{r}\frac{\partial}{\partial r} r n_i v_{ri} = \nu_w n_i, \tag{A.4}$$

$$m_i n_i v_{ri}\frac{\partial v_{ri}}{\partial r} = -\frac{\partial}{\partial r}(n_i T_i) - e n_i \frac{\partial \phi}{\partial r} - \nu_r m_i n_i v_{ri}, \tag{A.5}$$

$$\frac{1}{r}\frac{\partial}{\partial r}(r\frac{3}{2}T_i n_i v_{ri}) + \frac{T_i n_i}{r}\frac{\partial}{\partial r}(r v_{ri}) = \nu_i \frac{1}{2} m_i n_i v_{ri}^2 + \nu_t n_i T_i, \tag{A.6}$$

where axial dynamics are included through three frequency terms,

$$\begin{aligned}\nu_w &\simeq \nu_i - \frac{1}{n_i}\frac{\partial}{\partial x}(n_i v_{xi}),\\ \nu_r &\simeq \nu_i + \frac{v_{xi}}{v_{ri}}\frac{\partial v_{ri}}{\partial x},\\ \nu_t &\simeq \frac{\nu_i}{T_i}\Big(\frac{1}{2}m_i v_{xi}^2 + \frac{3}{2}T_n\Big) - \frac{5}{2}\frac{\partial v_{xi}}{\partial x} - \frac{3v_{xi}}{2n_iT_i}\frac{\partial n_iT_i}{\partial x}.\end{aligned} \tag{A.7}$$

These effective frequencies are unknown functions of x and r. The 1D radial model is based in taking $\nu_j = \nu_j(r), (j = i, w, r, t)$, as known functions in a generic axial position x. [Effective frequencies for charge-exchange, electron-neutral, and electron-ion collisions have been omitted in Eq. (A.2), based in the assumptions $\nu_{cx} \leq O(\nu_w)$ and $\nu_{en}, \nu_{ei} \ll \nu_w m_i/m_e$, holding generally inside a Hall thruster. It would be no problem to include them in the definition of ν_r.]

It is worth noting that the equations defining ν_w and ν_t, Eq. (A.7), also correspond to the axial equations of continuity and energy for the 'average' (i.e. r-independent) plasma state in an axial cross-section,

$$\frac{\partial}{\partial x}(n_i v_{xi}) = (\nu_i - \nu_w)n_i, \tag{A.8}$$

$$\frac{\partial}{\partial x}\Big(\frac{3}{2}n_iT_iv_{xi}\Big) + n_iT_i\frac{\partial v_{xi}}{\partial x} = \nu_i\Big(\frac{1}{2}m_in_iv_{xi}^2 + \frac{3}{2}T_n\Big) - \nu_t n_i T_i. \tag{A.9}$$

Since the losses of internal energy at lateral walls per particle are $5T_i/2$, ν_t should be equal to $5\nu_w/2$, which coincides with the result found in Sec. II, Eq. (1.12), from the analysis of the radial energy equation.

In a Hall thruster, electrons diffuse axially in a quasi-closed drift induced by a radial magnetic field, whereas the remain confined radially by the self-induced electric potential. Therefore, we can assume that in the radial direction electrons are in Maxwell-Boltzmann equilibrium at a temperature T_e,

$$0 \simeq -T_e\frac{\partial n_e}{\partial r} + en_e\frac{\partial \phi}{\partial r}. \tag{A.10}$$

The Poisson equation for the axisymmetric problem is

$$\frac{\partial^2\phi}{\partial x^2} + \frac{1}{r}\frac{\partial}{\partial r}\Big(r\frac{\partial\phi}{\partial r}\Big) = \frac{e}{\epsilon_0}(n_e - n_i). \tag{A.11}$$

Since the Debye length is much smaller than both the thruster dimensions and the relevant mean free paths, the zero Debye-length limit can be adopted to solve the problem. This means to consider the plasma quasineutral ($n_e \simeq n_i$) everywhere except in thin space-charge sheaths around the chamber walls, where a 1D form of Eq. (A.11) can be used.

Appendix B

ON THE PRESHEATH/SHEATH TRANSITION

The quasineutral equations (1.1)-(1.5) show that it is impossible to have $|v_{ri}| > c_s$ in the presheath. But these equations by themselves do not forbid a presheath/sheath transition with $|v_{ri}| < c_s$, as Keidar *et al.*[37] propose. To settle that $|v_{ri}| = c_s$ is the only possible transition condition is necessary to include the Poisson equation in the analysis.

Let us consider that the quasineutral solution extends until certain point Q with $v_{riQ} \leq c_{sQ}$ and $n_{eQ} = n_{iQ}$. The possibility of a transition to a non-neutral sheath depends on the local behavior of the plasma and Poisson equations around point Q. Taking into account that the sheath is a thin region tied to the wall, radial gradients would dominate within it and in the transition region, even for a plasma flowing axially. Then, the Poisson equation (A.11) reduces there to the planar form

$$\frac{\epsilon_0}{e}\frac{\partial^2 \phi}{\partial r^2} = n_e(\phi) - n_i(\phi, r), \tag{B.1}$$

where the two density functions come from Eqs. (1.1)-(1.5). Calling $\Delta\phi = \phi - \phi_Q$, $\Delta r = r - r_Q$, and $\lambda_{dQ} = \sqrt{\epsilon_0 T_e / e^2 n_{eQ}}$, the local expansion of Eq. (B.1) around point Q is

$$\lambda_{dQ}^2 \frac{\partial^2 \Delta\phi}{\partial \Delta r^2} + a\Delta\phi + b\Delta\phi^2 \simeq c\Delta r, \tag{B.2}$$

with

$$a = \frac{T_e}{m_i v_{riQ}^2 - \frac{5}{3}T_{iQ}} - 1, \qquad b = \frac{T_e}{2en_{iQ}}\Big(\frac{\partial^2 n_i}{\partial \phi^2} - \frac{\partial^2 n_e}{\partial \phi^2}\Big)\Big|_Q, \qquad c = -\frac{T_e}{en_{iQ}}\frac{\partial n_i}{\partial r}\Big|_Q. \tag{B.3}$$

Equation (B.2) shows that for $a > 0$, $\Delta\phi(\Delta r)$ can present only spatial oscillations around the quasineutral solution, $a\Delta\phi \simeq c\Delta r$. Therefore, a transition to a non-neutral sheath is only possible for $a \leq 0$.

For cold ions ($T_{iQ} = 0$), $a \leq 0$ is equivalent to $v_{riQ} \geq c_{sQ}$. For warm ions, one has $a \leq 0$ for $v_{riQ} \geq c_{sQ}$ and for $v_{riQ} < \sqrt{5T_{iQ}/3m_i}$, but in this last case the sheath equations would not admit to have $v_{ri} > \sqrt{5T_{iQ}/3m_i}$ anywhere and wall conditions could not be fulfilled [at least for $T_{iQ}/T_e \leq O(1)$]. Therefore, a transition to a sheath structure is only possible for $|v_{ri}| \geq c_s$. To conclude, since $v_{riQ} > c_{sQ}$ cannot be reached by the quasineutral solution, the sonic Bohm condition, $v_{riQ} = c_{sQ}$, (i.e., $a = 0$) is the *only possible* transition condition.

Once the transition point is uniquely determined, the solution of Eq. (B.2) with $a = 0$ yields the transition behavior of the electric potential and field. This problem was solved already by Tonks and Langmuir (see Fig. 6 in Ref. [54]) and with some more detail and generality by Lam[48]; both works use kinetic models but the deduction is the same for a macroscopic approach. The solution of the transition region shows that (i) the electric field increases *continuously and smoothly* from $d\phi/dr \sim T_e/eh$ at the presheath side to $d\phi/dr \sim T_e/e\lambda_d$ at the sheath side and (ii)

$$\left.\frac{d(e\phi/T_e)}{d\zeta}\right|_Q = 0 \tag{B.4}$$

is the correct asymptotic boundary condition at the sheath edge in the sheath distinguished scale, $\zeta = (r - r_W)/\lambda_d$.

In the presence of a magnetic field oblique to the wall, another situation where Beilis and Keidar proposed a subsonic ion flow at the sheath edge[14], Ref. [1] demonstrated that the sonic Bohm condition continues to be the correct presheath/sheath transition.

Appendix C

PARAMETER INVESTIGATION ON THE AXIAL MODEL

Here we present graphics showing the influence on the plasma and thruster performances of several of the parameters of the axial model presented in Chapter 5. In all figures the base case is that of Fig. 5.2 and only the parameters shown in the abcissae is varied. Chapter 5 already showed the influence of V_d and B_{max}. The rest of cases is presented here because they have not been analyzed in detail yet. Also, the reader must be aware that in several figure labels, the name of certain magnitudes is not the same we used in the main text.

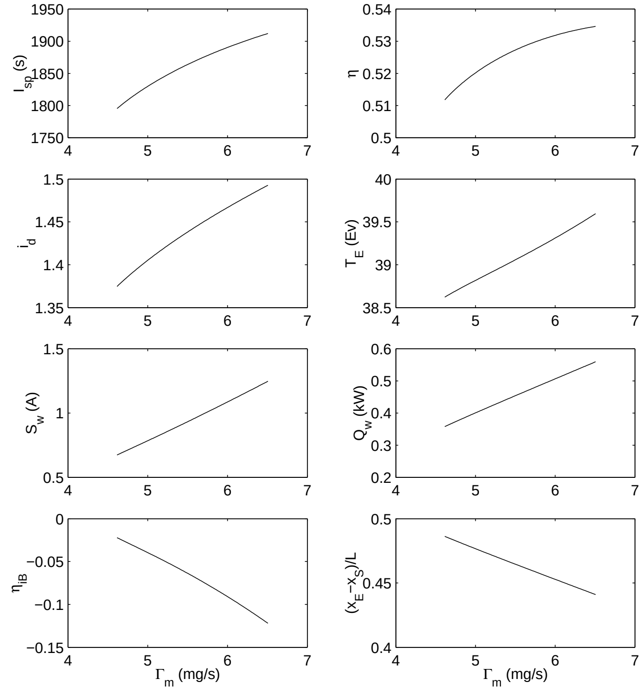

Figure C.1: Influence of the anode mass flow; Γ_m is actually $\dot{m} = m_i \Gamma_m$.

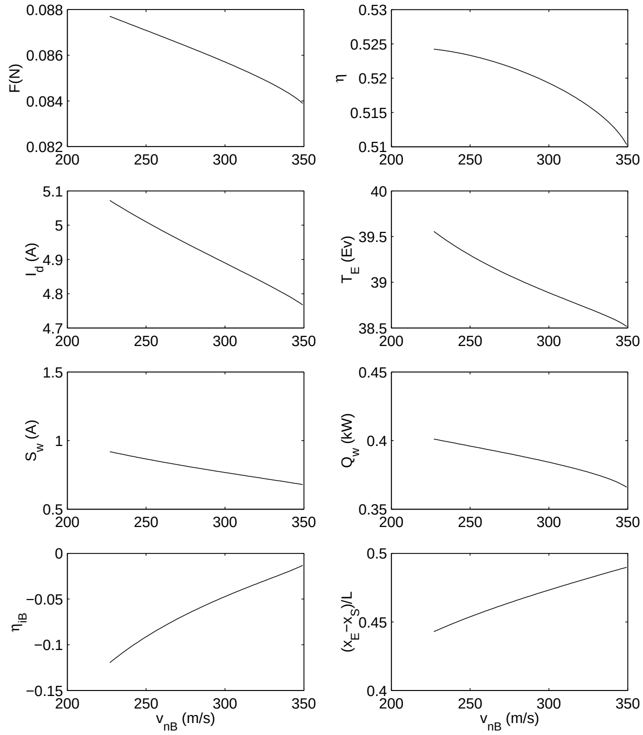

Figure C.2: Influence of the velocity of neutrals at the anode.

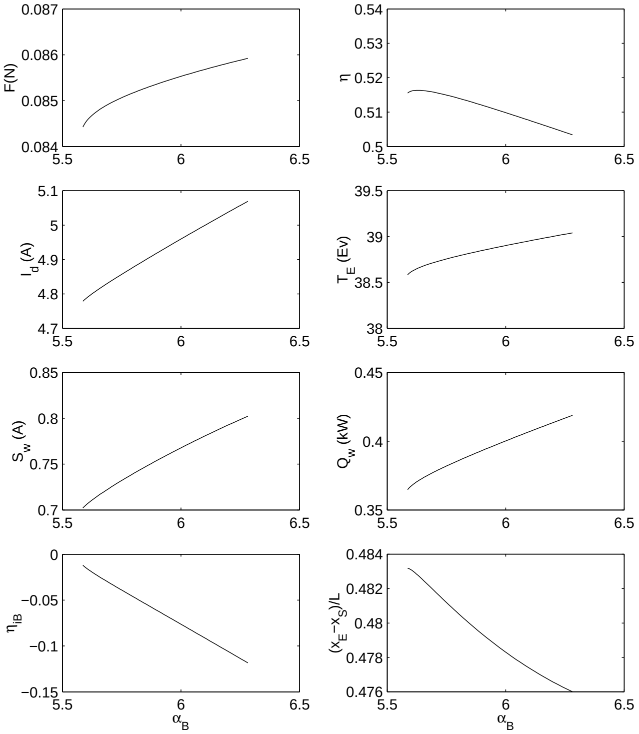

Figure C.3: Influence of the anomalous diffusion parameter; α_B is α_{ano} in the main text.

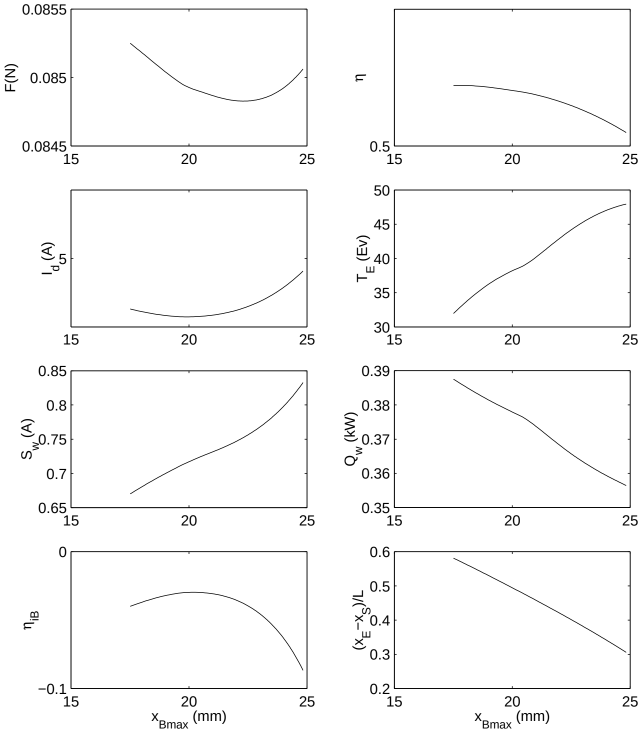

Figure C.4: Influence of the position of B_{max}.

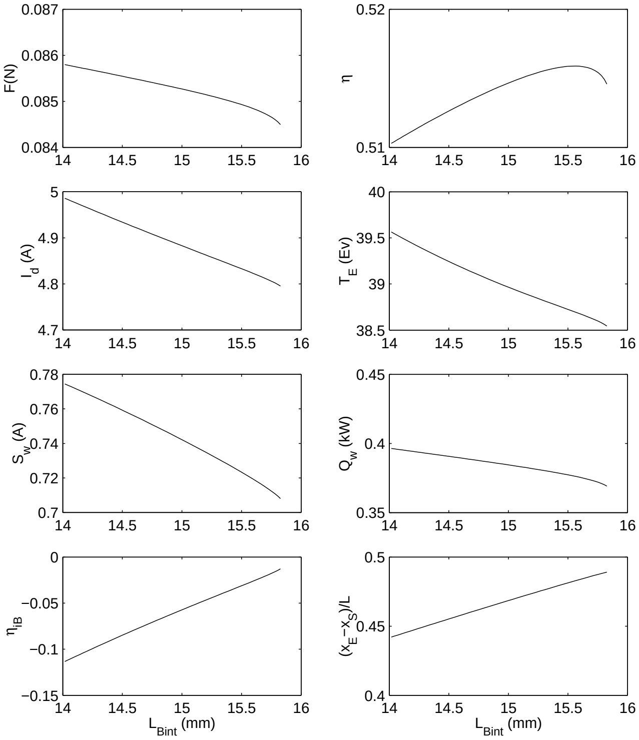

Figure C.5: Influence of the slope of the internal B-profile.

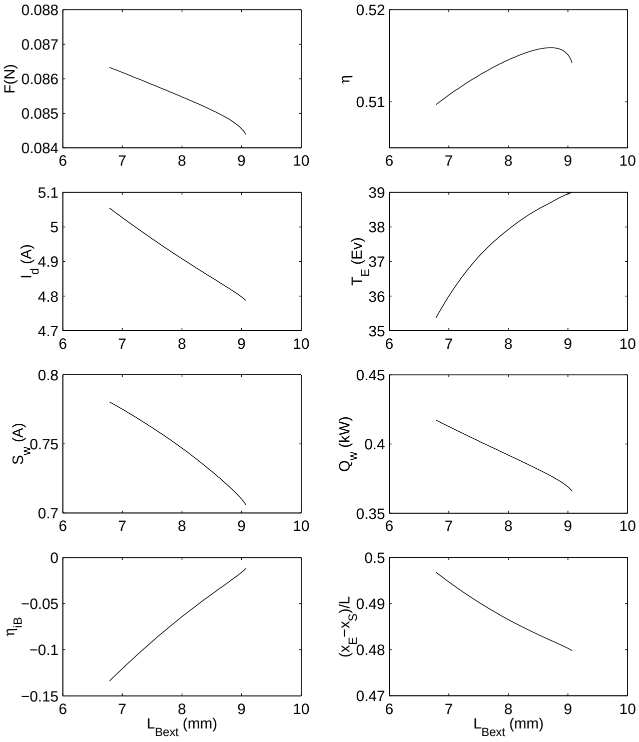

Figure C.6: Influence of the slope of the external B-profile.

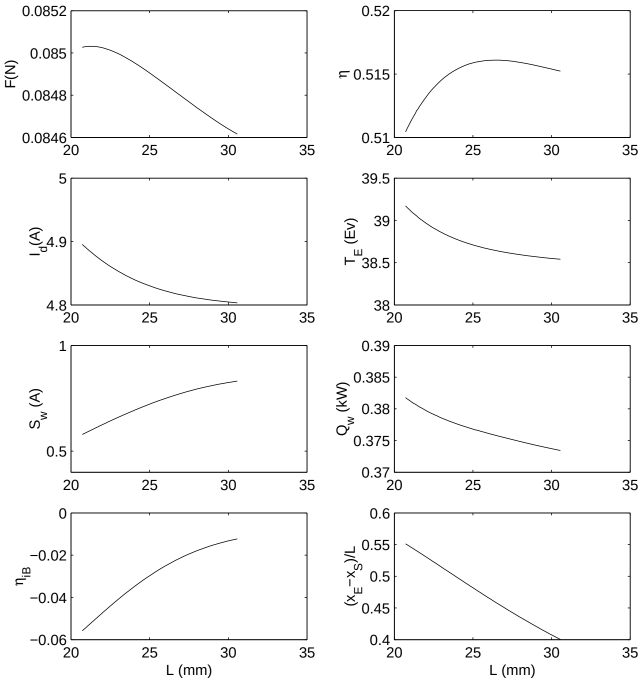

Figure C.7: Influence of the channel length: the position of the anode is changed, the B-field profile remains constant with respect to the channel exhaust.

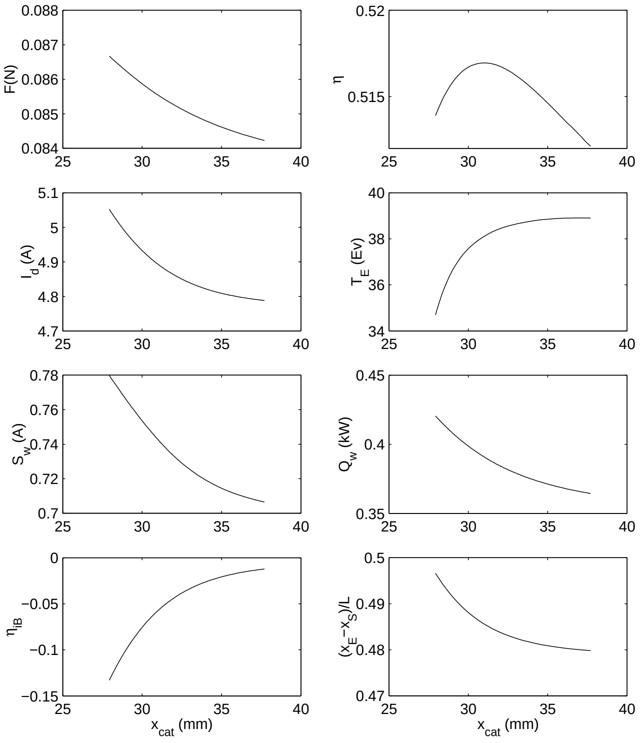

Figure C.8: Influence of the position of the neutralization surface; x_{cat} is L_{EP} in the main text.

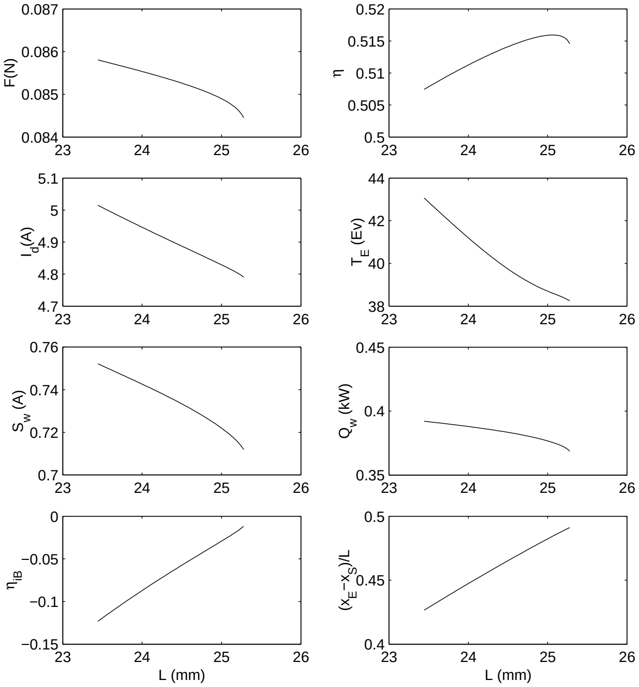

Figure C.9: Influence of the axial length scale: all axial magnitudes (L_{cat}, x_{Bmax}, L_{Bint}, and L_{Bext}) are scaled proportional to L, but radial magnitudes are not modified.

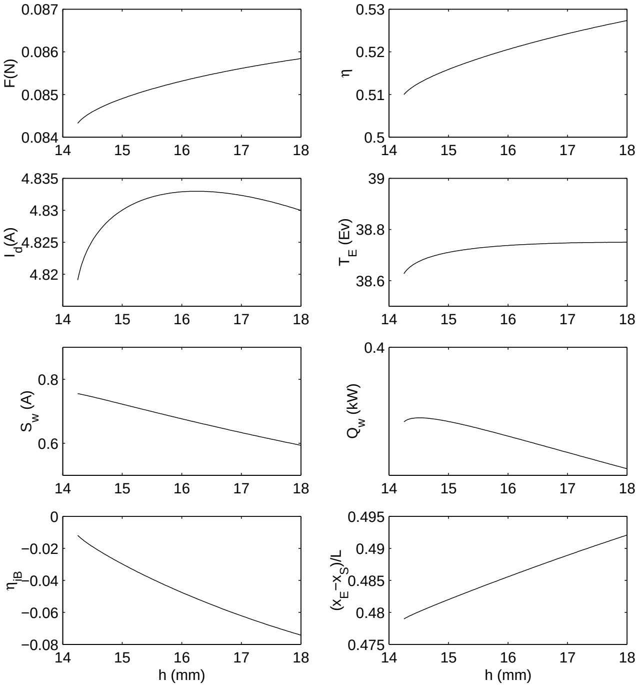

Figure C.10: Influence of the channel width; h is h_c in the main text.

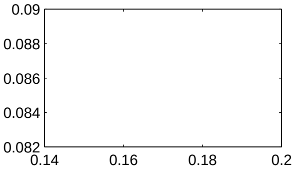

0.09
0.088
0.086
0.084
0.082
0.14
0.16
0.18
0.2

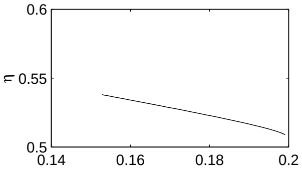

η
0.6
0.55
0.5
0.14
0.16
0.18
0.2

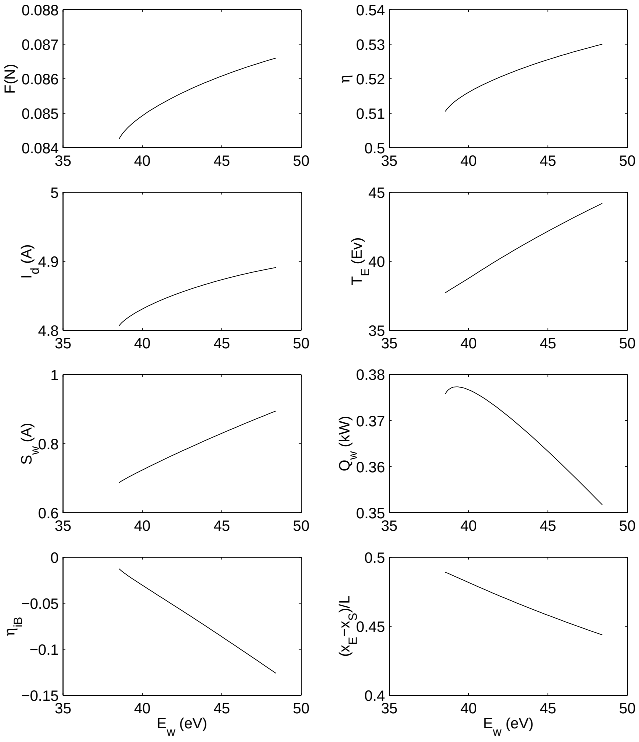

Figure C.13: Influence of the SEE reference temperature of the chamber material; E_w is T_1 in the main text.

BIBLIOGRAPHY

[1] E. Ahedo. Structure of the plasma-wall interaction in an oblique magnetic field. *Physics of Plasmas*, 4:4419–4430, 1997.

[2] E. Ahedo. Presheath/sheath model of a plasma with secondary emission from two parallel walls. *Physics of Plasmas*, 9:(october), 2002.

[3] E. Ahedo. Radial macroscopic model of a plasma flowing along annular dielectric walls. *Physics of Plasmas*, 9(7):3178–3186, 2002.

[4] E. Ahedo, J.M. Gallardo, and M. Martínez-Sánchez. Effects of the dielectric walls on the axial discharge of a Hall thruster. In *38th Joint Propulsion Conference, Indianapolis, IN*, AIAA 2002-4244. American Institute of Aeronautics and Astronautics,Washington, DC, 2002.

[5] E. Ahedo, J.M. Gallardo, and M. Martínez-Sánchez. Model of the plasma discharge in a Hall thruster with heat conduction. *Physics of Plasmas*, 9:4061–4070, 2002.

[6] E. Ahedo, P. Martínez, and M. Martínez-Sánchez. Steady and linearly-unsteady analysis of a Hall thruster with an internal sonic point. In *36th Joint Propulsion Conference, Huntsville, AL*, AIAA 2000-3655. American Institute of Aeronautics and Astronautics,Washington, DC, 2000.

[7] E. Ahedo, P. Martínez-Cerezo, J.M. Gallardo, and M. Martínez-Sánchez. Characterization of the plasma in a Hall thruster. In *27th International Electric Propulsion Conference, Pasadena, CA*, IEPC 01-17. Electric Rocket Propulsion Society, Cleveland, OH, 2001.

[8] E. Ahedo, P. Martínez-Cerezo, J.M. Gallardo, and M. Martínez-Sánchez. Modelling the plasma flow in a Hall thruster. In *SP-476: Proc. 7th Spacecraft Charging Technology Conf.*, pages 539–544, Noordwijk, The Netherlands, 2001. European Space Agency.

[9] E. Ahedo, P. Martínez-Cerezo, and M. Martínez-Sánchez. Model of plasma-wall interaction effects in a Hall thruster. In *37th Joint Propulsion Conference, Salt Lake City, UT*, AIAA 2001-3323. American Institute of Aeronautics and Astronautics,Washington, DC, 2001.

[10] E. Ahedo, P. Martínez-Cerezo, and M. Martínez-Sánchez. One-dimensional model of the plasma flow in a Hall thruster. *Physics of Plasmas*, 8:3058–3068, 2001.

[11] E. Ahedo and M. Martínez-Sánchez. One-dimensional plasma structure in Hall thruster. In *34th Joint Propulsion Conference, Cleveland, OH*, AIAA 98-8788. American Institute of Aeronautics and Astronautics,Washington, DC, 1998.

[12] E. Ahedo and F. I. Parra. Model of radial plasma-wall interactions in a Hall thruster. In *38th Joint Propulsion Conference, Indianapolis, IN*, AIAA 2002-4106. American Institute of Aeronautics and Astronautics,Washington, DC, 2002.

[13] S. Barral, K. Makowski, Z. Peradzynski, N. Gascon, and M. Dudeck. Numerical study of the current-voltage characteristic of Hall thrusters. In *27th International Electric Propulsion Conference, Pasadena, CA*, IEPC 01-27. Electric Rocket Propulsion Society, Cleveland, OH, 2001.

[14] I.I. Beilis and M. Keidar. Sheath and presheath structure in the plasma-wall transition layer in an oblique magnetic field. *Physics of Plasmas*, 5(5):1545–1553, 1998.

[15] A.M. Bishaev and V. Kim. Local plasma properties in a Hall-current accelerator with and extended acceleration zone. *Sov. Physics-Tech. Physics*, 23(9):1055–1057, 1978.

[16] R.C. Bissell, P.C. Johnson, and P.C. Stangeby. A review of models for collisionless one-dimensional plasma flow to a boundary. *Physics of Fluids B*, 1(5):1133–1140, 1989.

[17] J.A. Bittencourt. *Fundamentals of Plasma Physics.* Pergamon, Oxford, 1986.

[18] V. Blateau, M. Martínez-Sánchez, O. Batishchev, and J. Szabo. PIC simulation of high specific impulse Hall effect thruster. In *27th International Electric Propulsion Conference, Pasadena, CA*, IEPC 01-37. Electric Rocket Propulsion Society, Cleveland, OH, 2001.

[19] J.P. Boeuf and L. Garrigues. Low frequency oscillations in a stationary plasma thruster. *J. Applied Physics*, 84(7):3541–3554, 1998.

[20] D. Bohm. *The characteristics of electrical discharges in magnetic fields* , page 77. MacGraw-Hill, New York, 1949.

[21] A.I. Bugrova, A.I. Morozov, and V.K.Kharchevnikov. Experimental investigation of near wall conductivity. *Sov. J. Plasma Physics*, 16(12):849–856, 1990.

[22] J.V. Dugan and R.J. Sovie. Volume ion production costs in tenuous plasmas: A general atom theory and detailed results for helium, argon, and cesium. Technical report, NASA TN D-4150.

[23] G.A. Emmert, R.M. Wieland, A.T. Mense, and J.N. Davidson. Electric sheath and presheath in a collisionless, finite ion temperature plasma. *Physics of Fluids*, 23:803–812, 1980.

[24] V.Y. Fedotov and A.A. Ivanov. On the electron energy distribution function in a Hall-type thruster. *Physics of Plasmas*, 6:4360–4365, 1999.

[25] J. M. Fife. *Hybrid-PIC Modeling and Electrostatic Probe Survey of Hall Thrusters.* PhD thesis, Massachusetts Institute of Technology, 1998.

[26] J.M. Fife, M. Martínez-Sánchez, and J. [illegible]

J [illegible] L [illegible] Lo

[27] N.J. Fisch, Y. Raitses, L.A. Dorf, and A.A. Litvak. Variable operation of Hall thuster with multiple segmented electrodes. *J. Applied Physics*, 89(4):2040–2046, 2001.

[28] A. Fruchtman and N.J. Fisch. Modelling the Hall Thruster. In *34th Joint Propulsion Conference, Cleveland, OH*, AIAA 98-3500. American Institute of Aeronautics and Astronautics,Washington, DC, 1998.

[29] A. Fruchtman, N.J. Fisch, and Y. Raitses. Control of the electric-field in a Hall thruster. *Phys. Plasmas*, 8(3):1048–1056, 2001.

[30] J.M. Gallardo and E. Ahedo. Effects of an intermediate electrode on the Hall thruster plasma discharge. In *38th Joint Propulsion Conference, Indianapolis, IN*, AIAA 2002-4112. American Institute of Aeronautics and Astronautics,Washington, DC, 2002.

[31] G. Guerrini, C. Michaut, M. Dudeck, A.N. Vesselovzorov, and M. Bacal. Characterization of plasma inside the SPT-50 channel by electrostatic probes. In *25th International Electric Propulsion Conference, Cleveland, OH*, IEPC 97-053. Electric Rocket Propulsion Society, Cleveland, Ohio, 1997.

[32] James M. Haas and Alec D. Gallimore. An Investigation of Internal Ion Number Density and Electron Temperature Profiles in a Laboratory-Model Hall Thruster. In *36th Joint Propulsion Conf., Huntsville, Alabama*, number AIAA 2000-3422. American Institute of Aeronautics and Astronautics,Washington, DC, 2000.

[33] E.R. Harrison and W.B. Thompson. The low pressure plane symmetric discharge . *Proc. Physical Society of London*, 74:145–152, 1959.

[34] G.D. Hobbs and J.A. Wesson. Heat flow through a Langmuir sheath in the presence of electron emission . *Plasma Physics*, 9:85–87, 1967.

[35] G.S. Janes and R.S. Lowder. Anomalous electron diffusion and ion acceleration in a low-density plasma . *Physics of Fluids*, 9(6):1115–1123, 1966.

[36] L. Jolivet and J.-F. Roussel. Effects of the secondary electron emission on the sheath phenomenon in a Hall thruster. In *SP-465: 3rd Spacecraft Propulsion Conference, Cannes(Francia)*, pages 367–376, Noordwijk, The Netherlands, 2000. European Space Agency.

[37] M. Keidar, I.D. Boyd, and I.I. Beilis. Plasma flow and plasma-wall transition in Hall thruster channel. *Physics of Plasmas*, 8(12):5315–5322, 2001.

[38] V. Kim. Main physical features and processes determining the performance of stationary plasma thrusters. *J. Propulsion Power*, 14(5):736–743, 1998.

[39] K. Komurasaki, K. Mikami, and Y. Arakawa. Two-dimensional numerical model of plasma flow in a Hall thruster. *J. Propulsion Power*, 11(6):1317–1323, 1995.

[40] I. Langmuir. . *Physical Review*, 33:954–, 1929.

[41] D.H. Manzella, D.T. Jacobson, and R.S. Jankovsky. High voltage SPT performance. In *37th Joint Propulsion Conference, Salt Lake City, UT*, AIAA 2001-3774. American Institute of Aeronautics and Astronautics,Washington, DC, 2001.

[42] N.B. Meezan and M.A. Capelli. Electron density measurements for determining the anomalous electron mobility in a coaxial Hall discharge plasma. In *36th Joint Propulsion Conference, Huntsville, AL*, AIAA 2000-3420. American Institute of Aeronautics and Astronautics,Washington, DC, 2000.

[43] C.A. Ordonez and R.E. Peterkin. Secondary electron emission at anode, cathode, and floating plasma-facing surfaces. *Journal of Applied Physics*, 79(5):2270–2274, 1996.

[44] J.E. Pollard and E.J. Beiting. Ion energy ion velocity, and thrust vector measurements for the SPT-140 Hall thruster. In *SP-465: 3rd Spacecraft Propulsion Conference, Cannes(Francia)*, pages 789–796, Noordwijk, The Netherlands, 2000. European Space Agency.

[45] M. A. Raadu. The physics of double layers and their role in astrophysics. *Physics Reports*, 178:26–97, 1989.

[46] Y. Raitses, J. Ashkenazy, and G. Appelbaum. Experimental investigation of the effect of channel material on Hall thruster characteristics. In *25th International Electric Propulsion Conference, Cleveland, Ohio*, IEPC 97-056. Electric Rocket Propulsion Society, Cleveland, Ohio, 1997.

[47] Y. Raitses, L.A. Dorf, A.A. Litvak, and N.J. Fisch. Plume reduction in segmented electrode Hall thuster . *J. Applied Physics*, 88(3):1263–1270, 2000.

[48] S. H. Lam. Unified theory for the Langmuir probe in a collisionless plasma. *Physics of Fluids*, 8:73–87, 1965.

[49] J.M. Sankovic, J.A. Hamley, and T.W. Hang. Performance evaluation of the russian spt-100 thruster at nasa lerc. In *24th International Electric Propulsion Conference, Moscow, Russia*, IEPC 93-094. Electric Rocket Propulsion Society, Cleveland, Ohio, 1993.

[50] J.T. Scheuer and G.A. Emmert. A fluid treatment of the plasma presheath for collisionless and collisional plasmas. *Physics of Fluids B*, 2:445–451, 1990.

[51] L.A. Schwager. Effects of secondary and thermionic electron emission on the collector and source sheaths of a finite ion temperature plasma using kinetic theory and numerical simulation. *Physics of Fluids B*, 5:631–645, 1993.

[52] K.F. Stephens and C.A. Ordonez. Sheath and presheath potentials for anode, cathode and floating plasma-facing surfaces. *J. Appl. Physics*, 85:2522–2527, 1999.

[53] H. Tahara, D. Goto, T. Yasui, and T. Yoshikawa. Thrust performance and plasma characteristics of low power Hall thrusters. In *27th International Electric Propulsion Conference, Pasadena, CA*, IEPC 01-42. Electric Rocket Propulsion Society, Cleveland, OH, 2001.

[54] L. Tonks and I. Langmuir. A general theory of the plasma of an arc. *Physical Review*, 34:876–922, 1929.

[55] J.R. Vaughan. A new formula for secondary emission yield. *IEEE Transactions on Electron Devices*, 36(9):1963–1967, 1989.